THE UNIVERSITY *of* EDINBURGH
School of Engineering and Electronics &
Centre for Materials Science and Engineering

Synthesis and Characterization of High Temperature Cement-Based Hydroceramic Materials

Konstantinos Kyritsis

A thesis submitted to the University of Edinburgh for the Degree of Doctor of Philosophy

December 2008

DECLARATION

I declare that this thesis has been composed by myself and is all my own work except where otherwise stated.

Konstantinos Kyritsis
October 2008

ACKNOWLEDGMENTS

This thesis would not have been accomplished without the help, guidance and support of many people.

First and foremost, I would like to thank my two supervisors Prof. Christopher Hall and Dr. Nicola Meller for their constant help, expert advice and encouragement over the last three years. During my PhD I had the freedom to follow my own ideas which I am very grateful for.

I am also grateful to Dr. Vasileios Koutsos and Dr. Jane Blackford for their useful advices during my studies and for getting me familiar with the materials teaching studio.

Many thanks go to David Steel and Chris Hayward for their help with the electron microprobe experiments. I also thank Chris Jeffree for his assistance with the operation of the scanning electron microscope.

I am especially thankful to our external collaborators. Dr. Moira Wilson and Dr. Margaret Carter from the University of Manchester, School of Mechanical, Aerospace and Civil Engineering for their help and guidance with the permeability experiments. Many thanks go to Dr. Dale Bentz from the National Institutes of Standards and Technology (NIST), for his useful help and advices on the permeability simulations.

I would like to acknowledge Dr. David Taylor from Daresbury Laboratories for his assistance with synchrotron expriments.

I acknowledge the Engineering and Physical Sciences Research Council (EPSRC) for the financial support of this project. Also I would like to thank Dyckerhoff, especially Dr. Plank Heiko, and Sibelco for donating the starting materials for my experiments.

I am very thankful to all my colleagues at the Centre for Science at Extreme Conditions; Dr. Javier Sanchez-Benitez, Dr. Luis Ortega San Martin, Dr. Alistair Davidson, Dr. Sandra Carlsson, Dr. Iain Osvald, Dr. Jenny Rodgers, Wei Tin Chen, Adrian Hill, George Penny, Gaètan Giriat, and Artur Bocian, for the good times we shared, not only in the office but also in our free time. Many thanks go to my colleagues at the Institute of Materials and Processes; Dr. Andrea Hamilton, John Walker, Dr. Daniel Higgins and Dr. David Curry.

I would also like to thank all my friends that really supported me during my studies in Edinburgh; Dr. Emmanouil Glynos, Giannis Koltsidas, Kostas Krikelas, Gerasimos Skouvaklis, Savvas Makalias, Apostolos Apostolidis, Meletis Mexis, Akis Damoulas, Apostolos Evangelopoulos and Dr. Stratis Viglas and of course the rest of the "Greek gang" in Edinburgh; Anastasia Kostogiannou, Fifi Oikonomopoulou, Georgia Papakleovoulou, Iro Fourtouna, Dr. Kostas Oikonomou, Panagiotis Douvaras, Dr. Tasos Kementsietsidis and Dimitris Tsivoulas. I could not have asked to be part of a better group of people away from home. Our nights out, our feasts and our trips around the UK and Europe are some of my best memories.

Apart from those in Edinburgh, the last group of people I would like to thank is my friends from back home: Manos Katsipatakis, Nikos Konstantopoulos, Dimitris Kloukinas, Georgia Kafatou, George Nousias, Thanasis Spyrou, Kostas and Tassoula Zouridakis. They taught me the true meaning of friendship even though time and distance barriers were keeping us apart.

Finally, and most importantly, I would like to thank my family. My father Charalambos, my mother Maria and my brother Alexandros for their unconditional love and support even though this meant that we have to be apart for such a long time. Last but not least I would like to thank my partner Emmanouella for always being there for me, and for her patience and understanding all this time we were apart.

“To my parents my brother

and to Emmanouella”

SUMMARY

Synthesis and characterization of high temperature cement-based hydroceramic materials

Cement-based materials are of importance in the construction of geothermal wells and high-temperature oil and gas wells. These materials fill the annulus between the well casing and the rock forming a protective layer, known as sealant, which is used primarily to secure and support the casing inside the well. In addition it prevents entry of unwanted fluids into the well and communication between formation fluids at different levels. These cement based sealants need to perform for many years at high temperatures and in severe chemical environments; conditions which can cause the material of the well-casing to degrade resulting in reduced strength and increased permeability.

The aim of this study is to develop new materials which will have the potential properties (high strength and low permeability) for use as sealants in geothermal and deep, hot oil wells. In order to do this special cement slurries, based on the $CaO–Al_2O_3–SiO_2–H_2O$ (CASH) hydroceramic system, have been synthesised over the temperature range 200 to 350 °C (i.e. the typical working temperature of these wells). The additives used in these cement slurries are silica flour and alumina.

A detailed description of a suite of novel hydroceramic compositions over the temperature range 200 to 350 °C is given. X-ray diffraction has been used to determine the mineralogical composition and Rietveld refinement to quantify the known phases present at different temperatures. In addition the chemistry of some of the major phases present has been examined using electron probe microanalysis. Scanning electron microprobe and simulation software have been employed to study the crystal shape of these major minerals.

The engineering properties of the hydroceramic materials are very important. A study of the compressive strength and permeability has been carried out over a range of temperature (200 to 350 °C). In addition permeability has been calculated using simulation software and the results compared with experimental values.

Hydroceramic formulations with excellent strength and permeability measurements have been found. Some of these formulations have been tested for durability under simulated well conditions. These materials have been immersed into different brines for a certain period of time at temperatures between 200 to 300 °C. Some preliminary results regarding the changes in mineralogy in these samples are presented in this thesis. These experiments have been carried out at the Synchrotron Radiation Source (SRS) using tomographic energy-dispersive diffraction imaging (TEDII).

Major part of this thesis has been accepted for publication in international peer review journals. A list of all the publications can be obtained at the end of this thesis (Appendix –V).

Keywords: Cement slurries, hydroceramics, mineralogy, X-ray diffraction methods, electron probe microanalysis, crystal morphology, scanning electron microscopy, engineering properties, simulation methods.

TABLE OF CONTENTS

CHAPTER I

GENERAL INTRODUCTION

I- 1. Introduction

The demand for energy around the world is constantly increasing. Studies have shown that by 2030, worldwide energy demand will be more than 50% greater than it is today [1]. Oil resources are running out therefore oil industries are turning their interest to deeper reserves [2]. On the other hand renewable energy (i.e. energy generated from natural resources and it is environmental friendly) are of particular interest. One type of renewable energy is geothermal power.

Geothermal power is energy generated by heat stored beneath the earth surface. This energy is used globally in applications ranging from electricity generation (using steam to drive turbines) to space heating using ground source heat pumps (GSHP), which extract energy from shallow groundwater atmospheres. Potential sources of geothermal energy exist in many regions. In the UK potential resources in the form of radiothermal granites [3-7] are in Cornwall and Weardale but have not yet been fully exploited. In geothermal systems, cool fluids are pumped down wells, heated at depth by the surrounding rock formation and returned to surface via a production well (Figure I-1). This method, formerly known as hot dry rock (HDR) technology and now as engineered geothermal systems (EGS), requires the annulus between the well casing and the rock formation to be sealed with cement based materials.

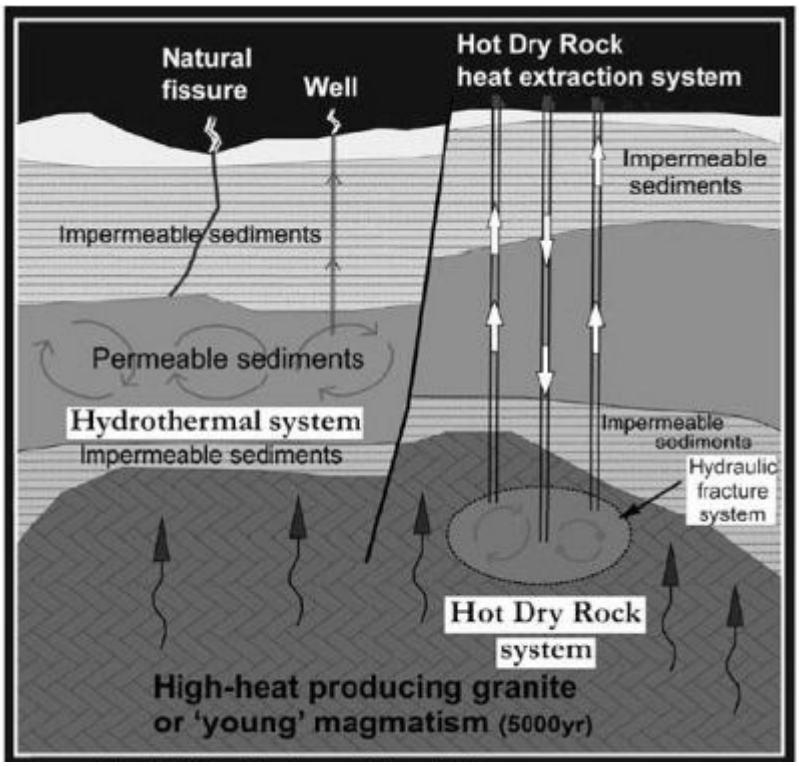

Figure I-1: Image illustrating the Hot Dry Rock process. (source dailyrecording.com.au/images)

Cement is universally used in the construction of oil and geothermal wells. Cement slurries are placed primarily to secure and support the casing inside the well, but also to prevent entry of unwanted fluids into the well and communication between formation fluids at different levels (Figure I-2) [8]. These cements need to perform for many years at high temperatures and in severe chemical environments, such as in brines or ground waters containing carbon dioxide [9]. Such environments can cause the material of the well-casing to degrade resulting in reduced strength and increased permeability [10-13]. It is therefore necessary for cement formulations to be sufficiently durable and resistant to chemical attack in order to seal the well for its working life.

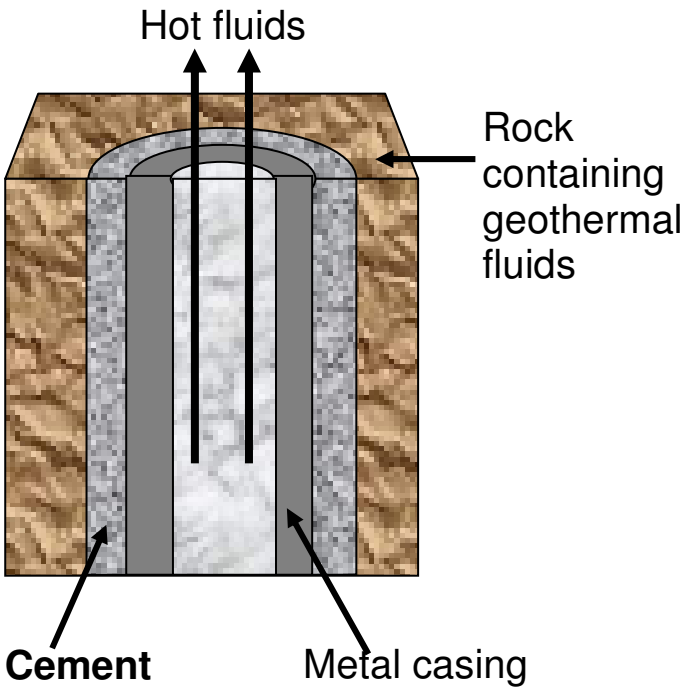

Figure I-2: Cross-section of a geothermal well showing the position of cement. Cement is pumped between the metal casing and the rock to allow recovery of hot fluids and prevent contamination by underground fluids.

Typical working temperatures for these wells are between 200 and 350 °C [8] and when the temperature exceeds 110 °C special cement formulations are used. There have been several recent attempts to design cements which are more durable at higher temperatures. Barlet- Gouédard et al. [14,15] and Meller and Hall [16,17] have designed slurries based on the $CaO–Al_2O_3–SiO_2–H_2O$ (CASH) system.

The aim is to develop formulations suitable for geothermal and deep, hot oil wells. These formulations contain minerals which occur in nature and may have the properties needed to be good well sealants. These are impermeability, strength and long-term stability in well environments. In particular, silica and alumina can be added to cement to produce CASH hydroceramics with a wide range of phases. A hydroceramic is defined here as any ceramic material containing chemically combined water as H_2O or OH or both [17].

I- 2. Research strategy

In this thesis the work is organised as follows:

In **Chapter II** a detailed examination of the mineralogy of sealants for geothermal or deep oil wells with additions of silica and alumina will be carried out, over the temperature range 200 to 350 °C.

In the next 3 chapters the chemistry and the crystal morphology of some of the major minerals that grow in hydroceramics will be described. In **Chapter III** and **IV** minerals with high and low Ca/Si ratio will be described respectively. In **Chapter V** aluminum bearing phases present in the hydrocerams will be examined.

The engineering properties of the hydroceramic materials such as compressive strength and permeability are very important. Therefore in **Chapter VI** the properties of these materials are described in detail. In addition simulation software has been employed to calculate permeability and compare it with experimental results.

Finally in **Chapter VII** the behaviour of these materials under simulated well conditions will be examined. In this Chapter preliminary results will be given of the behaviour of the mineralogy of hydroceramics when immersed in different brines.

I- 3. References

1. http://www.wikinvest.com/concept/Rising_Worldwide_Demand_for_Energy,

2. http://www.infield.com/deepwater_ultra_deepwater_market_reports.htm,

3. D. A. C. Manning, P. L. Younger, F. W. Smith, F. W. Jones, J. M. Jones, D. J. Dufton, and S. Diskin, "A deep geothermal exploration well at Eastgate, Weardale, UK: a novel exploration concept for low-enthalpy resources," *Journal of the Geological Society, London,* **164** 371-382 (2007).

4. K. E. Rollin, "A simple heat-flow quality function and appraisal of heat-flow measurements and heat-flow estimates from the UK Geothermal Catalogue," *Tectonophysics,* **244** 185-196 (1995).

5. P. MacDonald, A. Stedman, and G. Symons, "The UK geothermal hot dry rock R&D programme"; pp.5-11 in *Proceedings of the Seventeenth Workshop on Geothermal Reservoir Engineering, Stanford, CA*. Edited by H. J. Ramey, R. N. Horne, W. E. Brigham, andJ. W. Cook. Stanford University, Stanford, CA, 1992.

6. G. C. Brown, J. Plant, and L. M. K., "Geochemical and geophysical evidence on the geothermal potential of Caledonian Granites in the UK," *Nature,* **280** 129-131 (1979).

7. J. D. Garnish, "Geothermal energy and the UK," *Physics Education,* **13** 372-379 (1978).

8. E. B. Nelson, "Thermal Cements", pp. 9/1-9/19 in *Well Cementing***.** Edited by E. B. Nelson. Schlumberger Educational Services, Sugar Land, Texas, 1990.

9. A. J. Philippacopoulos and M. L. Berndt, "Structural analysis of geothermal well cements," *Geothermics,* **31** [6] 657-676 (2002).

10. R. A. Kennerly, "Products of hydrothermal hydration of cements from geothermal bores," *New Zealand Journal of Science,* **4** 453-468 (1961).

11. H. F. W. Taylor,"*Cement Chemistry*" 2nd. London, Thomas Telford Publishing, 1997.

12. R. Oberste-Padtberg, "Degradation of cements by magnesium brines"; in *Proceedings of the 7th International Conference on Cement Microscopy*. Edited by J. Bayles, G. R. Gouda, and A. Nisperos. Duncansville, TX, 1985.

13. T. Sugama, L. E. Brothers, and T. R. Van de Putte, "Air-foamed calcium aluminate phosphate cement for geothermal wells," *Cement and Concrete Composites,* **27** [7-8] 758-768 (2005).

14. V. Barlet-Gouédard, S. Danican, E. Nelson, and C. Cambus, "Cement compositions for high temperature applications." In *PCT Patent Application***.** 2003.

15. V. Barlet-Gouédard and B. Goffé, "High temperature cements," pp. 11. In *PCT Patent Application***.** 2005.

16. N. Meller and C. Hall, "Hydroceramic sealants for geothermal wells"; pp.281-284 in *Proceedings of the International Congress on Applied Mineralogy*. Edited by M. Pecchio, F. R. D. Andrade, L. Z. D. D'Agostino, H. Kahn, L. M. Sant'Agostigno, andM. M. M. L. Tassinari. Brazil, 2004.

17. N. Meller, C. Hall, and J. Phipps, "A new phase diagram for the CaO-Al_2O_3-SiO_2-H_2O hydroceramic system at 200 ˚C," *Materials Research Bulletin,* **40** 715-723 (2005).

CHAPTER II

MINERALOGY OF HYDROCERAMICS

II- 1. Introduction

In oilfield engineering, it is standard practice to use special cement formulations when the well temperature exceeds 110 °C. Above this temperature the predominant phase formed in the hydration of an oilwell cement, α-dicalcium silicate hydrate [$Ca_2SiO_3(OH)_2$], forms bulk materials which are too weak and permeable to seal the well [1,2]. Upon initial hydration cement first forms a C-S-H gel which on heating converts to crystalline $Ca_2SiO_3(OH)_2$. This crystallization causes a reduction in solid volume and is accompanied by an increase in permeability and the reduction in compressive strength known as *strength retrogression*. Therefore silica is commonly added to cement. This prevents the formation of $Ca_2SiO_3(OH)_2$ and instead a sequence of other calcium silicate hydrates form over a range of temperatures [3].

In Figure II-1 is presented the well known summary diagram of Taylor (redrawn) [3], based on information available in 1964, with the different calcium silicate hydrated products formed in different proportions of CaO/SiO_2 ratio. The grey shaded area illustrates the temperature range covered by this study (200 to 350 °C). Hillebrandite forms when small amounts of silica flour are added at lower temperatures (150 °C to 200 °C) and calcium chondrdite (reinhardbraunsite) at higher temperatures (250 °C). At temperatures above 110 °C and when more silica is added, 11Å tobermorite [$Ca_5Si_6O_{17}•5H_2O$] forms and converts at about 150 °C to xonotlite [$Ca_6Si_6O_{17}(OH)$] or gyrolite [$Ca_{16}Si_{24}O_{60}(OH)_8•(14+n)H_2O$ $0 \leq n \leq 3$] depending on the percentage of silica added. Around 250 °C truscotite [$Ca_{14}Si_{24}O_{62}•(4+z)H_2O$, $0 \leq z \leq 6$] forms which co-exists with xonotlite up to 400 °C. These hydrates produce bulk materials with greater strength and lower permeability. This chapter seeks to provide a detailed examination of the mineralogy of such sealants with additions of silica and alumina for geothermal wells over the temperature range 200 to 350 °C. Engineering properties are described elsewhere.

With high temperature well cementing in mind, Barlet-Gouédard *et al*. [4,5] and Meller *et al*. [6-8] have recently designed hydroceramics based on the $CaO–Al_2O_3–SiO_2–H_2O$ (CASH) system at 200 and 300 °C. A hydroceramic is defined here as any ceramic composition containing chemically combined water as H_2O or OH or both. The studies carried out by Barlet-Gouédard *et al*. used the principle, first described by Roy *et al.* [9-11], that the sealant should have the same overall chemical composition as the surrounding rock formation, hence if the rock

formation is stable in that environment the sealant should be too. For this reason a limited number of compositions were assessed. The research here extends the CASH system to cover a wider range of compositions and temperatures. A detailed knowledge of the mineralogy of a complete system delivers more options should some compositions be unsuitable in certain chemical environments. A detailed description of the mineralogy of a suite of hydroceramic compositions is given in this chapter over the temperature range 200 to 350 °C. The mineralogical composition was determined using X-ray diffraction and Rietveld refinement to quantify the known phases present at different temperatures. This information is drawn together into a model of the CASH system at temperatures typical of geothermal wells. Ground-breaking work on compositions within the hydrothermal CASH system and their properties was carried out by Roy *et al.* [11], using both cements and lime as the source of calcium oxide. The effects of alkalis and the magnesium oxide additions were also investigated [10].

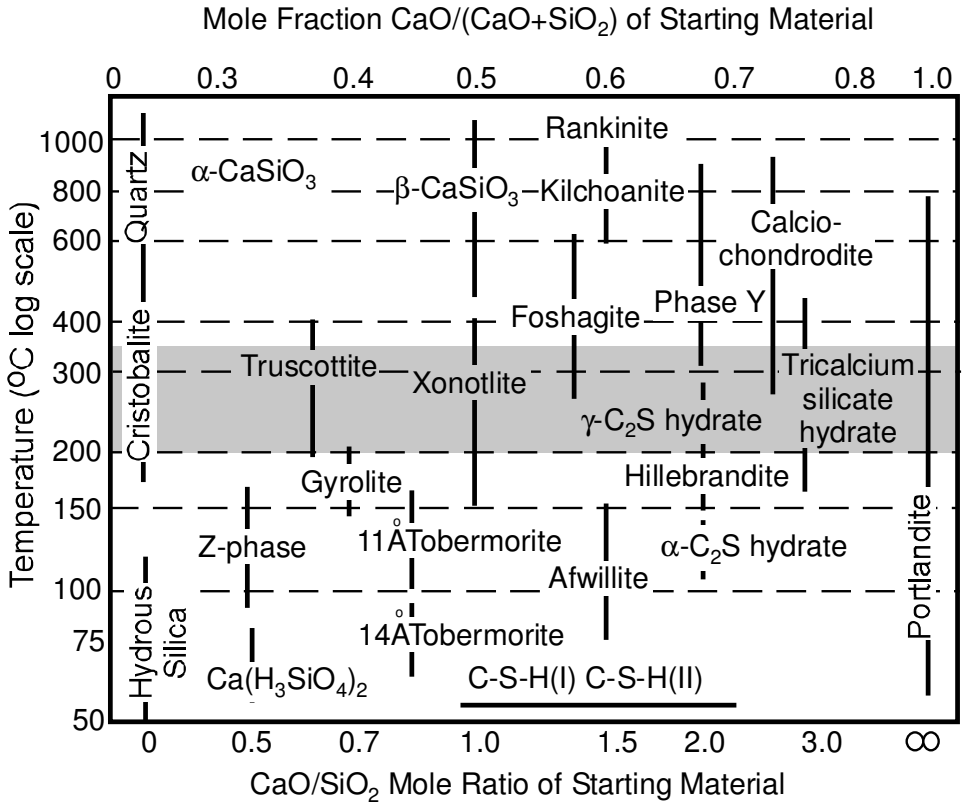

II- 2. Experimental procedures

II- 2.1 Hydroceramic synthesis

Dyckerhoff oilwell cement (API Class G) was used as the basis of the hydroceramics investigated. This commercial cement is widely used in well construction and has a consistent composition. The oxide analysis of the cement and the calculated mineralogical composition are summarized in Table II-1.

Table II-1: Chemical and mineralogical composition of Dyckerhoff Class G cement determined by X-ray fluorescence, LECO sulphur analysis and X-ray diffraction. Wt % phase compositions are calculated from oxide analysis according to the modified Bogue method for oilwell cements [12] and estimated by semi-quantitative Rietveld refinement.

Oxides	**Weight %**	
Na_2O	0.17	
MgO	0.76	
Al_2O_3	3.62	
SiO_2	22.55	
K_2O	0.66	
CaO	65.61	
TiO_2	0.17	
Mn_3O_4	0.14	
Fe_2O_3	4.53	
SO_3	1.82	
Loss on ignition at 1000 °C	1.18	
Free Lime	0.40	
Insoluble residue	Not determined	
% Phases	**By Modified Bogue method**	**By Rietveld Refinement**
Alite	62	60
Belite	21	22
Aluminoferrite	13	16
Gypsum	3	3

The mineralogy from a modified Bogue calculation[¥] [12] developed for oil well cements is in rather good agreement with that estimated by Rietveld whole-pattern fitting (mean of ten independent measurements) using Bruker TOPAS software. Silica was added in the form of silica flour HPF6, supplied by Sibelco and composed of 98 % silica as quartz SiO_2 with trace impurities and a mean grain size of 53 μm. It is a low cost additive widely used in the cementing of higher temperature wells [1]. Reagent grade α-alumina (corundum Al_2O_3) with a grain size of 50 to 150 μm, supplied by Sigma Aldrich [product code 34271-8], was used as the primary source of Al_2O_3. Additional samples were synthesised using finer alumina in the form of polishing powder supplied by Buehler [product code 40-6305-008, grain size 0.3 μm].

A total of 10 g of the starting compounds in the appropriate proportions was mixed with 4 g of water (water to total solids weight ratio w/s=0.4). Table 2 gives all the different compositions investigated using coarse and finer alumina. The results and discussion in this chapter concern samples prepared with coarse alumina unless explicitly stated otherwise. Each sample was mixed by hand for approximately 3 min and loaded into polytetrafluoroethylene (PTFE) cups with 2 cm dia and 1 cm depth. For the samples cured at 350 °C stainless steel cups were used as PTFE was close to its melting point. The samples were placed in a stainless steel autoclave cell (type 4750 Parr Instruments) of 125 mL capacity. The water vapour pressure in the vessel was 1.5 MPa, 4.0 MPa, 8.6 MPa and 16.5 MPa at 200, 250, 300 and 350 °C respectively (Appendix I regarding mass of saturated vapour). The maximum pressure rating of the autoclave cell was 20 MPa. Small notches were cut in the rims of the PTFE cups to ensure a uniform water-saturated atmosphere (Figure II-2) Once the cells are closed they are placed in the oven at 200 °C and left to equilibrate for 5 days. The same procedure was followed for the samples cured at 250 °C, 300 °C and 350 °C. After 5 days the cells were removed from the oven and quenched in cold water for 10 min to prevent further reaction. The samples were dried under vacuum to reduce carbonation before being milled to fine powders for XRD analysis.

[¥] The modified Bogue method is a computational program which calculates the phase composition of cement clinker. More information along with some results can be obtained in Appendix II.

Table II-2: Proportions of starting materials in samples cured at 200, 250, 300 and 350 ˚C. The (#) symbol represents samples made using finer alumina as well.

Proportions (wt %)			
Sample No.	**Dyckerhoff Cement**	**Silica Flour HPF6**	**α-Alumina**
1	100	0	0
2	95	5	0
3	90	10	0
4	85	15	0
5	80	20	0
6	75	25	0
7	70	30	0
8	65	35	0
9	60	40	0
10	55	45	0
11	50	50	0
12	95	0	5
13#	90	0	10
14	85	0	15
15	80	0	20
16	75	0	25
17	70	0	30
18	65	0	35
19#	60	0	40
20	55	0	45
21	50	0	50
22#	80	10	10
23#	70	10	20
24#	70	20	10
25#	60	10	30
26#	60	20	20
27#	60	30	10
28#	50	10	40
29#	50	20	30
30#	50	30	20
31#	50	40	10

Figure II-2: Image shows autoclave Parr cell. The small dark grey stainless steel cup is used to load the samples for XRD analysis. The tall stainless steel cups are used to produce samples for compressive strength measurements (see Chapter VI).

II- 2.2 Characterization techniques

II- 2.2.1 X-ray Diffraction (XRD)

X-ray diffraction is used to determine the structure of molecule, mostly crystals with atoms which are organised in repeating planes. These planes can act as reflecting surfaces for X-rays as a result of the interaction of the X-ray radiation with the electrons in the atoms. When the distances between the atoms are of the same magnitude as the wavelength of the X-rays, constructive and destructive interferences occur. This result in the diffraction of X-rays emitted at characteristic angles based on the planes between the atoms organised in crystalline structures. The diffraction pattern is characteristic of a crystal and provides information on the positions of each atom in the unit cell, and therefore in the molecule [13,14]. The relationship between wavelength λ, atomic spacing (d) and angle (θ) is defined by the Bragg equation:

$$n\lambda = 2d\sin\theta \qquad \text{(II-1)}$$

The identification of a compound is made by comparison with sets of d-spacing of the diffraction pattern obtained from standard compounds.

A Bruker-AXS D8-series 2 X-ray powder diffractometer, running at 40kV and 40mA, was employed for mineralogical analysis. Incident Cu $K_{\alpha 1}$ radiation was used with a Ge monochromator and passed through a 2 mm monochromator exit slit and 0.2^{o} divergence slit. A Braun position sensitive detector was used to collect data. Three types of scan were employed. Most diffraction patterns were collected over an angular range of 5 to 70^{o} 2θ for approx 30 min total time using a step size of 0.014^{o} 2θ and a count time of 0.3 s per step. Where a more detailed scan was required, samples were run for 6 or 12 h over the same angular range using a smaller step size (0.007^{o} 2θ) and longer count time (1.7 or 3.5 s per step, respectively). Finally, where samples with significant silica additions were made (> 40 wt %), were run at lower angles to confirm the presence or absence of gyrolite whose strongest peak lies at 4^{o} 2θ (22.00 Å).

II- 2.2.2 Rietveld refinement

The XRD pattern of each crystalline material is unique. The principle of Rietveld analysis is to compare the experimental pattern with a pattern simulated based on the presumed amounts, crystal parameters, and equipment parameters of a mixture of a known phase. All these parameters may be adjusted to minimise the difference between the experimental and simulated patterns by least square fitting.

Rietveld analysis always gives the sum of the phases present normalised to 100 %. Therefore all the phases and their known crystal structures present must be entered. If amorphous or unknown phases are present, the amounts of the crystalline phases estimated by the analysis will be higher than the true amounts present. This may be overcome by adding a known amount of a reference standard phase. The analysis may then be corrected by dividing the values by the ratio of the measured to true amount of standard. The difference between the total of the corrected phase quantities and 100 % gives the amount of amorphous (or unknown) phases.

Phases were identified using the powder diffraction database from the International Centre for Diffraction Data (ICDD) and the Bruker search-match software EVA. Once phases are identified they can be quantified using Rietveld refinement methods for which we used the Bruker fitting programme TOPAS. Phase quantification methods have been used successfully both on dry cement [15]

and hydroceramics [6]. The method does however have its limitations. Every phase in the sample must be identified and the crystal structure for each phase must be known. In Table II-3 are presented the phases used for the Rietveld refinement. It is assumed that the samples are wholly crystalline as no amorphous phases were detected either by spiking methods or le Bail silica curve fitting [16]. Where the crystal structure is not known (for example, for $Ca_8Si_5O_{18}$) the proportion of that phase must be estimated using spiking methods like those reported previously. Ten wt percent gypsum is added to our samples and the totals recalculated to estimate the final percentage of $Ca_8Si_5O_{18}$ and its co-existing phases. While a few percent error may normally be expected in association with any of the phases present in the hydroceramics, spiking methods obviously increase such errors and as such quantification by spiking methods should be treated with more caution than normal.

Table II-3: Phases identified in the CASH hydroceramics synthesised at 200 to 350 °C, ICDD card numbers and structure references.

Phase	**ICDD Card No**	**Crystal Structure Reference**
Alpha dicalcium silicate hydrate; a	29-373	Yano *et al.* [17]
Bicchulite; b	86-751	Dann *et al.* [18]
Calcium alumina hydrate; d	14-464	Ponomarev *et al.* [19]
Calcium silicate; m	29-368	None exists
Corundum; c	42-1468	Not referenced
Foshagite; f	74-360	Gard and Taylor [20]
Gyrolite; g	42-1452	Merlino [21]
Hillebrandite; l	42-538	Dai and Post [22]
Hydrogarnet; h	Hibschite 45-1447	Cohen-Addad *et al.* [23]
	Katoite 38-368	Sacerdoti and Passaglia [24]
Jaffeite; j	29-375	Yamnova *et al.* [25]
Kilchoanite; k	11-316	Taylor [26]
Portlandite; p	4-733	Petch [27]
Quartz; q	33-1161	Not referenced
Reinhardbraunsite; r	29-380	Kuznetsova *et al.* [28]
11Å tobermorite; t	19-1364	Merlino *et al.* [29]
Truscottite; v	29-382	Merlino [30] (Truscottite structure based on modified reyerite structure)
Xonotlite; x	29-379	Mamedon and Belov [31]

II- 3. Results and discussion

II- 3.1 X-ray diffraction

The results from the X-ray diffraction along with the estimated Rietveld refinement for samples made using fine alumina and cured at 200 and 250 ℃ are presented in 4. Table II-5 lists all the different compositions using coarse alumina in temperatures between 200 to 350 ℃. The results and discussion in this chapter concern samples prepared with coarse alumina (Table II-5) unless explicitly stated otherwise. These two tables show that the mineralogy of the CASH hydroceramic system is very complicated. All the chemical formulae of the phases present are shown in Appendix III.

Table II-4: Weight percent of phases present in each sample as estimated by Rietveld refinement. Fine alumina used for the preparation of these samples. Codes for phases are given in Table II-3.

Sample No.	200 ℃	250 ℃
13		p=5; j=11; h_1=57; h_2=24
19	h=69; c=31	–
22	–	j=9; h=90
23	–	t=9; h_1=28; h_2=54; c=9
24	t=46; h=54; c=10	t=17; x=27; h=56
25	t=18; h_1=29; h_2=32; c=21	t=9; h_1=36; h_2=34; c=21
26	t=49; q=3;h=36; c=12	–
27	t=91; x=4; c=5	t=62; x=29; c=9
28	t=20; q=2; h=42; c=36	t=12; h_1=41; h_2=14; c=33
29	t=42; q=5; h=26; c=27	t=42; q=2; h=28; c=28
30	t=58; q=9; h=17; c=16	t=70; q=10; c=20
31	t=71; q=14; h=6; c=9	t=68; q=20; c=10

Table II-5: Weight percent of phases present in each sample as estimated by Rietveld refinement. Coarse alumina used for the preparation of these samples. Codes for phases are given in Table II-3.

Sample No.	200 °C	250 °C	300 °C	350 °C
1	p=8; j=74; a=18	p=5; j=76; r=19	p=14; j=36; r=34; h=16	p=18; j=20; r=47; h=15
2	p=8, j=32; a=60	j=32; r=68	j=16; r=68; h=15	p=1; j=8; r=77; h=14
3	j=9; a=6; m=49; k=27; t=9	j=2; r=6; m=84; x=8	j=2; r=11; m=74; x=12	j=10; r=68; f=8; h=14
4	j=4; a=7; m=66; t=11; x=31	j=2; m=85; x=13	j=4; r=15; m=51; x=30	j=11; r=27; x=62
5	t=15; x=85	m=82; x=18	m=73; x=27	x=100
6	t=8; x=85	x=100	m=60; x=40	x=100
7	t=8; x=92	x=100	x=98; v=2	x=60; v=40
8	t=18; x=92	x=59; g=13; v=29	x=71; v=29	x=26; v=74
9	x=36; g=56; q=6	x=18; g=56; v=26	x=35; v=65	x=10; v=90
10	x=22; g=65; q=13	x=5; g=64; v=26; q=5	v=98; q=2	v=91; q=9
11	g=70; q=30	g=64; v=21; q=21	v=88; q=12	v=84; q=16
12	p=7; j=44; a=9; h=40	p=3; j=42; r=7; h=47	p=10; j=30; h=61	p=15; j=16; h=69
13	p=6; j=30; h=64	p=5; j=8; r=7; h=87	p=7; j=17; h=76	p=12; j=6; h=82
14	p=5; j=13; h=82	p=5; j=8; h=87	p=5; j=7; h=88	p=5; j=4; h=81; d=11
15	j=3; h=97	j=7; h=92	j=6; h=83; d=11	p=1; j=3; h=72; b=4; d=20
16	j=3; h=88; c=9	j=7; h=82; c=11	j=5; h_1=71; h_2=3; c=5; d=16	j=1; h=60; c=1; b=16; d=23
17	j=3; h=80; c=16	j=8; h=75; c=16	j=5; h_1=63; h_2=4; c=11; d=16	h=56; c=13; b=11; d=20
18	j=3; h=74; c=24	j=7; h=70; c=23	j=4; h=62; c=18; d=16	h=51; c=19; b=10; d=20
19	j=3; h=67; c=30	j=6; h=62; c=32	j=4; h=47; c=31; d=18	h=43; c=29; b=10; d=18
20	j=2; h=60; c=38	j=5; h=55; c=40	j=3; h=49; c=36; d=12	h=40; c=35; b=8; d=16
21	j=2; h=55; c=43	j=5; h=51; c=44	j=3; h=44; c=42; d=11	h=35; c=42; b=8; d=15
22	j=7; k=26; t=12; h=49; c=6	j=11; h=89	j=7; h=93	p=1; j=4; f=1; x=18; h=75
23	j=4; k=11; t=9; h=61; c=14	h=88; c=12	j=2; h_1=62; h_2=31; c=5	p=3; x=9; h_1=46; h_2=33; c=9
24	t=22; x=39; h=30; c=10	t=10; x=38; h=48; c=4	x=37; h=63	x=9; h_1=44; h_2=35; c=7; b=6
25	j=1; t=8; h=68; c=23	t=6; h=67 (1.4); c=27	h_1=47; h_2=35; c=19	x=4; h_1=37; h_2=36; c=20; b=4
26	t=18; x=36; h=26; c=20	t=7; x=40; h=34; c=19	x=45; h_1=12; h_2=21; c=21	x=56; h=14; c=30
27	t=19; x=64; h=5; c=12	x=84; c=16	x=55; v=31; c=13	x=21; v=58; h=6; c=14
28	t=9; h=54; c=36	t=4; x=10; h=48; c=38	x=3; h_1=35; h_2=28; c=33	h=65; c=32; b=2
29	t=20; x=39; h=11; c=31	t=8; x=55; c=38	x=51; h=13; c=36	x=43; v=15; c=43
30	t=13; x=25; g=38; c=22	x=27; g=37; v=13; c=24	x=35; v=39; c=26	x=11; v=62; c=27
31	g=83; q=8; c=9	g=64; v=20; q=4; c=12	x=13; v=71; q=2; c=15	x=4; v=76; q=6; c=14

II- 3.2 Rietveld refinement

With the presence of unknown errors associated with quantification by Rietveld refinement we might ask how we can even know whether the results are realistic. Mass balancing of simple phase assemblages by Meller *et al.* [6] suggest that the Rietveld refinement method yields realistic results. In addition we have compared the mole ratios $CaO/(CaO+SiO_2)$ and $CaO/(CaO+Al_2O_3)$ of the sample with the corresponding quantities from the Rietveld refinement (Figure II-3) and generally find good agreement. The $CaO/(CaO+SiO_2)$ ratios are particularly close, differing by < 10 % for the most part. $CaO/(CaO+Al_2O_3)$ ratios lie a little further from the 1:1 correlation line, particularly when higher proportions of corundum are added to the mix (>33 wt %). Electron probe results which will be described in detail in Chapter 5 show that the calcium/aluminum ratio of the hydrogarnet is not ideal (the $CaO/(CaO+Al_2O_3)$ value is commonly ≥ 0.70). This has been taken into account in creating the plot but does not fully account for the shortfall in alumina, suggesting that either corundum or hydrogarnet or both are being slightly overestimated by the Rietveld method.

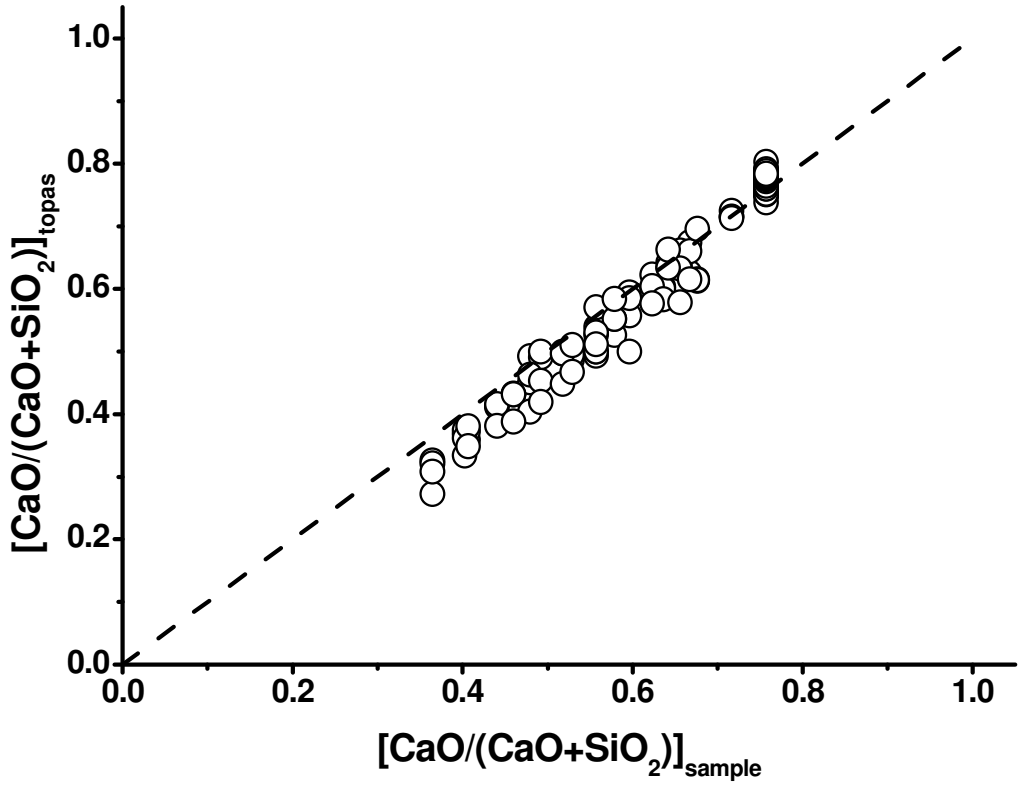

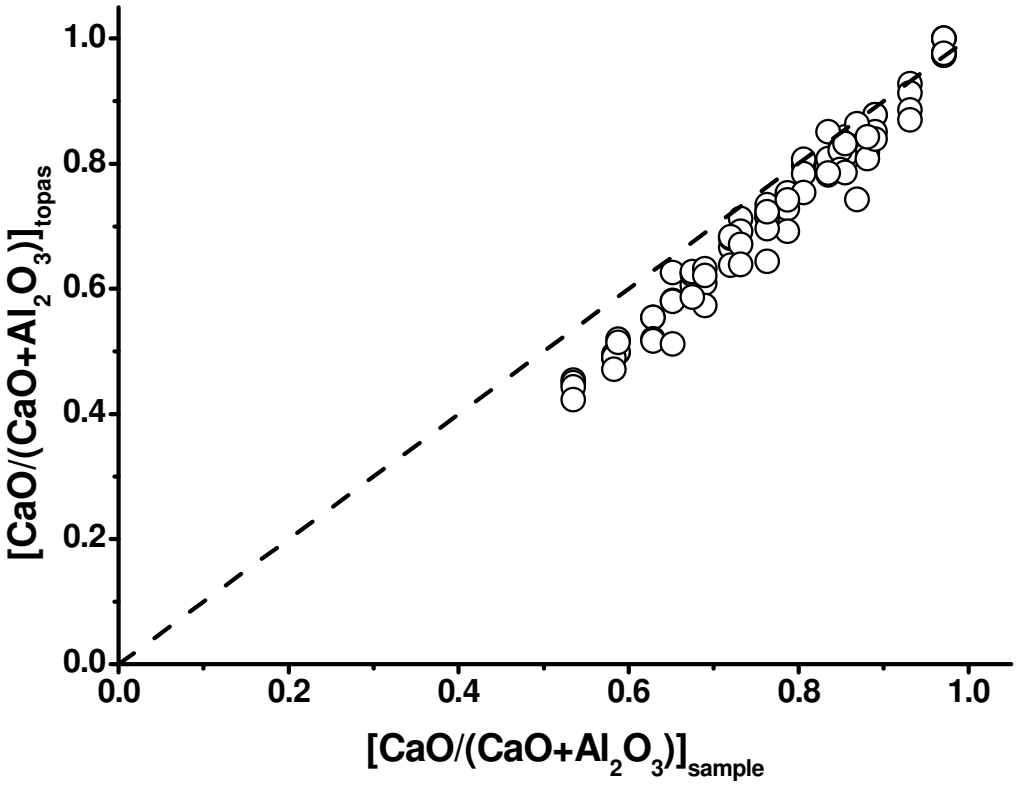

Figure II-3: Comparisons of molar proportions of $CaO/(CaO+SiO_2)$ and $CaO/(CaO+Al_2O_3)$ of the bulk sample and the phase assemblages quantified by Rietveld refinement, Topas (Table II-5).

II- 3.3 The CASH hydroceramic system

II- 3.3.1 High $CaO/(CaO+SiO_2)$ hydrates: portlandite, jaffeite, reinhardnraunsite, hillebrandite and alpha-dicalcium silicate hydrate.

The high $CaO/(CaO+SiO_2)$ (> 0.5) hydrates occur with low silica and/or with low alumina additions (< 20 wt %). Jaffeite persists when more alumina is added but is generally present only in small amounts (typically a few percent). Of these hydrates, the formation of reinhardbraunsite (also known as calcio-chondrodite), hillebrandite and alpha-dicalcium silicate hydrate [α-$Ca_2SiO_3(OH)_2$] are strongly temperature dependent, while portlandite and jaffeite being present over the complete temperature range (Figure II-4 and Figure II-5). Hillebrandite and α-C_2SH are found at 200 °C but not at higher temperatures. Taylor's diagram (Figure II-1)

suggests that α-$Ca_2SiO_3(OH)_2$ is found only up to 150 °C, above which it is replaced by hillebrandite. Hillebrandite is observed as a minor phase in our system (< 10 %) whereas α-$Ca_2SiO_3(OH)_2$ is a major phase (60 %), particularly at 5 wt % silica addition (Table II-5). Hillebrandite and α-$Ca_2SiO_3(OH)_2$ appear to be replaced by reinhardbraunsite above 200 °C.

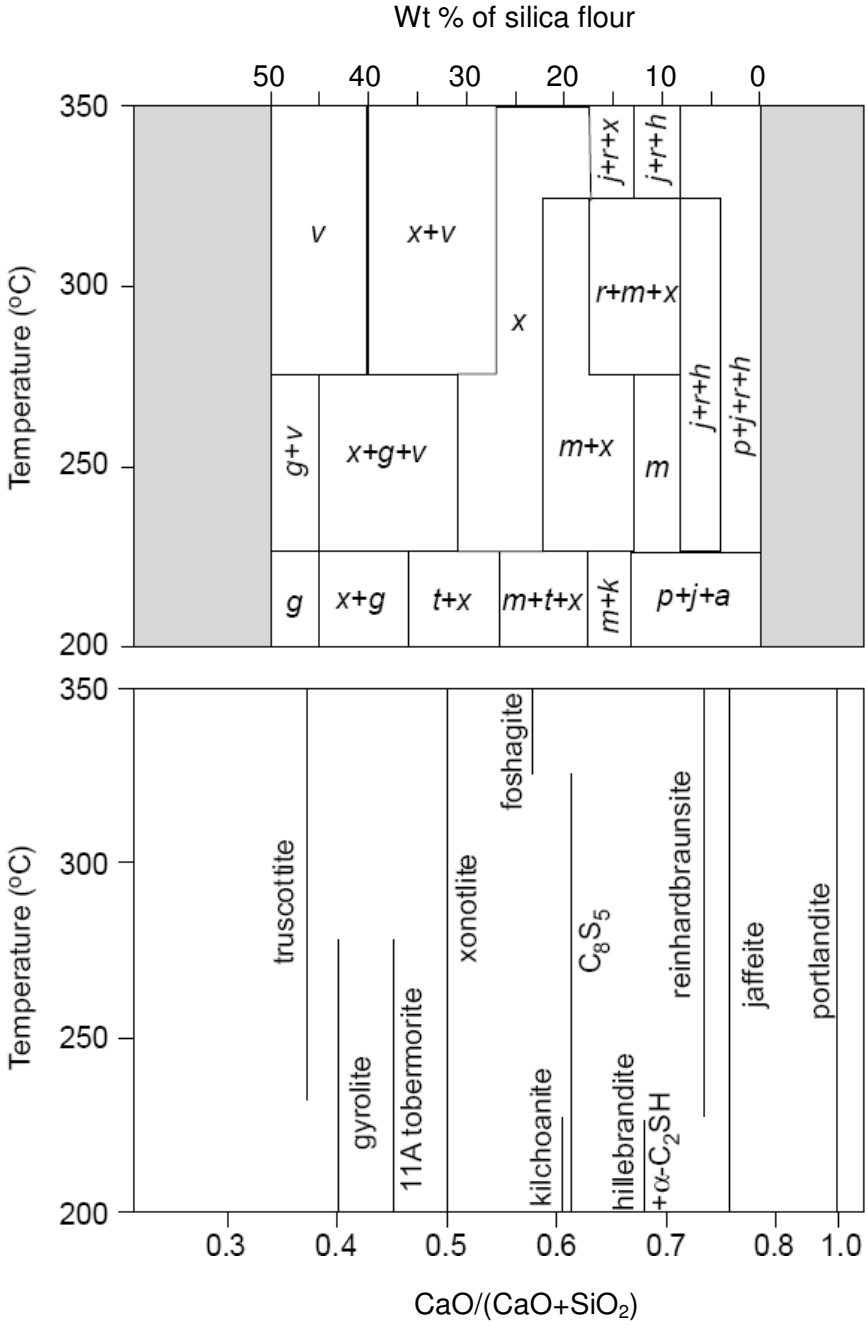

Figure II-4: Phase diagram (lower figure) and phase map (upper figure) for the cement and silica flour system from 200 to 350 °C. The phase diagram shows the temperature over which phases >10 wt % are present. The phase map illustrates which major phases form for different proportions of silica flour in wt %. Abbreviations for phases are given in Table II-3. Shaded area represents compositions not investigated here. C_8S_5 and α-C_2SH corresponds to $Ca_8Si_5O_{18}$ and α-$Ca_2SiO_3(OH)_2$ respectively.

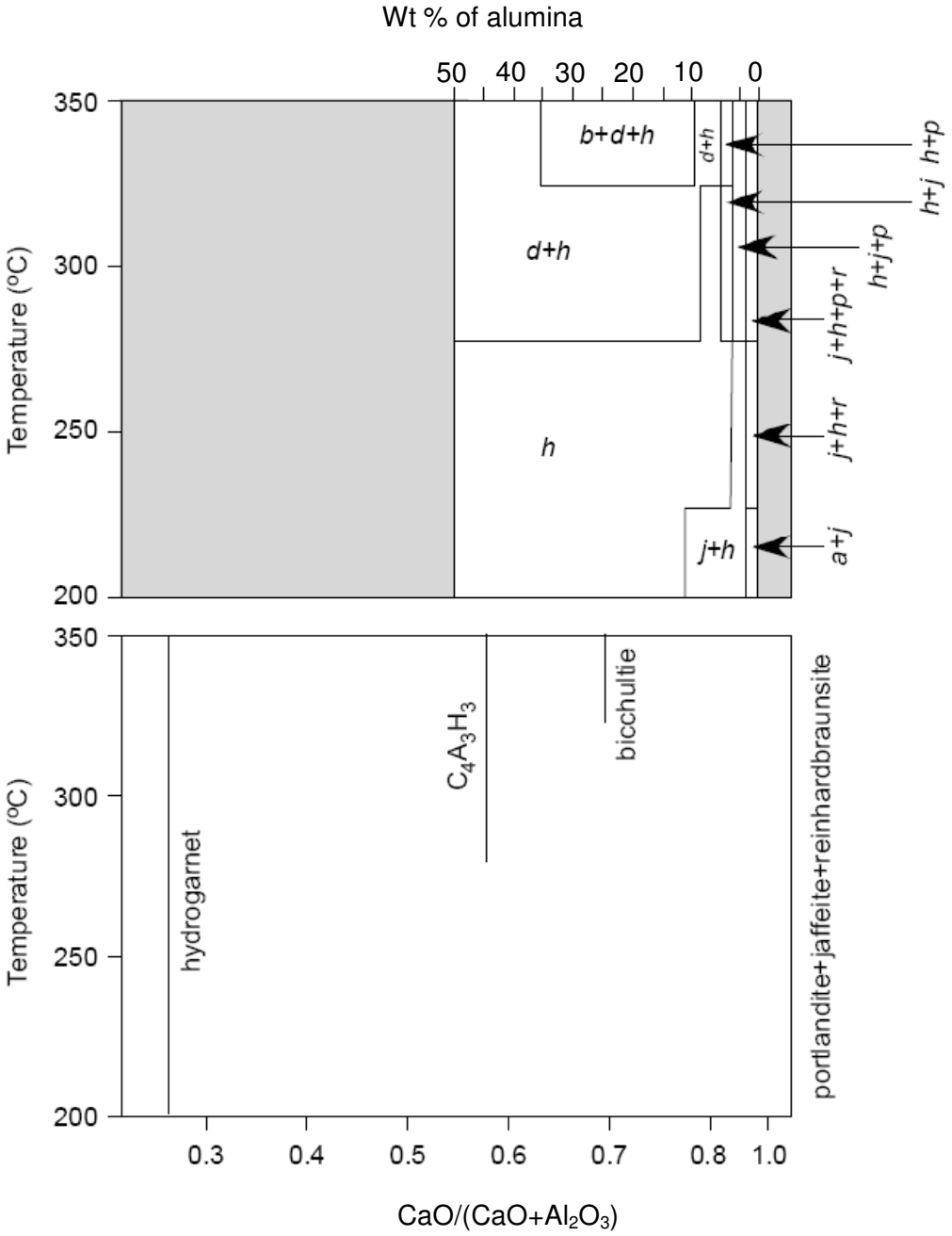

Figure II-5: Phase diagram (lower figure) and phase map (upper figure) for the cement and corundum system from 200 to 350 °C. The phase diagram shows the temperature over which phases >10 wt % are present. The phase map illustrates which major phases form for different proportions of corundum in wt %. Abbreviations for phases are given in Table II-3. Shaded area represents compositions not investigated here. $C_4A_3H_3$ corresponds to calcium aluminum oxide hydrate $Ca_4Al_6O_{13}•3H_2O$.

II- 3.3.2 $Ca_8Si_5O_{18}$

The CASH system at 200 °C has previously been fully described by Meller *et al.* [7,8]. The main difference to note here is that $Ca_8Si_5O_{18}$ was not previously identified in these samples and occurs when 10 to 25 wt % of silica flour is added from 200 to 350 °C. $Ca_8Si_5O_{18}$ is poorly documented in the literature and no crystal structure refinement currently exists. A powder diffraction file does however exist in the JCPDS database (card no. 29-368) and its structure is believed to be related to kilchoanite and γ-$Ca_2SiO_3(OH)_2$. Where it has been observed previously it is found coexisting with [32] or as a decomposition product of γ-$Ca_2SiO_3(OH)_2$ [33] and its XRD pattern typically shows it to be poorly crystalline compared to other calcium silicate (hydrate) products in hydroceramics (Figure II-6), thus accounting for its previous misidentification.

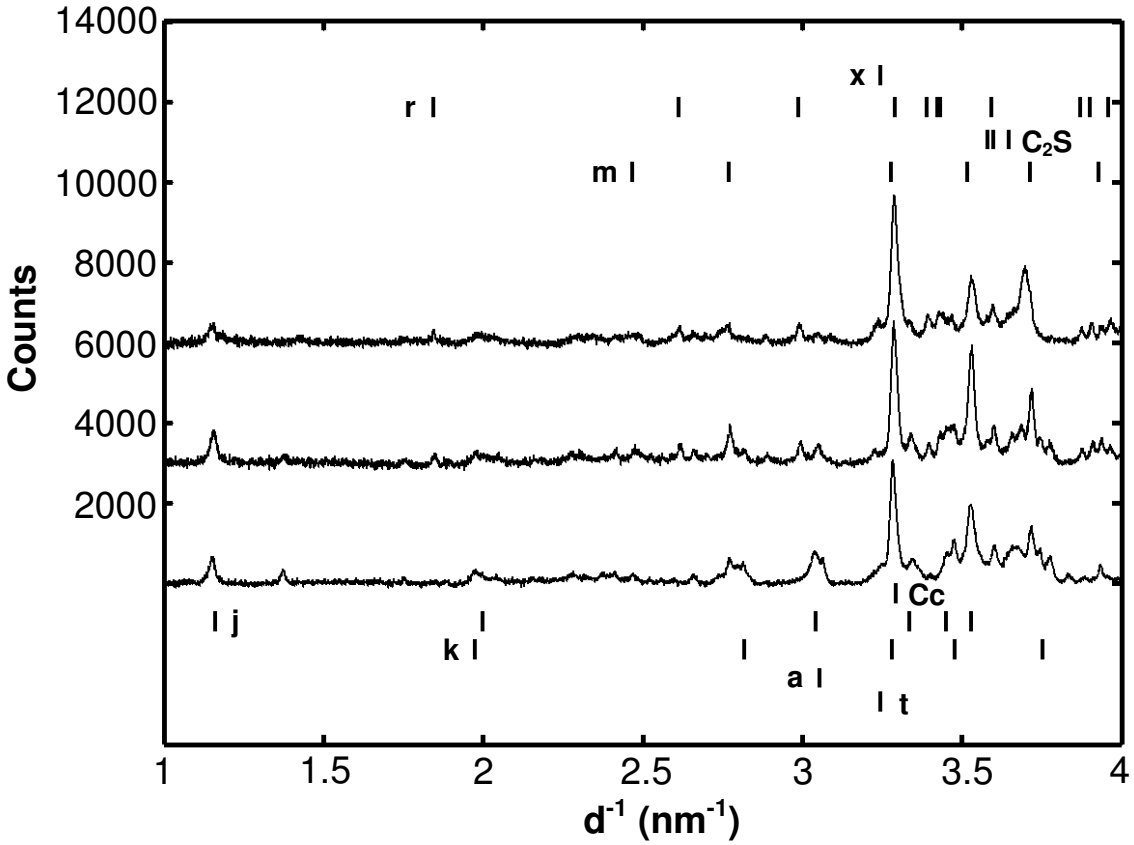

Figure II-6: XRD pattern of cement with 10 wt% of silica flour at 200 (lower), 250 (middle), 300 (upper) °C illustrating the presence of $Ca_8Si_5O_{18}$ (m), kilchoanite (k), jaffeite (j), α-$Ca_2SiO_3(OH)_2$ (a), 11Å tobermorite (t), reinhardbraunsite (r), xonotlite (x), calcite (Cc) and relict belite (β-Ca_2SiO_4) and the poorly crystalline nature of the product phases. Where C_2S corresponds to β-$Ca_2SiO_3(OH)_2$.

While $Ca_8Si_5O_{18}$ is found only in samples with silica additions and not those with alumina additions it forms a significant proportion of the sample from 10 to 25 wt % of silica flour from 200 to 350 °C (Table II-5). $Ca_8Si_5O_{18}$ is also absent from Taylor's diagram. It is possible that $Ca_8Si_5O_{18}$ is a metastable product in the system either because of the short curing period or because the impurities in the cement alter the phase boundaries of the pure system (compare Figure II-1 and Figure II-5).

II- 3.3.3 11Å Tobermorite

11Å tobermorite coexists with $Ca_8Si_5O_{18}$ in the range of silica additions from 10 to 20 wt % at 200 °C, and with xonotlite from 20 to 35 wt % of silica additions. At 250 °C 11Å tobermorite persists but only when 20 to 40 wt % of alumina is added (Figure II-7, Table II-5). Taylor's diagram suggests that 11Å tobermorite is found only to approx 150 °C but it is commonly reported in the literature that its temperature of stability can be raised by the addition of alumina [34-40]. The majority of samples were synthesised using a laboratory coarse alumina reagent; however in some cases the finer alumina was used (Table II-4). The ternary contour plot in Figure II-7 shows the amount in weight percent of 11Å tobermorite (calculated from Rietveld refinement) in samples made with coarse and fine alumina. The sample compositions (open circles) are expressed as molar proportions of the three major oxides present in the system CaO, SiO_2 and Al_2O_3. The calculated molar proportions of SiO_2 and Al_2O_3 include the amount of these oxides from the cement, and the amount added to each sample. It is clear that finer alumina promotes the formation of 11Å tobermorite.

Tobermorite is commonly reported as having a higher compressive strength and lower permeability than xonotlite [1,40,41] and so the prevalence of tobermorite in our hydroceramics suggests that the addition of alumina improves the engineering properties of the sealant, although further testing is required. It has not been able to be established which form of 11Å tobermorite is present. It has long been known that two forms of 11Å tobermorite exist: normal and anomalous [3,29]. Normal 11Å tobermorite collapses on heating to 9Å tobermorite whereas anomalous 11Å tobermorite persists to higher temperatures, its structure being supported by ions, e.g. Al^{3+}, which would not be present in the normal structure. While it has not been possible to establish exactly which form is present from the XRD patterns it is more than likely that the anomalous form is present as the presence of small amounts of additional alumina appear to encourage its formation.

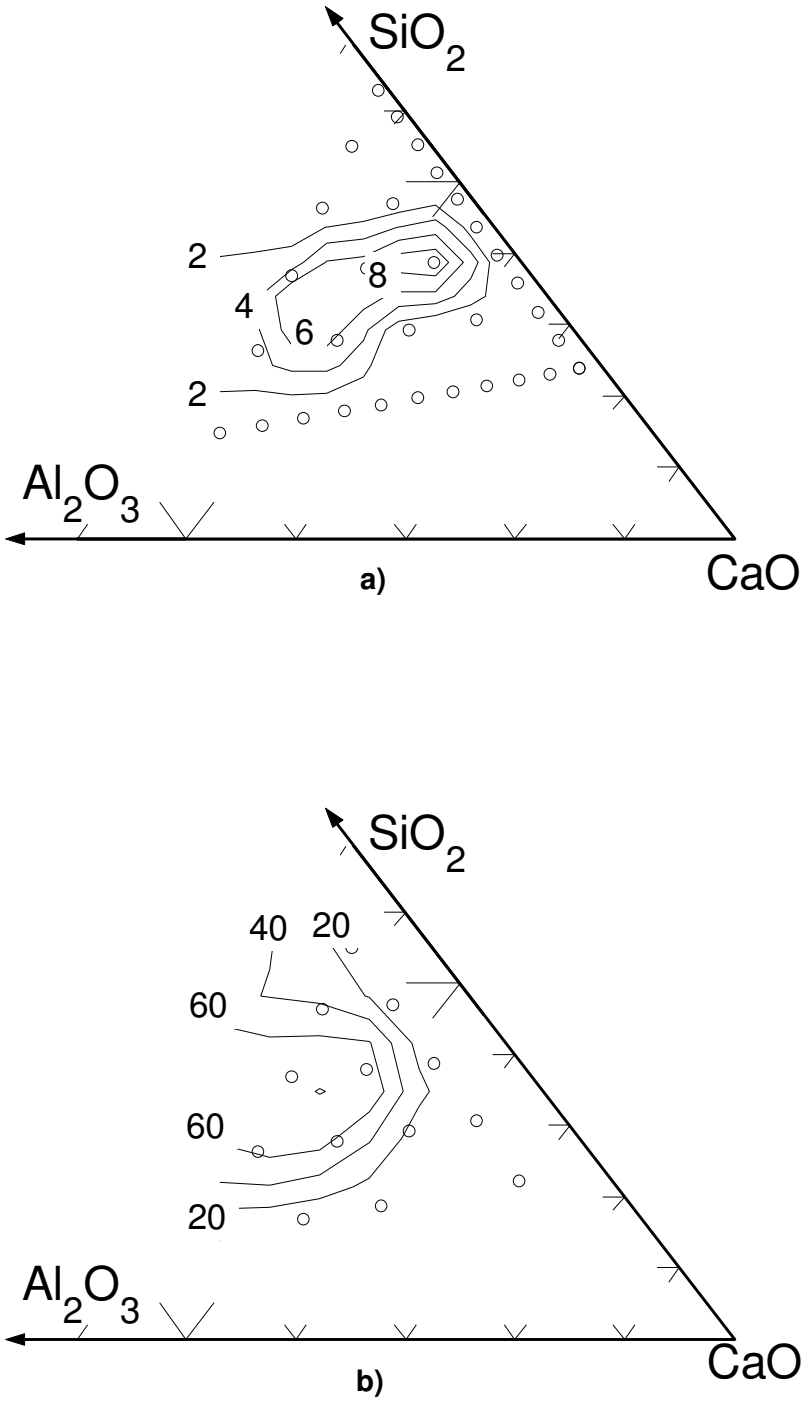

Figure II-7: Ternary plots of wt % of 11Å tobermorite with coarse (**a**) and fine (**b**) corundum. Sample points (open circles) are plotted as molar proportions of CaO, SiO_2 and Al_2O_3. Tick marks are at intervals of 0.1.

II- 3.3.4 Xonotlite

Xonotlite is present over the entire range of temperatures examined when silica flour additions exceed 10 wt % and these results are in accordance with those of Roy *et. al.* [11] who studied similar systems. The presence of alumina does not appear to increase the proportion of xonotlite formed, in contrast to the case of tobermorite. This is consistent with earlier observations [42]. However the field of stability does appear to shift to higher $CaO/(CaO+SiO_2)$ at 350 ºC, perhaps as a result of a lack of $Ca_8Si_5O_{15}$ at this temperature (Table II-5).

II- 3.3.5 Low $CaO/(CaO+SiO_2)$ hydrates: gyrolite and truscottite

The low $CaO/(CaO+SiO_2)$ phases form when silica additions exceed 30 wt %. It is found that gyrolite and truscottite coexist at 250 ºC, below which only gyrolite is present and above which only truscottite is found (Figure II-4). Taylor's diagram (Figure II-1) on the other hand indicates that gyrolite is replaced by truscottite at about 200 ºC. It is possible that this system has not reached phase equilibrium. It is also noted that the proportion of gyrolite in samples cured at 250 ºC is increased by the addition of alumina at lower silica contents; probably by the incorporation of alumina in the structure (in Chapter IV will be discussed in more detail the chemistry of gyrolite in the CASH hydroceramic system). This effect is also observed for truscottite but not to such a great extent.

II- 3.3.6 Hydrogarnet

Hydrogarnet is the most common aluminum-bearing secondary phase produced in the CASH hydroceramic system. It is most abundant when corundum is added but is present in all samples except those with silica only additions exceeding 10 wt %. To quantify hydrogarnet two patterns were used as this mineral displays solid solution from grossular (y=0) to katoite (y=3), the general formula being $Ca_3Al_2(SiO_4)_{3-y}(OH)_{4y}$. The y value is determined by measuring the d-spacing of the hydrogarnet peaks [6] and from this occupancy factors are determined for Si and H which are fed into the refinement process. Two structures are used: the Sacerdoti [24] katoite structure as default but where the y value is significantly low (<0.8) the Cohen-Addad [23] hibschite structure is used. In some samples above 250 ºC more than one hydrogarnet is present (Figure II-8) and both structures can be fitted. The lower pattern in Figure II-8 corresponds to a sample made using coarse alumina, cured at 350 ºC, with the y values of the two different hydrogarnets being 1.2

(Sacerdoti structure used) and 0.8 (Cohen-Addad structure used) respectively. The addition of fine alumina appears to promote the formation of two distinct hydrogarnets at lower temperatures. The upper pattern in Fig.7 illustrates a sample made using fine alumina, cured at 200 °C, with the *y* values being 2 and 1.4 respectively. A detailed analysis of the hydrogarnet chemistry is given in Chapter V.

However the presence of hydrogarnets in minor or trace amounts in samples with silica only additions less than 10 wt % is problematic as the peaks overlap with relict Ca_2SiO_4. This makes Rietveld refinement impossible, especially at temperatures < 300 °C. Hence although we can see small identifiable hydrogarnet peaks in these samples we cannot fit them at present and must treat hydrogarnet as zero in the quantified sample (Table II-5).

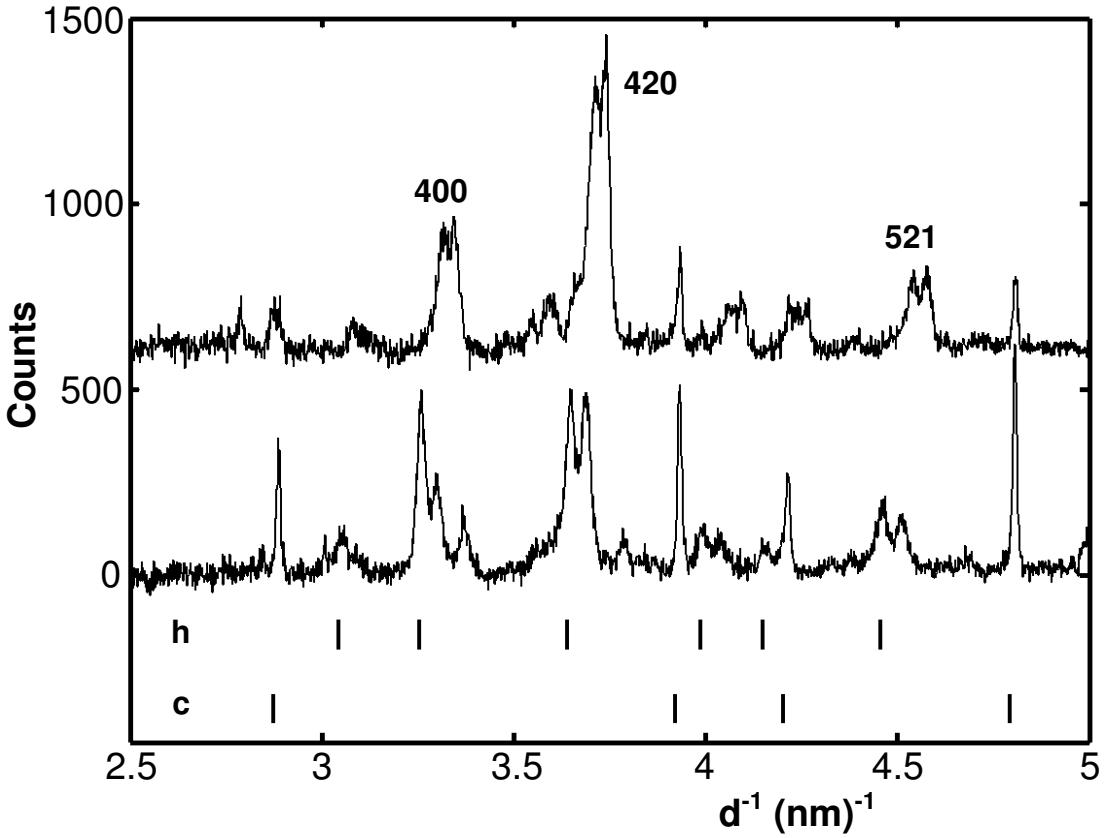

Figure II-8: Samples illustrating the presence of two distinct hydrogarnets (*h*) with split 400, 420 and 521 peaks. Some relict corundum is present (*c*). The lower sample was synthesised at 200 °C and contains 10 wt % of silica flour and 30 wt % of fine corundum. The upper sample was synthesised at 350 °C and contains 20 wt % of silica flour and 10 wt % of corundum.

II- 3.3.7 Other phases

Not all the phases present have been described above. Relict corundum and silica are observed in some samples, particularly where additions are high (Table II-4 and Table II-5). The temperature does not appear to increase corundum consumption but silica consumption does increase with increasing temperature. However it also appears that further additions of either silica or corundum add little value to the product as relict corundum or quartz are observed in the diffraction pattern. Indeed it seems that additions of > 50 wt % of corundum add little value in terms of product phases.

Other phases present either in small quantities or in few samples are kilchoanite and foshagite. Kilchoanite is observed in four samples (Figure II-6, Table II-5) at 200 °C. This is at odds with Taylor's diagram (Figure II-1) where it is observed in the pure system at temperatures only in excess of 500 °C. However Taylor [3] stated that kilchoanite has been noted with other products from hydrothermal treatment of afwillite at temperatures little above 200 °C. Therefore the presence of this anhydrous mineral in hydroceramics should be expected. It is probably a metastable phase in our system because of the short curing period.

Foshagite is observed in two samples at 350 °C (Table II-5). According to Taylor's diagram it would be expected at lower temperatures than this but its formation is probably being prevented by the presence of $Ca_8Si_5O_{18}$ whose CaO/SiO_2 ratio is not dissimilar (0.57 vs. 0.62).

II- 3.4 Cautionary notes

Small amounts of carbonate (calcite $CaCO_3$) are observed in most samples (Figure II-6). The amount of carbon dioxide in the autoclave is not sufficient to form the amounts observed (typically < 10 %). Therefore it must result either from the water used (which was not deaerated) or from exposure to the atmosphere during cooling and dehydration. Although samples were dried under vacuum we were unable to completely prevent the formation of carbonate. The carbonate is not quantified for simplicity, hence small mismatches in $CaO/(CaO+SiO_2)$ or $CaO/(CaO+Al_2O_3)$ may also be explained by the presence of minor or trace amounts of carbonate in the system.

Unreacted belite β-Ca_2SiO_4 is also present in some samples (Figure II-6). Quantification of this phase in the hydrated samples is difficult as peaks are broad, and frequently overlap peaks from other phases, notably those of hydrogarnet.

Partial Ca_2SiO_4 hydrates have been observed using the electron microprobe (see Chapter III) but no satisfactory ICDD pattern or crystal structure exists for these phases. Once again for simplicity and because of fitting difficulties the relict Ca_2SiO_4 phase has not been quantified.

With regards to phase identification, not all peaks can satisfactorily be identified. The system is extremely complex, sometimes containing five or more product phases (Figure II-6, Table II-4 and Table II-5). It has already been noted the many differences between the stability fields of the pure system (Figure II-1) and the samples synthesised with real cement. It is unlikely that we have always succeeded in identifying every phase which can form under hydrothermal conditions in the CASH system.

Lastly it should be noted that the samples used in this study were only hydrated for 5 days. Samples synthesised over shorter periods of time [12] do display intermediate products and it is uncertain at present whether the phases displayed in these samples are the final product phases or are intermediate phases of a much longer hydration process.

II- 4. Conclusions

A comparison has been made between the pure $CaO\text{-}SiO_2$ system of Taylor (Figure II-1) with that produced from a system consisting of cement and silica (Figure II-4) more representative of practical formulations over the temperature range 200 to 350 °C. While many phases appear to be stable at similar temperatures (portlandite, jaffeite, hillebrandite, reinhardbraunsite and xonotlite) there are numerous deviations from the pure system when using real cements:

The stability of $\alpha\text{-}Ca_2SiO_3(OH)_2$ is extended to < 250 °C. In addition $Ca_8Si_5O_{18}$, not observed by Taylor, forms a large proportion of the sample when 10 to 20 wt % of silica flour is added.

The stability of 11Å tobermorite is greatly extended from 170 °C to < 300 °C.

When alumina is added to the system, not only are aluminum bearing phases dominant (Figure II-5), but the stability fields of nominally Al-free phases are extended, both in terms of composition and temperature range. Thus:

Hydrogarnet is the dominant Al-bearing product phase in the system. The broad peaks suggest that a range of compositions is present within any one sample and some samples display more than one distinct composition.

At > 250 °C hydrogarnet is replaced by $Ca_4Al_6O_{13}•3H_2O$.

At > 300 °C hydrogarnet is replaced by both $Ca_4Al_6O_{13}•3H_2O$ and bicchulite.

The presence of alumina, particularly fine grained alumina, pushes the stability field of 11 Å tobermorite and gyrolite to higher temperatures.

II- 5. References

1. E. Nelson,"*Well Cementing*" Sugar Land, Texas, Schlumberger Educational Services, 1990.

2. G. Carter and D. K. Smith, "Properties of cementing compositions at elevated temperatures and pressure," *Transactions of the Metallurgical Society of the American Institute of Metallurgical Engineers,* **213** [2] 20-26 (1958).

3. H. F. W. Taylor, "The calcium silicate hydrates", pp. 168-232 in *The Chemistry of Cements,* **Vol. 1.** Edited by H. F. W. Taylor. Academic Press, London, 1964.

4. V. Barlet-Gouédard, S. Danican, E. Nelson, and C. Cambus, "Cement compositions for high temperature applications." In *PCT Patent Application***.** 2003.

5. V. Barlet-Gouédard and B. Vidick, "A non-conventional way of developing cement slurry for geothermal wells," *Geothermal Resources Council Transactions,* **25** 85-91 (2001).

6. N. Meller, C. Hall, K. Kyritsis, and G. Giriat, "Synthesis of cement based CaO-Al_2O_3-SiO_2-H_2O (CASH) hydroceramics at 200 and 250 °C: Ex-situ and in-situ diffraction " *Cement and Concrete Research,* **37** [6] 823-833 (2007).

7. N. Meller, C. Hall, and J. Phipps, "A new phase diagram for the CaO-Al_2O_3-SiO_2-H_2O hydroceramic system at 200 °C," *Materials Research Bulletin,* **40** [5] 715-723 (2005).

8. N. Meller and C. Hall, "Hydroceramic sealants for geothermal wells"; pp.281-284 in the *Proceedings of the International Congress on Applied Mineralogy*. Edited by M. Pecchio, F. R. D. Andrade, L. Z. D. D'Agostino, H. Kahn, L. M. Sant'Agostigno, and M. M. M. L. Tassinari. Sao Paolo, Brazil, 2004.

9. E. L. White, C. A. Langton, M. W. Grutzeck, and D. M. Roy, "High temperature cements for geothermal applications," *American Ceramic Society Bulletin,* **58** [3] 334 (1979).

10. D. M. Roy, C. A. Langton, M. W. Grutzeck, and E. L. White, "Hydrothermal high temperature cements for potential geothermal applications"; in *Proceedings of the 5th International Symposium on Oilfield and Geothermal Chemistry*. Stanford, California, 1980.

11. D. M. Roy, E. L. White, C. A. Langton, and M. W. Grutzeck, "Potential new high temperature cements for geothermal wells"; in *Proceedings of the International Symposium on Oilfield and Geothermal Chemistry*. Houston, Texas, 1979.

12. C. Hall and K. L. Scrivener, "Oilwell cement clinkers-X-ray microanalysis and phase composition," *Advanced Cement Based Materials,* **7** [1] 28-38 (1998).

13. M. M. Woolfson,"*An introduction to X-ray crystallography*" Cambridge, UK, Syndics of the Cambridge University Press, 1970.

14. A. Guinier,"*X-Ray Diffraction: In crystals, imperfect crystals, and amorphous bodies*" New York, Courier Dover Publications, 1994.

15. K. L. Scrivener, T. Fullmann, E. Gallucci, G. Walenta, and E. Bermejo, "Quantitative study of Portland cement hydration by X-ray diffraction/Rietveld analysis and independent methods," *Cement and Concrete Research,* **34** [9] 1541-1547 (2004).

16. A. Le Bail, "Modelling the silica glass structure by the Rietveld method," *Journal of Non-Crystalline Solids,* **183** [1-2] 39-42 (1995).

17. T. Yano, K. Urabe, H. Ikawa, T. Teraushi, N. Ishizawa, and S. Udagawa, "Structure of a-dicalcium silicate," *Acta Crystallographica,* **C49** 1555-1559 (1993).

18. S. E. Dann, P. J. Mead, and M. T. Weller, "Loewensteins rule extended to an aluminium rich framework. The structure of bicchulite, $Ca_8(Al_2SiO_6)_4(OH)_8$, by MAS NMR and neutron diffraction," *Inorganic Chemistry,* **35** [6] 1427-1428 (1996).

19. V. I. Ponomarev, D. M. Kheiker, and N. V. Belov, "Crystal structure of tetracalcium trihydrotrialuminate $C_4A_3H_3$," *Doklady Akademii Nauk SSSR,* **194** 1072-1075 (1970).

20. J. A. Gard and H. F. W. Taylor, "The crystal structure of foshagite," *Acta Crystallographica,* **13** 785-793 (1960).

21. S. Merlino, "Gyrolite: its crystal structure and crystal chemistry," *Mineralogical Magazine,* **52** [366] 377-387 (1988).

22. Y. Dai and J. E. Post, "Crystal structure of hillebrandite: a natural analogue of calcium silicate hydrate (CSH) phases in Portland cement," *American Mineralogist,* **80** [7-8] 841-844 (1995).

23. C. Cohen-Addad, P. Ducros, and E. F. Bertaut, "Etude de la substitution du groupement SiO_4 par $(OH)_4$ dans les composes $Al_2Ca_3(OH)_{12}$ et $Al_2Ca_3(SiO_4)_2.16(OH)_{3.36}$ de type grenat," *Acta Crystallographica,* **23** 220-230 (1967).

24. M. Sacerdoti and E. Passaglia, "The crystal structure of katoite and implications within the hydrogrossular group of minerals," *Bulletin de Mineralogie,* **108** [1] 1-8 (1985).

25. N. A. Yamnova, K. H. Sarp, Y. K. Egorov-Tismenko, Y. D. Pushcharovski, and G. Dasgupta, "Crystal structure of jaffeite," *Crystallography reports,* **38** [4] 464-467 (1993).

26. H. F. W. Taylor, "The crystal structure of kilchoanite, $Ca_6(SiO_4)(Si_3O_{10})$, with some comments on related phases," *Mineralogical Magazine,* **38** [293] 26-31 (1971).

27. H. E. Petch, "The hydrogen positions in portlandite, $Ca(OH)_2$, as indicated by the electron distribution," *Acta Crystallographica,* **14** [9] 950-957 (1961).

28. T. P. Kuznetsova, N. N. Nevskii, V. V. Ilyukin, and N. V. Belov, "Refinement of the crystal structure of calcium chondrodite $Ca_5(SiO_4)_2(OH)_2$ and $Ca(OH)_2(Ca_2SiO_4)_2$," *Kristallografiya,* **25** [1] 159-160 (1980).

29. S. Merlino, E. Bonaccorsi, and T. Armbruster, "The real structure of tobermorite 11Å: normal and anomalous forms, OD character and polytypic modifications," *European Journal of Mineralogy,* **13** [3] 577-590 (2001).

30. S. Merlino, "The structure of reyerite, $(Na,K)_2Ca_{14}Si_{22}Al_2O_{58}(OH)_8(H_2O)_2$," *Mineralogical Magazine,* **52** [365] 247-256 (1988).

31. K. S. Mamedov and N. V. Belov, "The crystal structure of the minerals of the wollastonite group. 1. Structure of xonotlite," *Zapiski Vsesoyuznogo Mineralogicheskogo Obscchestva,* **85** 13-38 (1956).

32. J. M. Bennet, J. A. Gard, K. Speakman, and H. F. W. Taylor, "$Ca_8Si_5O_{18}$ and the nature of γ-dicalcium silicate hydrate," *Nature,* **209** 1127 (1966).

33. X. Hu, K. Yanagisawa, A. Onda, and K. Kajiyoshi, "Effects of hydrothermal process on formation of calcium silicate hydrates at 250 °C," *Journal of the Society of Inorganic Materials Japan,* **13** [320] 32-39 (2006).

34. N. Meller, C. Hall, K. Kyritsis, G. Giriat, H. J. Jakobsen, and J. Skibsted, "Incorporation of aluminium guest ions in nominally alumina-free calcium silicate hydrates: effects on crystal structure and thermal stability"; in *Proceedings of the Proceedings of the 12th International Congress on the Chemistry of Cement*. Edited by J. J. Beaudoin, J. M. Makar, andL. Raki. Montreal Canada, 2007.

35. F. Liu, D. Chen, W. Ni, and Z. Cao, "Effect of Al^{3+} on tobermorite crystallinity," *Journal of University of Science and Technology Beijing,* **7** [2] 79-81 (2000).

36. D. S. Klimesch and A. S. Ray, "DTA-TGA evaluations of the CaO-Al_2O_3-SiO_2-H_2O system treated hydrothermally," *Thermochimica Acta,* **334** [1-2] 115-122 (1999).

37. D. S. Klimesch and A. S. Ray, "Effects of quartz particle size on hydrogarnet formation during autoclaving at 180 °C in the CaO-Al_2O_3-SiO_2-H_2O system," *Cement and Concrete Research,* **28** [9] 1309-1316 (1998).

38. N. Isu, H. Ishida, and T. Mitsuda, "Influence of quartz particle size on the chemical and mechanical properties of autoclaved aerated concrete (I) Tobermorite formation," *Cement and Concrete Research,* **25** [2] 243-248 (1995).

39. T. Sugama, L. E. Kukacka, and W. Horn, "Effects of tobermorite and calcium silicate hydrate (I) crystals formed within polymer concretes " *Journal of Materials Science,* **16** 345-354 (1980).

40. G. L. Kalousek and S. L. Chow, "Research on cements for geothermal and deep oil wells," *Society of Petroleum Engineers of AIME,* SPE 5940 (1976).

41. L. D. Sanders and W. J. Smothers, "Effect of tobermorite on the mechanical strength of autoclaves Portland cement-silica mixtures," *Journal of the American Concrete Institute,* **28** 127-134 (1957).

42. K. Luke, H. F. W. Taylor, and G. L. Kalousek, "Some factors affecting formation of truscottite and xonotlite at 300-350 °C," *Cement and Concrete Research,* **11** [2] 197-203 (1981).

43. K. Kyritsis, N. Meller, and C. Hall, "Chemistry and morphology of hydrogarnets formed in cement pastes cured at 200 ˚C to 350 ˚C," (submitted to Journal of the American Ceramic Society).

CHAPTER III

MINERALS WITH HIGH CaO/SiO_2 MOLE RATIO

III- 1. Introduction

Minerals with high CaO/SiO_2 mole ratio are present in the CASH hydroceramic system in neat cement samples and when less than 20 wt % of silica flour is added at temperatures between 200 ℃ and 3 50 ℃. The chemistry and the crystal shape of some of the major minerals with high CaO/SiO_2 mole ratio that are present in this system, such as alpha dicalcium silicate hydrate (α-$Ca_2SiO_4 \bullet (H_2O)$), jaffeite ($Ca_6(Si_2O_7)(OH)_6$) and reinhardbrausite ($Ca_5(SiO_4)_2(OH)_2$), will be discussed in this chapter. Using electron probe microanalysis it will be determined if any other phases are present which cannot be identified by X-ray diffraction. In addition we will try to determine where the minor elements that cement contains, such as iron, aluminium, magnesium, sulphur and potassium, are distributed.

Finally scanning electron microscopy and a simulation software, called WinXmorph, will be used to determine the crystal shape of those minerals with high CaO/SiO_2 ratio. Samples studied in detail are neat cement cured at 200 and 250℃ and cement with 10 wt % of silica flour cured at 300 ℃.

III- 2. Characterization techniques

III- 2.1 Electron Probe Microanalysis (EPMA)

III- 2.1.1 Principle

Electron probe microanalysis (EPMA) is a fully quantitative method for elemental analysis of micro-sized volumes at the surface of materials, with sensitivity at the level of ppm. It is the most precise and accurate micro-analysis technique available and elements ranging from beryllium to uranium can be analyzed. In EPMA high velocity electrons are generated under high vacuum conditions from a filament (usually made from tungsten). These electrons are focused through a series of electromagnetic lenses into a very narrow beam with a typical energy of 5 to 30 keV. When the electron beam impacts the sample, elements in the sample emit X-rays whose wavelength is characteristic of a particular element. Hence the sample composition can be easily identified by recording WDS spectra (Wavelength Dispersive Spectroscopy). WDS spectrometers are based on the Bragg's law and use various moveable, shaped monocrystals as monochromators. By comparing the intensities of these lines with those emitted from

standards (of known composition) it is possible to determine the concentrations of the elements to accuracy around ± 1 %. Wavelength discriminating X-ray detectors are the most quantitative because their signal to noise ratio is high and they have excellent wavelength resolution. The high signal to noise ratio also implies higher sensitivity to minor and trace elements. Disadvantages are that X-ray measurements is time consuming and since the elements of interest have to be tuned this implies they need to be first anticipated [1-3].

III- 2.1.2 Experimental conditions

The electron microprobe was used to obtain the accurate composition of some of phases in the hydroceramic samples. A piece was taken from the sample, mounted in epoxy resin, polished (to a finish of 0.25 μm) to be planar and relief free, and then coated with carbon. The analyses were carried out using a WDS electron microprobe system (Cameca SX 100) at the University of Edinburgh (School of Geosciences) with five crystal spectrometers. The microprobe operated with an accelerated potential of 10 kV, a sample current of 10 nA measured on brass and a beam size of approximately 1 μm. The counting time on the background was 10 sec and the reduction algorithm operated was the PAP [4,5]. The standards used (for the Kα lines of all elements) were: wollastonite for Ca and Si; spinel for Al and Mg; fayalite for Fe; and celestite for SO_3.

III- 2.2 Scanning Electron Microscopy (SEM)

III- 2.2.1 Principle

Scanning electron microscope (SEM) is very similar to electron microprobe analysis but it is designed primarily for imaging rather than analysis. In SEM a beam of electrons is generated by heating a filament made of tungsten wire. This filament functions as the cathode. During operation the filament and its heating supply are maintained at a high negative potential by the high voltage supply. At the operating temperature, electrons are emitted from the V- shaped filament towards the anode. The anode is positive with respect to the filament - this forms powerful attractive forces for electrons. A hole in the anode allows a fraction of these electrons to continue down the column. The beam is then focussed on to the sample by electromagnetic lenses. The electron beam hits the sample, producing, among others, secondary and backscattered electrons from the sample. These electrons

are collected by a secondary electron or a backscattered electron detector, converted to a voltage, and amplified. SEM has the advantage of offering high spatial resolution images (~5 nm) with a large depth of focus. It is generally fitted with an energy dispersive spectrometer (EDS) which provides easy and rapid qualitative compositional information derived from the emitted X-rays. The approximate penetration depth of the beam is ~1 µm [2,6].

III- 2.2.2 Experimental conditions

The scanning electron microscope was used to image the crystals grown in the hydroceramic samples. A Hitachi 4700 II cold field-emission SEM was used based at the University of Edinburgh (School of Biological Sciences). The acceleration voltage used was 5 kV and the samples were sputter-coated with approximately 8 nm of 60 % gold and 40 % palladium in order to minimize charging.

III- 2.3 WinXmorph

WinXmorph is a computer software that can simulate the shape of a crystal. This program takes as inputs the crystallographic parameters of a phase such as the point group, the unit cell parameters, the Miller indices and the central distances and produces the possible crystal shapes. The last two parameters can be edited freely and the input is automatically corrected [7,8]. This program has previously been used to simulate molecular crystals [9] but according to my knowledge it is used here for the first time for cement hydration products. In this study the data of the simulated crystals has been obtained from the International Crystal Structure Database (ICSD).

III- 3. Results and discussion

III- 3.1 Belite and its alteration products

Belite constitutes 21 wt % of the oilwell cement that has been used in this study (see Chapter II, Table II-1). Using electron probe microanalysis, unreacted belite has been detected when curing cement only at 200 ℃ for 5 days. The amount of this phase must be very small as it has not been detected from the X-ray diffraction (results discussed in Chapter II) and only one grain of totally unhydrated belite was found in the whole sample (Figure III-1). The presence of belite, or

dicalcium silicate (Ca_2SiO_4), is not wholly unexpected as it is known that it reacts slowly with water [10]. Therefore a very small amount of belite remained unhydrated after 5 days in the autoclave cell. The backscattered image in Figure III-1 (taken using EPMA) shows a belite grain, in cement only sample cured at 200 ℃, and the three different points that have been analyzed with EPMA. In Figure III-2 the image is taken using SEM illustrating more clearly a similar belite grain found in the same sample. In both images the characteristic belite striations are clearly seen. It has been reported that very common type of belite grain in production clinkers, called Type I belite, is rounded, with a mean dimension typically 20 to 40 μm, and shows several sets of parallel striations [10-12]. This is clearly illustrated in both Figures III-1 and 2.

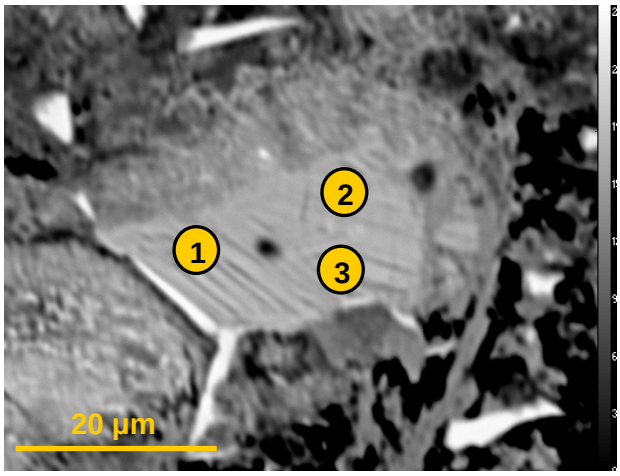

Figure III-1: EPMA backscattered image showing a belite grain. Sample contains cement only and cured at 200 ℃.

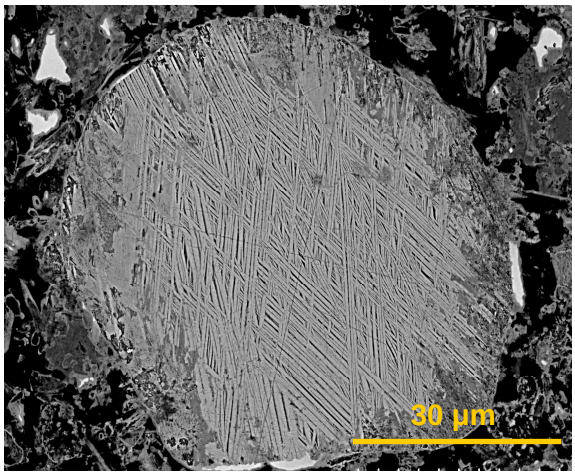

Figure III-2: SEM backscattered image of a similar grain found in sample containing cement only and cured at 200 °C.

The average results are shown in Table III-1. The calculation of the formula is based on 4 oxygens, details of calculation can be found in Appendix III. The weight percent of the oxides CaO and SiO_2 in Table III-1 are in very good agreement with that of the pure Ca_2SiO_4 (34.9 % SiO_2 and 65.1 % CaO). In addition the CaO/SiO_2 mole ratio is in very good agreement with experimental previous analysis of belite grains in ordinary Portland cement pastes [13,14]. Moreover the EPMA reveals the presence of two other elements in the structure of belite, namely Al and Fe^{3+} with the chemical formula being:

$$Ca_{1.99}\ (Al_{0.04}Fe_{0.035}Si_{0.95})\ O_4$$

Table III-1: Electron probe microanalysis results from a belite grain found in cement only sample cured at 200 ℃. In this table are presented electron probe results from belite grains found in clinker from Hall *et al.* [15] for comparison. A typical error between these measurements is less than 3.5 %.

Weight percent of oxides						
CaO	SiO_2	Al_2O_3	Fe_2O_3	H_2O		
63.78	32.4	1.27	1.6	-		
Formula based on 4 oxygens						
Ca	Si	Al	Fe^{3+}	H	Ca/Si	Al/Fe
1.99	0.95	0.04	0.035	-	2.1	1.14
Wt % of oxides after Hall *et al.* [15]						
CaO	SiO_2	Al_2O_3	Fe_2O_3	H_2O		
63.49	31.64	1.45	1.63	-		

The presence of these two elements is not rare in dicalcium silicates as it has been reported that the structure can be modified by ionic substitutions and that at ordinary pressures five polymorphs exist [16]. Normally in Portland cements belite is present wholly or largely as the β-polymorph which has a monoclinic crystal structure [17]. Clinker belites usually contain 4-6% of substituted oxides the majority of which are usually Al_2O_3 and Fe_2O_3 [10]. The source is the raw materials used to produce these clinkers. The Al_2O_3/Fe_2O_3 ratio in Table III-1 is in good agreement with experimental results reported from Hall *et al.* [15] regarding clinker belites and with computational results from the modified Bogue composition (Appendix II). Nuclear magnetic resonance (NMR) carried out on synthetic belites by Hall *et al.* [15] and Skibsted *et al.* [18] suggest that Al substitutes exclusively Si.

In addition sulphur and magnesium has been reported that can be present in the belite structure [19] and that a coupled substitution probably occurs between $2Al^{3+} + S^{6+}$ for $3Si^{4+}$ [20]. The sulphur content ($SO_{3(b)}$) is also related to that of the clinker ($SO_{3(c)}$) by the relation

$$SO_{3(b)} = 1.23(SO_{3(c)}) = 0.24 \qquad \textbf{(III- 1)}$$

and that a correlation exists between MgO and Al_2O_3/Fe_2O_3 ratio [15,21]. Although none of the above elements have been found in our study; possibly the lack of

measurements on the specific phase might incorporate an error when calculating these elements.

III- 3.1.1 Alpha-dicalcium silicate hydrate (α-Ca_2SiO_4•(H_2O))

Alpha-dicalcium silicate hydrate is present in samples containing cement only and cured at 200 and 250 ℃. It is also present when adding less than 15 wt % silica flour to the system (Chapter 2) at 200 ℃. The chemistry of α-Ca_2SiO_4•(H_2O) examined using EPMA, in neat cement samples cured at 200 and 250 ℃. The backscattered image in Figure III-3 taken from the EPMA (sample containing cement only, cured at 200 ℃) presents the points that this grain has been analyzed. The analysis for alpha-dicalcium silicate hydrate is based on 5 oxygens and the weight percent of water is calculated as the difference from 100% of the total. A typical error between these measurements is less than 6 %. The results in Table III-2 shows that the inner part of this grain (points 6, 7, 8, 9) is dicalcium silicate partially hydrated with the chemical formula being:

$$(Ca_{1.86}K_{0.02}Mg_{0.01})_{\Sigma=1.89}\,(Si_{0.85}Al_{0.05}Fe_{0.04}S_{0.01})_{\Sigma=0.95}\,O_{4.08}\,H_{0.5}$$

The outer part of this grain (points 1, 2, 3, 4, 5) is alpha dicalcium silicate hydrate with a chemical formula being:

$$(Ca_{2.01}K_{0.01}Mg_{0.01})_{\Sigma=2.03}\,(Si_{0.9}Al_{0.04}Fe_{0.04}S_{0.01})_{\Sigma=0.99}\,O_{4.98}\,H_{2.01}$$

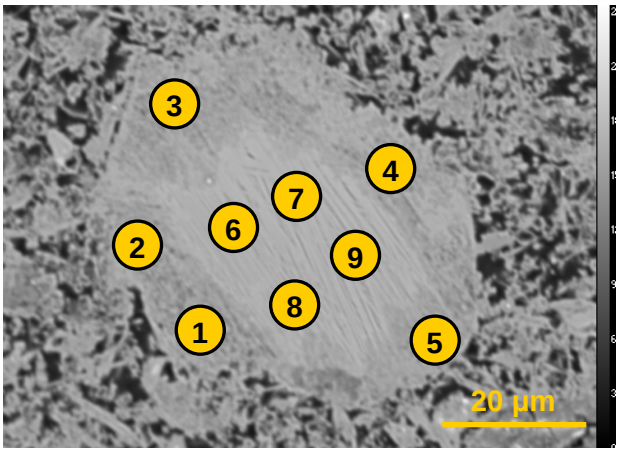

Figure III-3: EPMA analysis on grain found in cement only cured at 200 ℃. The rim of the grain is α-Ca_2SiO_4•(H_2O) and the inner of the core in Ca_2SiO_4 partially hydrated. The numbered yellow circles correspond to probe measurements.

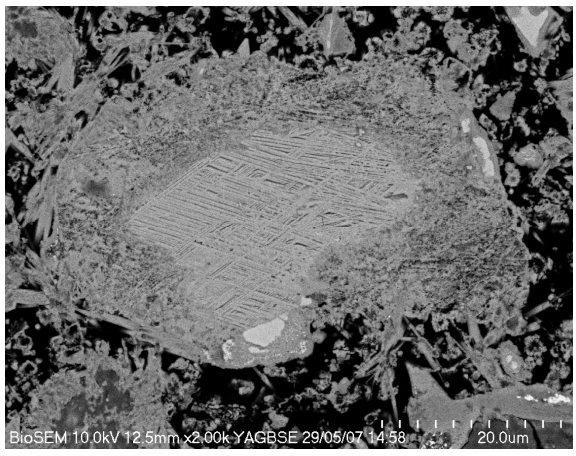

Figure III-4: SEM backscattered image of a similar grain found in sample containing cement only and cured at 200 ℃.

The backscattered image in Figure III-4, taken from the SEM, illustrates more clearly the progress of the belite alteration on a single grain. The inner part of the grain consists of striations (typical belite texture as seen in section III-3.1), which is belite partially hydrated, whereas the rims of the grain are hydrated belite in the form of α-$Ca_2SiO_4 \bullet (H_2O)$.

Another observation is the way that the hydration reaction proceeds in Figure III-4 as it starts at the rims of the grain moving inwards. Such processes, called dissolution-reprecipitation, have been reported and clearly monitored in mineral replacement reactions. In these processes when a solid is in contact with an aqueous solution, dissolution of even a few monolayers of the parent surface occurs. This may result in a fluid boundary layer which is supersaturated with respect to a more stable solid phase. The nucleation of the product phase (in this case α-$Ca_2SiO_4 \bullet (H_2O)$) on the parent surface (belite) will depend on different factors such as the nucleation kinetics and the degree of epitaxy between the two solids. The epitaxial nucleation is responsible for transferring the crystallographic information from the parent to the product [22,23].

However Putnis [22] in his review paper suggests that the continuation of the transformation reaction depends on keeping open fluid transport pathways to the reaction interface between parent and product solids. This means that porosity must be generated in the product phase. The generation of porosity according to Putnis depends on two factors: the relative molar volume of the two solid phases and the relative solubility of the two phases in the fluid. In this case the solubility of these phases in water is very slow, however a calculation of the molar volume (V_m) has been carried out.

$$\underset{V_m = 53.38}{\mathbf{Ca_2SiO_4}} \quad + \quad \underset{V_m = 19.64}{\mathbf{H_2O}} \quad \rightarrow \quad \underset{V_m = 71.38}{\mathbf{Ca_2(SiO_3OH)(OH)}}$$

The total molar volume of belite plus water is higher than the product phase (alpha dicalcium silicate hydrate) as seen from the chemical equation above resulting in porosity (in Figure III-4 the rim of the grain is porous). Therefore the continuation of the hydration reaction may occur. The above example shows that the conditions met in mineral replacement are possible to occur during the hydration of cement.

The weight percent of the oxides of alpha-dicalcium silicate hydrate from the EPMA is in very good agreement with the ideal phase (58.5 % CaO, 32.04 % SiO_2 and 9.46 % H_2O) as well as the CaO/SiO_2 mole ratio. The presence of other elements in the structure (Mg, Al, Fe, and S) is not unusual as belite can incorporate these elements in its structure (see section 3.1). However Equation III-1 for sulphur and the correlation for magnesium between Al_2O_3/Fe_2O_3 ratio can not applied in this study due to other phases present and their ability of incorporating any of these elements in their structure. The presence of potassium is rare although studies indicate that synthetic belites can be substituted with K_2O up to 1.2 % [24].

Table III-2: EPMA analysis of α-Ca_2SiO_4•(H_2O) grain present in sample containing cement only, cured at 200 ℃.

Mineral	**Ca_2SiO_4•x(H_2O) partially hydrated**	**α-Ca_2SiO_4•H_2O**
	Weight percent of oxides	
CaO	61.95	58.79
MgO	0.25	0.34
K_2O	0.65	0.40
SiO_2	30.78	28.78
Al_2O_3	1.56	0.94
Fe_2O_3	1.62	0.98
SO_3	0.35	0.36
H_2O	2.84	9.41
	Formula based on 4.08 oxygens	**Formula based on 5 oxygens**
Ca	1.86	2.01
Mg	0.01	0.01
K	0.02	0.01
Si	0.85	0.90
Al	0.05	0.04
Fe^{3+}	0.04	0.04
S	0.01	0.01
H	0.50	2.01
Ca/Si	2.18	2.23

At 250 ℃ similar belite grains have been found (Figure III-5) and analysed using EPMA. The procedure calculating the formula in Table III-3 is the same as previously and the results are similar to those at 200 ℃. The inner part of the grain consists of partially hydrated dicalcium silicate with the chemical formula being:

$$(Ca_{1.9}K_{0.02}Mg_{0.01})_{\Sigma=1.93}\ (Si_{0.89}Al_{0.04}Fe_{0.03}S_{0.01})_{\Sigma=0.97}\ O_{4.05}\ H_{0.35}$$

The outer part is hydrated alpha dicalcium silicate and the calculated formula is:

$$(Ca_{2.0}K_{0.01}Mg_{0.02})_{\Sigma=2.03}\ (Si_{0.87}Al_{0.04}Fe_{0.03}S_{0.01})_{\Sigma=0.95}\ O_{4.95}\ H_{1.99}$$

The CaO/SiO_2 mole ratio of α-$Ca_2SiO_4\bullet(H_2O)$ at 250 ℃ is in very good agreement with the ideal phase and the minor elements present in the structure have similar values with those found at 200 ℃. Therefore the in crease of temperature does not seem to affect the chemistry of this phase.

Table III-3: EPMA analysis of α-$Ca_2SiO_4\bullet(H_2O)$ grain present in sample containing cement only, cured at 250 ℃.

Mineral	**$Ca_2SiO_4\bullet x(H_2O)$ partially hydrated**	**α-$Ca_2SiO_4\bullet H_2O$**
	Weight percent of oxides	
CaO	62.95	59.55
MgO	0.19	0.32
K_2O	0.44	0.15
SiO_2	31.42	27.57
Al_2O_3	1.26	1.20
Fe_2O_3	1.37	1.00
SO_3	0.28	0.31
H_2O	2.09	9.90
	Formula based on 4.05 oxygens	**Formula based on 5 oxygens**
Ca	1.90	2.00
Mg	0.01	0.02
K	0.02	0.01
Si	0.89	0.87
Al	0.04	0.04
Fe^{3+}	0.03	0.03
S	0.01	0.01
H	0.35	1.99
Ca/Si	2.13	2.29

Figure III-6 is a similar grain found in neat cement cured at 250 ℃, again clearly illustrating hydration of the belite phase.

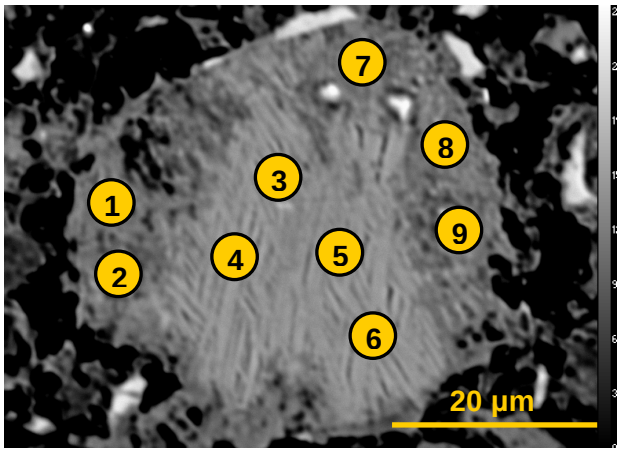

Figure III-5: EPMA analysis on grain found in cement only cured at 250 °C. The rim of the grain is α-Ca_2SO_4•(H_2O) and the inner of the core in Ca_2SiO_4 partially hydrated.

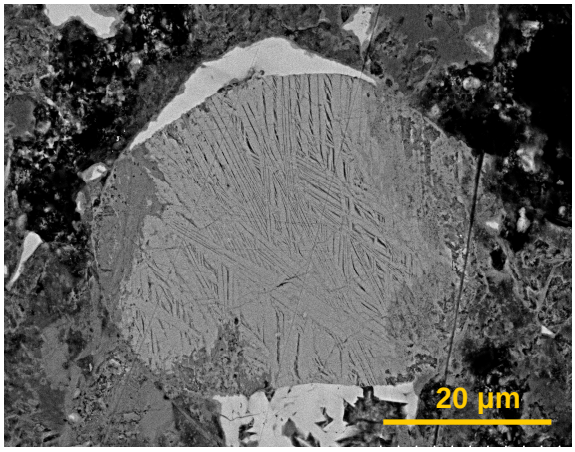

Figure III-6: SEM backscattered image of a similar grain found in sample containing cement only and cured at 250 ℃.

III- 3.2 Jaffeite $Ca_6(Si_2O_7)(OH)_6$

Jaffeite or tricalcium silicate hydrate (TSH) as it is known in cement chemistry, is the phase that is regularly met in the CASH hydroceramic system (Chapter 2) [25]. The chemistry of this phase has been studied using EPMA in neat cement samples cured at 200 and 250 ℃ which contain jaffeite in high amounts (>70 %). The analysis is based on 13 oxygens and the weight percent of water is calculated as the difference from 100 % of the total. A typical error between these measurements is less than 7.5 %.

The results in Table III-4 show that the weight percent of the major oxides as well as the CaO/SiO_2 mole ratio are in very good agreement with that of the pure phase (65.88 % CaO, 23.52 % SiO_2 and 10.58 % H_2O) at both temperatures. In addition EPMA measurements that have been carried out on natural samples from the Kombat Mine, Nambia [26] are in good agreement with the results in Table III-4.

The structure of jaffeite also contains minor elements such as magnesium, iron, aluminium and sulphur the source of which is cement. The chemical formulae as revealed from EPMA at both temperatures are:

$(Mg_{0.04}Fe_{0.06}Ca_{5.79})_{\Sigma=5.89}(Si_{2.05}Al_{0.13}S_{0.03})_{\Sigma=2.21}O_{13.21}H_{5.81}$ **200 ℃**

$(Mg_{0.04}Fe_{0.05}Ca_{5.71})_{\Sigma=5.80}(Si_{1.83}Al_{0.13}S_{0.03})_{\Sigma=1.99}O_{12.91}H_{6.27}$ **250 ℃**

Previous studies on synthetic jaffeite have reported that magnesium can substitute calcium in the structure [27]. In addition the minor elements in the structure have the same values at both temperatures suggesting that temperature does not influence substitution in the jaffeite structure.

Table III-4: EPMA results of jaffeite crystals found in samples containing cement only and cured at two different temperatures 200 and 250 ℃. In addition electron probe results from natural jaffeite samples found in Kombat mine, Nambia [22] are also presented.

Temperature	**200 ℃**	**250 ℃**	**Jaffeite results after Sarp *et al.* [26]**
	Weight percent of oxides		
CaO	63.91	63.33	64.29
MgO	0.35	0.31	-
SiO_2	23.90	22.24	24.30
Al_2O_3	1.25	1.73	-
Fe_2O_3	0.89	0.72	-
SO_3	0.52	0.46	-
H_2O	9.18	11.21	11.41
	Formula based on 13 oxygens		
Ca	5.79	5.71	5.86
Mg	0.04	0.04	-
Si	2.05	1.83	2.02
Al	0.13	0.17	-
Fe^{3+}	0.06	0.05	-
S	0.03	0.03	-
H	5.81	6.27	6.21
Ca/Si	2.82	3.12	2.90

It has been reported that jaffeite can be produced via hydrothermal treatment of alite [Ca_3SiO_5] [28,29]. Many workers that analysed alite using X-ray microanalysis in cement clinkers [15,30-32], and the results from the modified Bogue calculations (Appendix) conclude that alite structure is never pure. The significant substitutions in clinker alites are Na^+, K^+, Mg^{2+} and Fe^{3+} for Ca^{2+} and Al^{3+},

P^{5+} and S^{6+} for Si^{4+}. It is therefore logical that some of the substituted oxides that were present in alite should also be present in jaffeite structure.

The chemical formulae above confirm that apart from sodium, potassium and phosphorus the rest of the elements are present in jaffeite. Comparing the results for the oxide composition of alites in different clinkers that Hall *et al.* [15] published, with that in jaffeite structure some similarities and some differences are observed. The amount of Al_2O_3 and MgO are found to be in good agreement with Hall *et al.* [15] and with the modified Bogue calculations. However the amount of iron and sulphur are different. The amount of iron in jaffeite structure is less compared to the alite whereas the amount of sulphur in jaffeite is double. The explanation for these differences has not been found yet.

According to X-ray diffraction the major phases in sample containing cement only at 200 ℃ are jaffeite and alpha dicalcium sil icate hydrate (Chapter II). An approximate estimate of the amount of aluminium, iron, magnesium, sulphur and potassium that these two phases derive from Dyckerhoff cement (see Chapter II, Table II-1) can be calculated. The weight percent of jafffeite and alpha dicalcium silicate hydrate is known from the Rietveld refinement in each sample (Chapter II, Table II-4). In addition the total mass of the reagents used is also known therefore from the law of mass/matter conservation and the EPMA chemical formulae (Table III-2 and Table III-4) the mass of aluminium, iron, magnesium, sulphur and potassium these two phases contain can be estimated and compared with that of the whole sample.

Figure III-7 shows that more than 70 % of the alumina present in cement is incorporated in jaffeite and approx 10 % in the α-$Ca_2SiO_4 \bullet (H_2O)$ structure. In addition more than 50 % of iron is distributed between these two phases. As alpha dicalcium silicate hydrate does not contain a lot of magnesium and sulphur in the chemical formula most of these elements are incorporated in jaffeite (45 % of magnesium and 35 % of sulphur). Finally more than 50 % of potassium contained in cement is incorporated in the α-$Ca_2SiO_4 \bullet (H_2O)$ structure whereas jaffeite does not contain any potassium. The remainder of these elements is probably distributed among the other phases present in this sample.

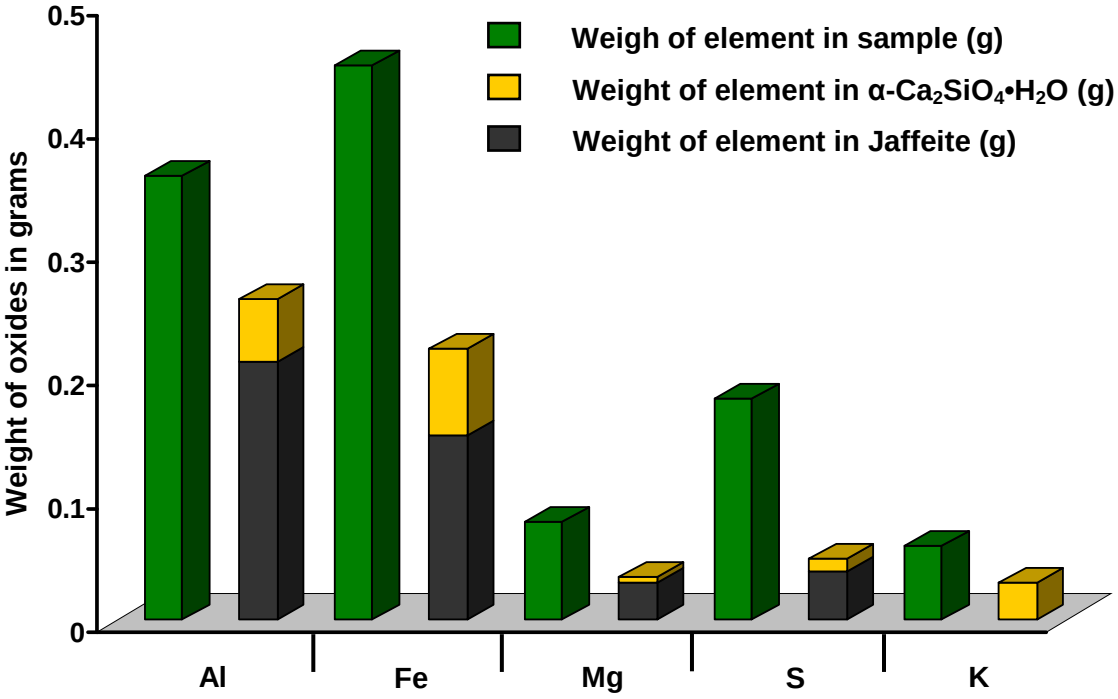

Figure III-7: Plot comparing the weight of the oxides Al_2O_3, Fe_2O_3. MgO, SO_3 and K_2O in the whole sample and in jaffeite and alpha dicalcium silicate hydrate structure.

It has been reported that the mineral jaffeite is transparent and colourless, the crystal system is hexagonal and that it occurs as euhedral to subhedral elongated crystals with a hexagonal cross section [26]. The SEM micrographs in Figure III-8 and Figure III-10 present needle shaped jaffeite crystals found in samples containing cement only and cured at 200 and 250 ℃ respectively. The micrographs in Figure III-9 and Figure III-11 are of higher magnification clearly presenting jaffeite crystals with hexagonal ends. According to these images the thickness of jaffeite crystals grown in cement, over 5 days, is approximately 200 nm.

The jaffeite crystal has been simulated using WinXmorph and as input parameters values from the International Crystal Structure Database (ICSD) have been used [26,27]. Figure III-12 shows a simulated hexagonal needle shaped crystal, which is identical with the real jaffeite crystals found in hydroceramic samples, shown in previous micrographs. In order to simulate this crystal, the values shown in Table III-5 have been used. These values represent the distances of the major faces from the centre of the crystal. The longer the distance the faster the face grows. The jaffeite crystal, according to WinXmorph, is elongated parallel to the

0 0 1 face along the *c* axis. This face is growing faster than the others (as it has a higher value than the others therefore the longer distance from the centre of the crystal) giving the needle shape to the crystal.

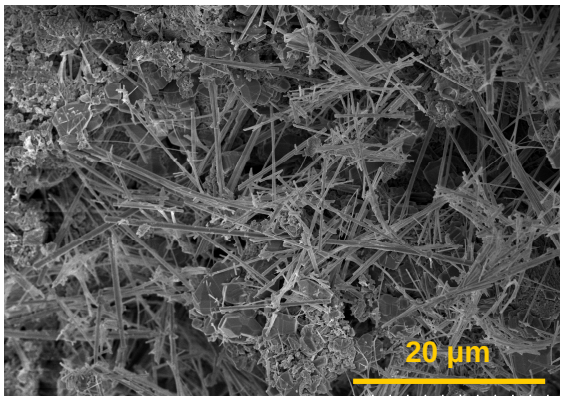

Figure III-8: SEM micrograph of jaffeite crystals in neat cement sample cured at 200 ℃

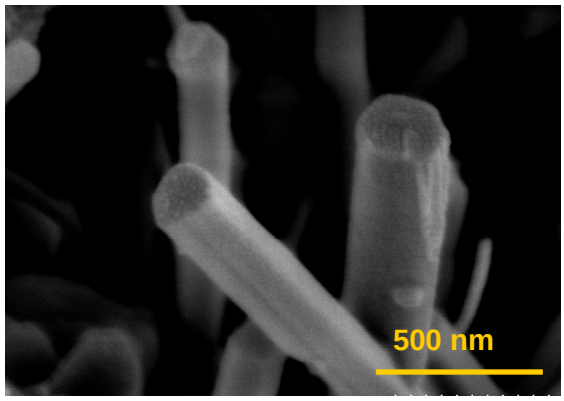

Figure III-9: Jaffeite crystals in neat cement cured at 200 ℃.

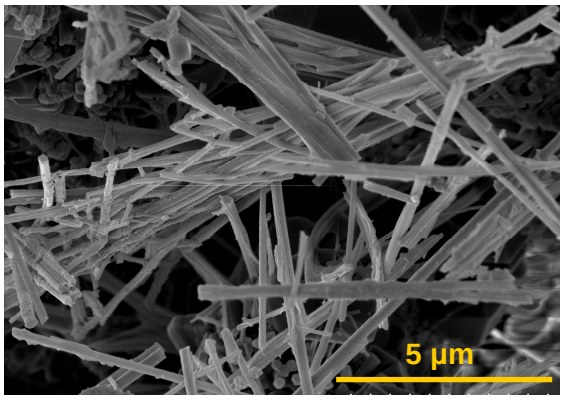

Figure III-10: SEM micrograph of jaffeite crystals in neat cement sample cured at 250 ℃

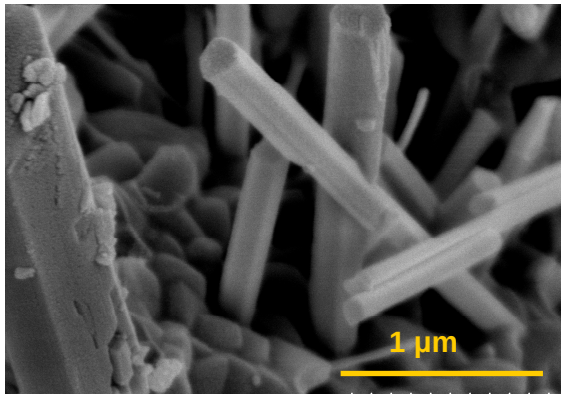

Figure III-11: Jaffeite crystals in neat cement cured at 250 ℃.

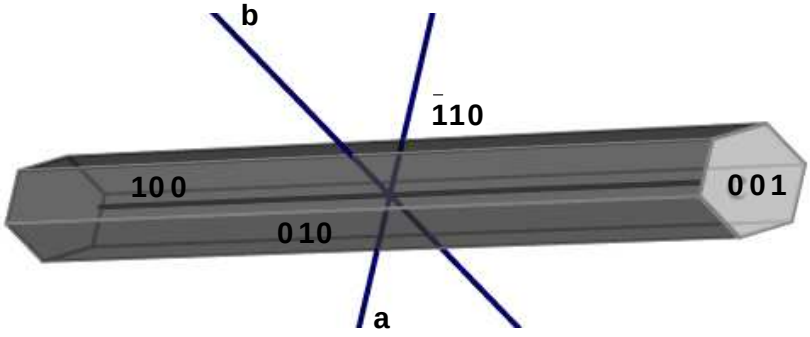

Figure III-12: Jaffeite crystal along with the faces growing as simulated using WinXmorph.

Table III-5: Distances of faces from the centre of the crystal.

Indices	Distance
1 0 0	1
0 1 0	1
0 0 1	20

III- 3.3 Reinhardbraunsite $Ca_5(SiO_4)_2(OH)_2$

Reinhardbraunsite forms in the CASH hydroceramic system at temperatures between 250 and 350 ℃ in neat cement samples and also in samples containing less than 20 wt % of silica flour (Chapter II). Using EPMA the chemistry of this mineral is examined in the sample containing 10 wt % of silica flour and cured at 300 ℃. Figure III-13 is a backscattered image taken from EPMA which shows a reinhardbraunsite grain and the different points that have been analysed. The results in Table III-6 are an average of these analyses. The formula is based on 10 oxygens and the weight percent of water is calculated as the difference from 100 % of the total. A typical error between these measurements is less than 7 %.

According to Table III-6 the chemical formula of reinhardbraunsite is:

$$(Mg_{0.01}Ca_{4.91})_{\Sigma=4.91}(Si_{1.99}Al_{0.03})_{\Sigma=2.02}\ O_{9.95}\ H_2$$

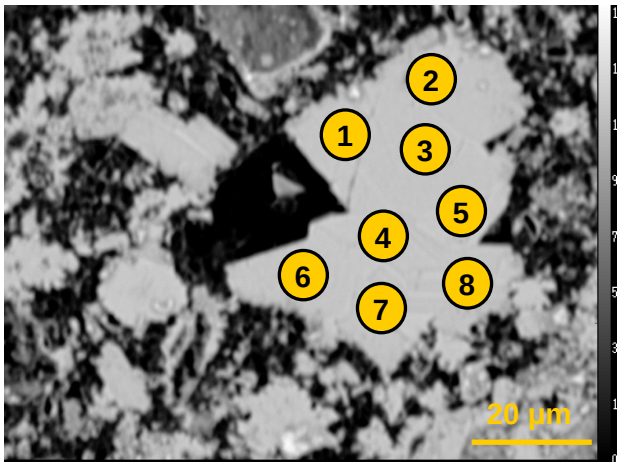

Figure III-13: Backscattered image of an EPMA analysis on a reinhardbraunsite grain. Sample contains 10wt % silica flour and cured at 300 ℃.

Table III-6: EPMA results of a reinhardbraunsite grain.

Weight percent of oxides	
CaO	66.18
SiO_2	28.68
Al_2O_3	0.53
MgO	0.26
H_2O	4.35
Formula based on 10 oxygens	
Ca	4.91
Si	1.99
Al	0.03
Mg	0.01
H	2.00
Ca/Si	2.47

The weight percent of the major oxides CaO and SiO_2 as well as the CaO/SiO_2 ratio are in very good agreement with that of the pure phase (66.98 % CaO, 28.7 % SiO_2 and 4.3 % H_2O). Minor amounts of other elements are also present in the structure such as magnesium and aluminium. The magnesium can substitute calcium as reinhardbraunsite, first known as calcio-chondrodite, is a natural equivalent of the mineral chondrodite $(Mg_5(SiO_4)_2(F,OH)_2$ [33]. Other reports mention that a trace of aluminium can exist in the reinhardbraunsite structure [34].

The crystal symmetry of reinhardbraunsite is monoclinic [34]. The secondary electron SEM image in Figure III-14 shows needle shaped reinhardbraunsite crystals where the length is approximately 500-600 nm and the thickness 100-200 nm.

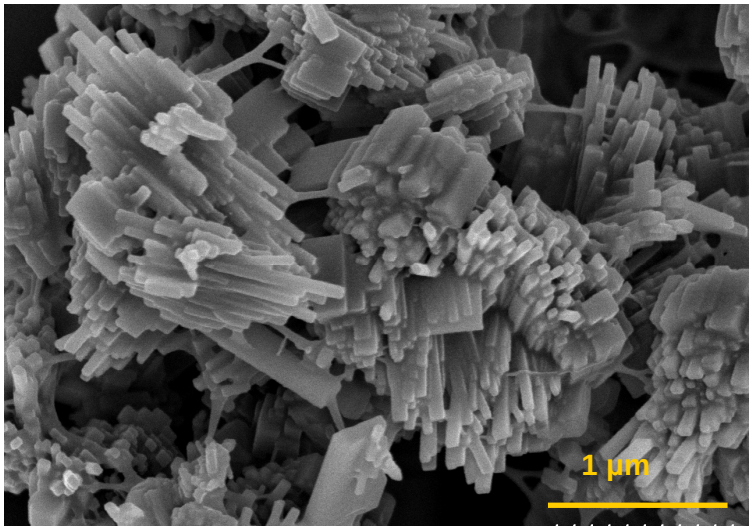

Figure III-14: SEM image of reinhardbraunsite crystals

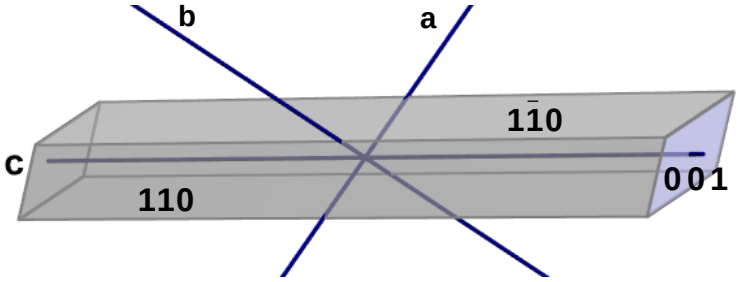

Figure III-15: Simulated reinhardbraunsite crystal using WinXmorph.

Table III-7: Distances of faces from the centre of the crystal.

Indices	Distance
0 0 1	20
1 1 0	1

Using WinxXmorph with input parameters from the International Crystal Structure Database (ICSD) [33,34] the reinhardbraunsite crystal has been simulated. In addition Table III-7 represents the distances of the major phases used to simulate that crystal. Figure III-15 shows a needle shaped crystal which is identical with the reinhardbraunsite crystals in hydroceramic samples. These crystals are elongated parallel to *0 0 1* face, as it is the face which grows faster (longer distance from the centre of the crystal), along the *c* axis.

III- 4. Conclusions

In this chapter the chemistry and the crystal shape of some major minerals that grow in the CASH hydroceramic system have been discussed. Using electron probe microanalysis the chemistry of belite, alpha dicalcium silicate hydrate, jaffeite and reinhardbraunsite have been studied. The EPMA results are found to be in very good agreement with measurements that have been carried out on either natural minerals or the synthetic equivalent. All these minerals incorporate in their structure some of the minor elements found in Dyckerhoff cement, such as aluminium, iron, magnesium, sulphur and potassium. In addition the temperature does not affect the amount of minor elements incorporated in the structure of jaffeite and alpha dicalcium silicate hydrate.

In neat cement sample cured at 200 ℃ it is found that most of the minor elements are incorporated in the two major phases which are jaffeite and alpha dicalcium silicate hydrate. Moreover in neat cement samples cured at 200 and 250 ℃ grains illustrating the progression of belite hydration have been found. The inner part of these grains consisted of belite partially hydrated whereas the outer part of alpha dicalcium silicate hydrate. In addition the hydration reaction of belite is shown here that possibly follow the rules encountered in mineral replacement processes.

Finally using WinXmorph jaffeite and reinhardbraunsite crystal have been simulated successfully. The shape of the simulated crystals was found to be identical with that of the real crystals found in hydroceramic samples. These minerals form needle shaped crystals, and according to WinXmorph are elongated parallel to *0 0 1* face, along the *c* axis.

III- 5. References

1. S. J. B. Reed,"*Electron probe microanalysis*" Cambridge, Cambridge University Press, 1996.

2. J. I. Goldstein, D. E. Newbury, P. Echlin, D. C. Joy, A. D. Romig, C. E. Lyman, C. Fiori, and E. Lifshin,"*Scanning electron microscopy and X-ray microanalysis. A text for biologists, materials scientists and geologists.*" New York and London, Plenum Press, 1992.

3. http://www.cameca.fr/html/epma_technique.html,

4. J. L. Pouchou and F. Pichoir, "Basic expression of 'PAP' computation for quantitative EPMA"; pp.249-253 in *Proceedings of the 11th ICXOM*. Edited by J. D. Brown and R. H. Packwood. University of Western Ontario, Ontario, 1987.

5. S. J. B. Reed and A. Buckley, "Virtual WDS," *Mikrochimica Acta,* **13** 479-483 (1996).

6. http://www.hitachi-hitec-uk.com/,

7. Kaminsky W., "WinXMorph: a computer program to draw crystal morphology, growth sectors and cross sections with export files in VRML V2.0 utf8-virtual reality format," *Journal of Applied Crystallography,* **38** [3] 566-567 (2005).

8. Kaminsky W., "From CIF to virtual morphology using the WinXMorph program," *Journal of Applied Crystallography,* **30** [2] 382-385 (2007).

9. Hiremath R., Basile J. A., Varney W. S., and Swift A. J., "Controlling molecular crystal polymorphism with self-assembled monolayer templates," *Journal of the American Chemical Society,* **27** [51] 18321-18327 (2005).

10. H. F. W. Taylor,"*Cement Chemistry*" 2nd. London, Thomas Telford Publishing, 1997.

11. G. W. Groves, "Twinning in beta-dicalcium silicate," *Cement and Concrete Research,* **12** [5] 619-624 (1982).

12. Y. J. Kim, I. Nettleship, and W. M. Kriven, "Phase-transformations in dicalcium silicate .2. TEM studies of crystallography, microstructure, and mechanisms," *Journal of the American Ceramic Society,* **75** [9] 2407-2419 (1992).

13. I. G. Richardson and G. W. Groves, "Microstructure and microanalysis of hardened ordinary Portland cement pastes," *Journal of Materials Science,* **28** [1] 265-277 (1993).

14. I. G. Richardson and G. W. Groves, "Microstructure and microanalysis of hardened cement pastes involving ground granulated blast-furnace slag," *Journal of Materials Science,* **27** [22] 6204-6212 (1992).

15. C. Hall and K. L. Scrivener, "Oilwell cement clinkers-X-ray microanalysis and phase composition," *Advanced Cement Based Materials,* **7** 28-38 (1998).

16. P. Barnes, C. H. Fentiman, and J. W. Jeffery, "Structurally related dicalcium silicate phases," *Acta Crystallographica,* **A36** 353-356 (1980).

17. K. Fukuda, I. Maki, and S. Ito, "Anisotropic thermal expansion of beta-Ca_2SiO_4 monoclinic crystal," *Journal of the American Ceramic Society,* **80** [6] 1595-1598 (1997).

18. J. Skibsted, H. J. Jakobsen, and C. Hall, "Direct observation of aluminum guest ions in the silicate phases of cement minerals by Al-27 MAS NMR spectroscopy," *Journal of the Chemical Society Faraday Transactions,* **90** [14] 2095-2098 (1994).

19. C. D. Lawrence, "The constitution and specification of portland cement", pp. 131-188 in *Lea's chemistry of cement & concrete***.** Edited by P. C. Hewlett. Butterworth-Heineman, Oxford, 1998.

20. L. Bonafous, C. Bessada, D. Massiot, J. P. Coutures, B. Lerolland, and P. Colombet, "Si-29 MAS NMR study of dicalcium silicate- The structural influence of sulfate and alumina stabilizers.," *Journal of the American Ceramic Society,* **78** [10] 2603-2608 (1995).

21. M. Kristmann, "Portland cement clinker, mineralogical and chemical investigations: Part II Electron microprobe analysis," *Cement and Concrete Research,* **8** 93-102 (1978).

22. A. Putnis, "Mineral replacement reactions: from macroscopic observations to microscopic mechanisms," *Mineralogical Magazine,* **66** [5] 689-708 (2002).

23. A. Putnis and C. V. Putnis, "The mechanism of reequilibration of solids in the presence of a fluid phase," *Journal of Solid State Chemistry,* **180** [5] 1783-1786 (2007).

24. C. H. Chan, W. M. Kriven, and J. F. Young, "Analytical electron microscopic studies of doped dicalcium silicates," *Journal of the American Ceramic Society,* **71** [9] 713-719 (1988).

25. N. Meller, K. Kyritsis, and C. Hall, "The mineralogy of the $CaO-Al_2O_3-SiO_2-H_2O$ (CASH) system from 200 to 350 ℃," *Cement and Concrete Research,* (submitted).

26. H. Sarp and D. R. Peacor, "Jaffeite, a new hydrated calcium silicate from the Kombat Mine, Namibia," *American Mineralogist,* **74** 1203-1206 (1989).

27. N. A. Yamnova, K. H. Sarp, Y. K. Egorov-Tismenko, Y. D. Pushcharovski, and G. Dasgupta, "Crystal structure of jaffeite," *Crystallography Reports,* **38** [4] 464-467 (1993).

28. P. Barnes, S. L. Colston, A. C. Jupe, S. D. M. Jacques, M. Attfield, R. Pisula, S. Morgan, C. Hall, P. Livesey, and S. Lunt, "The use of synchrotron sources in the study of cement materials", pp. 477-498 in *Structure and Performance of Cements***.** Edited by J. Bensted and P. Barnes. Spon Press, London & New York, 2002.

29. K. Garbev, L. Black, G. Beuchle, and P. Stemmermann, "Inorganic Polymers in Cement Based Materials," *Wasser und Geotechnologie,* **2** 19-30 (2002).

30. M. Kristmann, "Portland-cement clinker mineralogical and chemical investigations .2. Electron-microprobe analysis," *Cement and Concrete Research,* **8** [1] 93-102 (1978).

31. K. Fukuda, I. Maki, and K. Adachi, "Structure change of Ca_2SiO_4 solid-solutions with Ba concentration," *Journal of the American Ceramic Society,* **75** [4] 884-888 (1992).

32. A. M. Harrisson, H. F. W. Taylor, and N. B. Winter, "Electron-optical analyses of the phases in a portland-cement clinker, with some observations on the calculation of quantitative phase-composition," *Cement and Concrete Research,* **15** [5] 775-780 (1985).

33. A. Kirfel, H. M. Hamm, and G. Will, "The crystal structure of reinhardbraunsite, $Ca_5(SiO_4)_2(OH,F)_2$, a new mineral of the calcio-chondrodite type.," *Tschermaks Mineralogische und Petrographische Mitteilungen,* **31** [1-2] 137-150 (1983).

34. H. M. Hamm and G. Hentschel, "Reinhardbraunsite, $Ca_5(SiO_4)_2(OH,F)_2$, a new mineral. The natural equivalent of synthetic calcio-chondrodite.," *Neus Jahrbuch fur mineralogie-Monatshefte,* **3** 119-129 (1983).

CHAPTER IV

CALCIUM SILICATE HYDRATE MINERALS WITH LOW CaO/SiO_2 MOLE RATIO

IV- 1. Introduction

Calcium silicate hydrate minerals with increased silica in their structure start to form in the $CaO\text{-}SiO_2\text{-}Al_2O_3\text{-}H_2O$ (CASH) hydroceramic system when more than 20 wt % of silica flour is added at temperatures between 200 ℃ to 350 ℃ (Chapter II). When the CaO/SiO_2 mole ratio is equal or less than 1 the major minerals are xonotlite $Ca_6Si_6O_{17}(OH)_2$, 11Å tobermorite $Ca_5Si_6O_{17}\bullet 5(H_2O)$, gyrolite $Ca_{16}Si_{24}O_{60}(OH)_8\bullet(14+x)H_2O$ $0 \leq x \leq 3$ and truscottite $Ca_{14}Si_{24}O_{62}\bullet(4+z)H_2O$, $0 \leq z \leq 6$.

Using electron probe microanalysis (EPMA) the chemistry of these minerals has been studied. In addition scanning electron microscopy (SEM) and WinXmorph have been applied to obtain information regarding the crystal morphology of minerals with low CaO/SiO_2 mole ratio. The experimental techniques are described in detail in Chapter III.

IV- 2. Results and discussion

IV- 2.1 Xonotlite ($Ca_6Si_6O_{17}(OH)_2$)

Xonotlite is one of the most stable phases in the $CaO\text{-}SiO_2\text{-}Al_2O_3\text{-}H_2O$ (CASH) hydroceramic system. It is formed once more than 20 wt % of silica flour is added between temperatures of 200 ℃ to 350 ℃ (Cha pter II). Using electron probe microanalysis five different samples containing xonotlite have been studied. In order to examine if temperature has an impact on xonotlite chemistry, three samples (from the total group of five that were examined) containing the same amount of silica flour (30 wt %) but cured at different temperatures (200 ℃, 250 ℃ and 300 ℃) have been studied. The amount of xonotlite in these samples is very high (<90%) according to Rietveld refinement of X-ray diffraction patterns, as discussed in Chapter II. In addition two other samples have been studied containing other minerals with low CaO/SiO_2 mole ratio such as gyrolite or truscottite which co-exist with xonotlite, in order to examine whether the presence of other minerals affects the chemistry of xonotlite. The analysis of xonotlite is based on 19 oxygens and the weight percent of water is calculated as the difference from 100 % of the total.

Table IV-1 shows the average analysis of at least 15 measurements that have been carried out on xonotlite grains found in samples containing the same

amount of silica flour but cured at different temperatures (200 ℃, 250 ℃ and 300 ℃). A typical error between these measurements is less than 8 %.

Table IV-1: Electron probe analysis of xonotlite found in samples containing 30 wt % of silica flour. The ideal formula and previous analysis on a natural sample is also presented.

Temperature	200 ℃	250 ℃	300 ℃	Ideal Formula	Previous analysis after H. de Bruiyn [10]
	Weight percent of oxides				
CaO	42.43	43.82	44.58	47.06	45.07
Na_2O	0.35	0.10	0.10	-	-
K_2O	0.36	0.27	0.28	-	-
MgO	0.17	0.12	0.35	-	0.02
SiO_2	43.53	44.32	45.20	50.41	47.66
Al_2O_3	1.95	1.97	1.85	-	-
Fe_2O_3	0.54	0.70	1.06	-	-
SO_3	0.94	0.31	0.73	-	0.25
H_2O	9.73	8.39	5.85	2.51	7.00
	Formula based on 19 oxygens				
Ca	5.06	5.04	5.54	6	5.48
Na	0.07	0.02	0.02	-	-
K	0.05	0.04	0.04	-	-
Mg	0.03	0.02	0.06	-	0.003
Si	4.96	5.02	5.24	6	5.41
Al	0.26	0.25	0.25	-	-
Fe^{3+}	0.04	0.06	0.1	-	0.02
S	0.04	0.03	0.06	-	-
H	6.56	5.95	4.46	2	5.30
Ca/Si	1.02	1.00	1.06	1	1.01
Al/Si	0.06	0.05	0.04	-	-
Al/Fe	6.50	4.16	2.50	-	-

The chemical formulae of xonotlite as revealed from EPMA at different temperatures are:

$(K_{0.05}Mg_{0.03}Na_{0.07}Ca_{5.06})_{\Sigma=5.21}(Si_{4.96}Al_{0.26}Fe_{0.04}S_{0.04})_{\Sigma=5.30}\ (OH)_2\ O_{16.92}\ H_{4.56}$ **200 ℃**

$(K_{0.04}Mg_{0.02}Na_{0.02}Ca_{5.04})_{\Sigma=5.12}(Si_{5.02}Al_{0.25}Fe_{0.06}S_{0.03})_{\Sigma=5.36}\ (OH)_2\ O_{16.66}\ H_{3.95}$ **250 ℃**

$(K_{0.04}Mg_{0.06}Na_{0.02}Ca_{5.54})_{\Sigma=5.66}(Si_{5.24}Al_{0.25}Fe_{0.10}S_{0.06})_{\Sigma=5.65}\ (OH)_2\ O_{17.04}\ H_{2.46}$ **300 ℃**

The first observation is that the water content in xonotlite formula is high and as temperature increases the amount of water decreases. Previous analysis of both

natural and synthetic xonotlites show higher water content than assumed by the formula ($Ca_6[Si_6O_{17}](OH)_2$) [1-3]; and there are two general formulae to calculate the water content. Grimmer *et al.* [2] suggests the formula $Ca_{6-x}(Si_6O_{17}H_{2x})(OH)_2(H_2O)_{x/2}$ where as Kalousek *et al.* [3] suggests $Ca_{6-x}(Si_6O_{17}H_{2x})(OH)_2$. However these formulae can not be applied in our case due to the presence of other elements in xonotlite structure.

The CaO/SiO_2 mole ratio is in good agreement with that of the pure phase however the weight percent of these oxides (CaO and SiO_2) have lower values compared to pure xonotlite (47.06 wt % CaO and 50.41 % SiO_2). Studies have shown that if xonotlite is deficient in Ca, in order to maintain the charge balance additional H atoms are incorporated in the structure as SiOH groups and as OH molecules [2,3]. In our case the values for both Ca and Si are lower than expected therefore possibly more water molecules are incorporated in the structure replacing these two elements in order to maintain the charge balance. This suggestion is based on the fact that as more calcium and silica is present in xonotlite, as the temperature increased, the water content is decreased. Of course there remains the possibility some of the water molecules are present in order to obtain charge balance due to other elements present in the structure (Al, Fe^{3+} etc.).

Additionally xonotlite is believed to form topotactically from tobermorite [3,4]. That is, a single crystal of tobermorite changes into something approaching a single crystal of xonotlite, in a definite crystallographic orientation. During such a process the numbers of Ca and Si atoms per unit volume possibly tend to remain constant [3]. Therefore it is possible the xonotlite formed in the hydroceramics is defective in Ca as tobermorite has less Ca in the structure than xonotlite. The Si deficiency can also be explained if the chemical formula of tobermorite is also defective in Si.

The EPMA shows that xonotlite accommodates approximately 1.9 wt % of Al_2O_3 in the structure at all the temperatures examined. The presence of this oxide is not rare as it has been reported that natural xonotlites can incorporate small amounts of Al_2O_3 (~1 wt %) [5] and synthetic xonotlites can substitute Al^{3+} for Si^{4+} up to 5 % [3,6,7]. Temperature does not seem to affect the amount of Al substituted in the structure. In contrast, comparing the Al_2O_3/Fe_2O_3 ratio of xonotlite with temperature a correlation is observed. As temperature increase the amount of iron present in the structure increases also. The only assumption that can be made is that the sample cured at 300 ℃ is pure xonotlite (Chapter II) where as at lower

temperatures (200 ℃) small amounts of tobermorite are present as well which might incorporate some iron in the structure.

Magnesium can partially substitute Ca up to 14 % in systems with high amounts of MgO [8,9]. In our case only small amounts of Mg are present in the structure < 0.4 wt %. Other minor elements such as potassium, sodium and sulphur, are present, which is not rare in natural occurring xonotlites [10].

According to X-ray diffraction results the only phase present in the sample containing 30 wt % of silica flour and cured at 300 ℃ is xonotlite (Chapter II). An approximate estimate of the amount of calcium, silica, aluminum, iron, magnesium, sulphur, potassium and sodium that this phase absorbs from Dyckerhoff cement (Table II-1) can be calculated. The weight percent of xonotlite is known in this sample from the Rietveld refinement (Chapter II see Table II-4). In addition the total mass of the reagents used is also known therefore from the law of mass/matter conservation and the EPMA chemical formulae (Table IV-1) the mass of calcium, silica, aluminum, iron, magnesium, sulphur, potassium and sodium that xonotlite contains can be estimated and compare it with that of the whole sample.

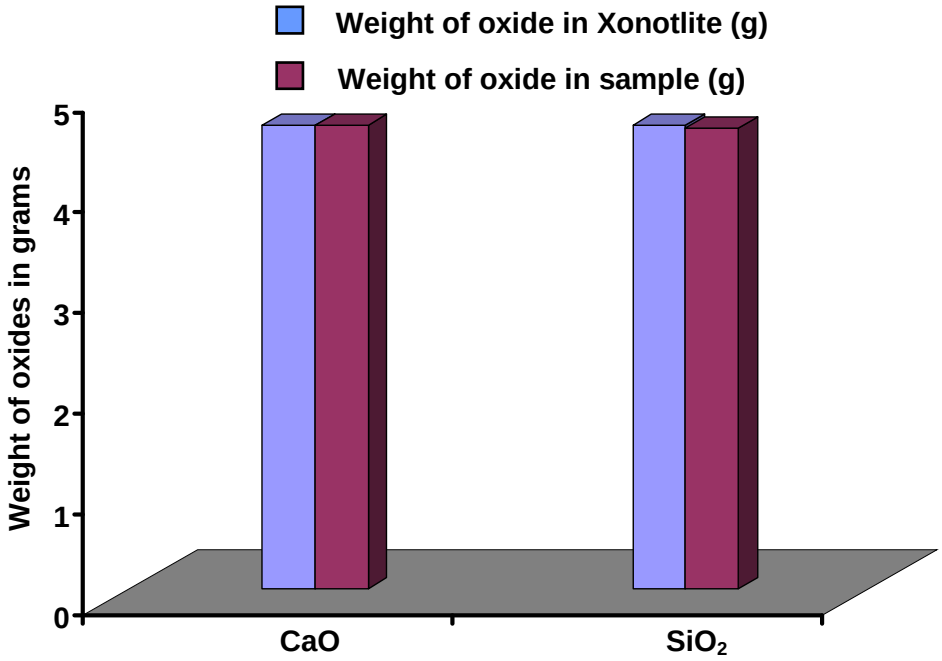

Figure IV-1: Plot comparing the weight of CaO and SiO_2 in sample cured at 300 ℃ containing 30 wt% of silica flour and in xonotlite.

The amount of calcium and silica according to Figure IV-1 is the same in the xonotlite structure and the whole sample. This suggests that the system has reached equilibrium as the amount of the two major oxides have been consumed and reacted to form xonotlite. In addition Figure IV-2 shows that all the aluminum, sodium and potassium present in Dyckerhoff cement enters the xonotlite structure. More than 90 % of the iron from the ferrite phases of cement is present in xonotlite, and 95 % of magnesium and 70 % of sulphur enters the xonotlite structure. In some cases the amount of the oxide that xonotlite contains is slightly higher than the amount of the whole sample (e.g. Na_2O). This is due to overestimation of the particular element from the electron probe.

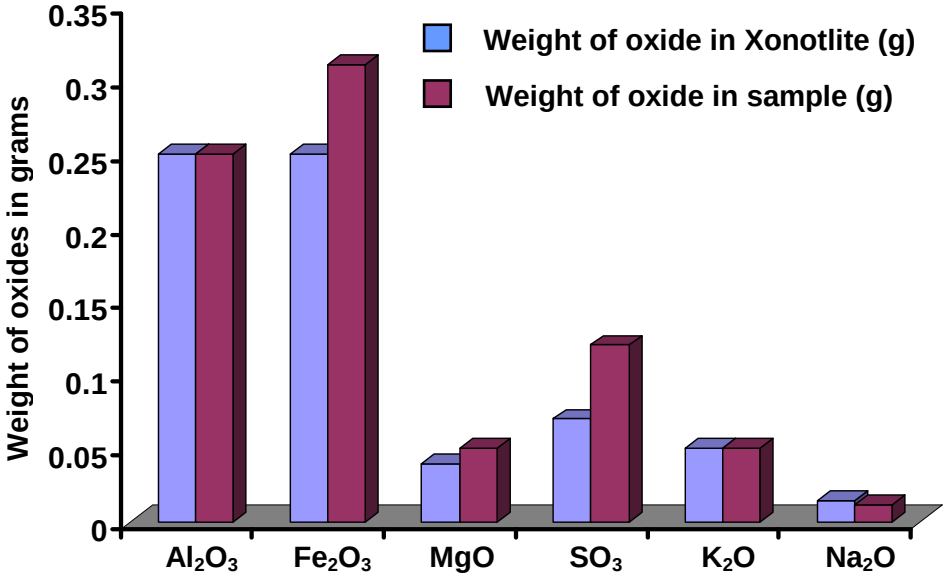

Figure IV-2: Plot comparing the weight of Al_2O_3, Fe_2O_3, MgO, SO_3, K_2O and Na_2O in the sample cured at 300 ℃ containing 30 wt% of silica flour compared with xonotlite in the same sample.

EPMA measurements have been carried out on samples containing 40 wt % of silica flour and cured at 200 ℃ and 300 ℃. The results shown in Table IV-2 are an average of xonotlite measurements found in these samples. The chemical formulae of xonotlites in these samples are:

$$Ca_{5.32}(Si_{5.12}Al_{0.18}Fe_{0.01}S_{0.11})_{\Sigma=5.42}\ (OH)_2\ O_{17.18}\ H_{4.02}$$ **200 ℃**

$(Mg_{0.03}Ca_{5.29})_{\Sigma=5.32}(Si_{5.07}Al_{0.19}Fe_{0.09}S_{0.05})_{\Sigma=5.4}\ (OH)_2\ O_{16.95}\ H_{3.85}$ **300 ℃**

Table IV-2: EPMA measurements on xonotlite in samples containing 40 wt % of silica flour and cured at 200 ℃ and 300 ℃. The ideal formula o f xonotlite is also presented.

Temperature	200 ℃	300 ℃	Ideal formula
	Weight percent of oxides		
CaO	44.10	43.65	47.06
Na_2O	n.d.	n.d.	-
K_2O	n.d.	n.d.	-
MgO	n.d.	0.18	-
SiO_2	45.46	44.84	50.41
Al_2O_3	1.38	1.41	-
Fe_2O_3	0.10	1.15	-
SO_3	1.31	0.62	-
H_2O	7.77	8.97	2.51
	Formula based on 19 oxygens		
Ca	5.32	5.29	6
Na	n.d.	n.d.	-
K	n.d.	n.d.	-
Mg	n.d.	0.03	-
Si	5.12	5.07	6
Al	0.18	0.19	-
Fe^{3+}	0.01	0.09	-
S	0.11	0.05	-
H	6.02	5.85	2
Ca/Si	1.03	1.04	1

The Ca/Si is again in good agreement with that of the pure phase but still the amount of these elements is in low concentration compared to pure xonotlite. The amount of alumina is the same in both samples. Comparing the two xonotlite formulae in samples cured at 200 ℃ Na, K, and Mg a re not present in the structure of xonotlite in sample containing 40 wt % of silica flour, and the amount of iron is also lower. The presence of gyrolite in this sample probably affects the xonotlite chemistry. A similar effect is observed in the presence of truscottite in the sample containing 40 wt % of silica flour and cured at 300 ℃. The xonotlite structure in this case does not contain Na and K.

Xonotlite forms needle shape crystals. Figures IV-2 to IV-6 show samples at different magnifications containing xonotlite crystals. All the samples have the same amount of silica flour (30 wt %) but are cured at different temperatures (200 ℃–

300℃). According to the micrographs the thickness of a xonotlite needle is approximately 100 nm.

Xonotlite has a monoclinic crystal structure although different polytypes exist [6]. Using WinXmorph, xonotlite crystals have been simulated. The input parameters that have been used are from the International Crystal Structure Database (ICSD) [6,11]. Figure IV-7 presents the simulated xonotlite crystal which is identical with the crystals present in the micrographs. Table IV-3 shows the faces used to generate the crystal and the relative distance of those faces from the centre of the crystal. Xonotlite crystals are elongated parallel to the *b* axis where the *0 1 0* face is growing.

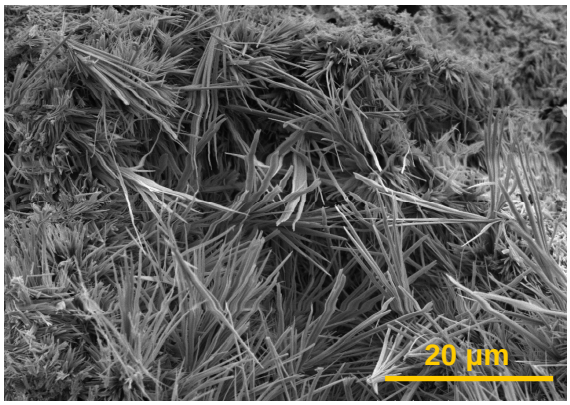

Figure IV-3: SEM micrograph of xonotlite needles in sample cured at 200 ℃, containing 30 wt% of silica flour.

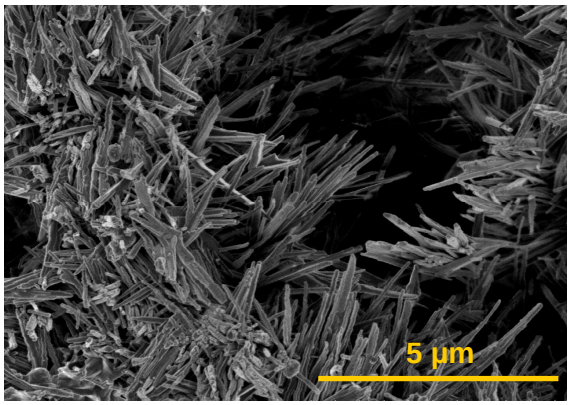

Figure IV-4: SEM micrograph of xonotlite needles in sample cured at 250 ℃, containing 30 wt% of silica flour.

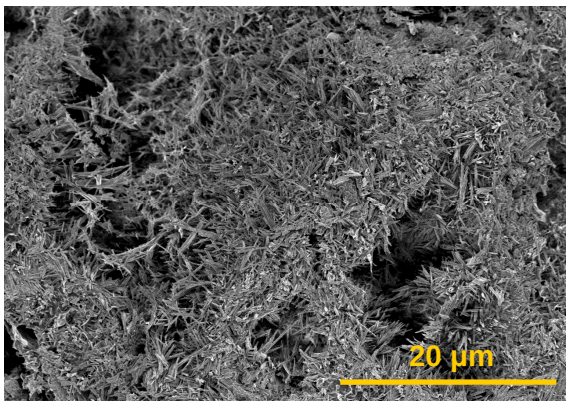

Figure IV-5: SEM micrograph of xonotlite needles in sample cured at 300 ℃, containing 30 wt% of silica flour.

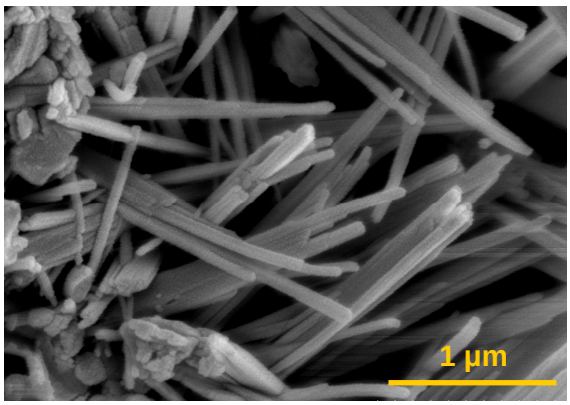

Figure IV-6: SEM micrograph of xonotlite needles in sample cured at 300 ℃, containing 30 wt% of silica flour.

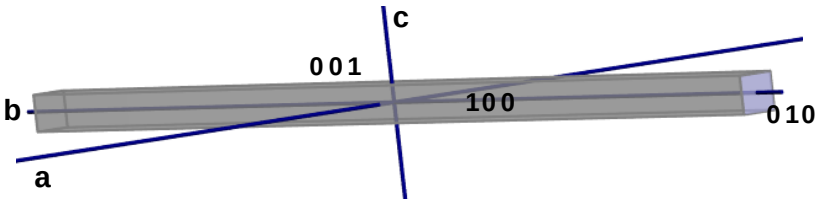

Figure IV-7: Xonotlite crystal along with the faces growing as simulated using WinXmorph.

Table IV-3: Distances of faces from the centre of the crystal.

Indices	Distance
1 0 0	1
0 1 0	30
0 0 1	1

IV- 2.2 11Å Tobermorite ($Ca_5Si_6O_{17}•5H_2O$)

The tobermorite group consists of three distinct members corresponding to three degrees of hydration. 14Å tobermorite or plombierite is the most hydrated member of this group with the chemical formula $Ca_5Si_6O_{16}(OH)_2•7H_2O$ [12]. Once this phase is heated up it loses some interlayer water and undergoes unidimensional lattice shrinkage resulting to tobermorite 11Å with a general chemical formula $Ca_{4+x}SiO_{15+2x}(OH)_{2-2x}•5(H_2O)$ [13]. At higher temperatures >300 ℃ tobermorite loses more water and the lattice shrinks further resulting in 9Å tobermorite or riversideite with the formula being $Ca_5Si_6O_{16}(OH)_2$ [14]. Some specimens of tobermorite 11Å do not shrink on dehydration and are called 'anomalous' to distinguish them from those specimens that shrink on dehydration ('normal' tobermorites) [15].

Tobermorite is mostly present in the $CaO\text{-}SiO_2\text{-}Al_2O_3\text{-}H_2O$ (CASH) hydroceramic system when more than 10 wt % of silica flour is added to the system at 200 ℃. It is also present when both silica and alumina are added at different proportions at 200 ℃ and 250 ℃ (see Chapter II). In order to examine the chemistry of this particular phase a sample containing 30 wt % of silica flour and cured at 200 ℃ has been studied using EPMA. The an alysis of tobermorite is based on 22 oxygens and the weight percent of water is calculated as the difference from 100 % of the total. A typical error between these measurements is less than 9.5 %.

In Table IV-4 the results from an average of 15 measurements of tobermorite are presented. The chemical formula of tobermorite as revealed from EPMA is:

$$(K_{0.1}Mg_{0.06}Na_{0.08}Ca_{5.14})_{\Sigma=5.37}(Si_{5.44}Al_{0.36}Fe_{0.14}S_{0.05})_{\Sigma=5.99}\ O_{21.87}\ H_{9.61}$$

The amount of water in the structure of this mineral suggests that in the hydroceramic system at 200 ℃ 11Å tobermorite is pr esent as confirmed from the X-ray diffraction (Chapter II). Whether it is the normal or the anomalous form is still unclear.

Table IV-4: EPMA results of tobermorite. Sample containing 30 wt % of silica flour and cured at 200 ℃. The ideal formula and previous analysis on natural sample is also presented.

Temperature	**200 ℃**	**Ideal Formula**	**Previous analysis after Mitsuda et. al [15]**
	Weight percent of oxides		
CaO	38.47	38.36	34.64
Na_2O	0.35	-	0.44
K_2O	0.53	-	0.12
MgO	0.31	-	0.02
SiO_2	43.76	49.31	45.24
Al_2O_3	2.41	-	3.81
Fe_2O_3	1.48	-	0.07
SO_3	0.50	-	-
H_2O	11.63	12.32	15.66
	Formula based on 22 oxygens		
Ca	5.14	5	4.36
Na	0.08	-	0.1
K	0.10	-	0.02
Mg	0.06	-	0.003
Si	5.44	6	5.31
Al	0.36	-	0.52
Fe^{3+}	0.14	-	0.006
S	0.05	-	-
H	9.61	10	12.27
Ca/(Al+Si)	0.88	-	0.74
Al/(Al+Si)	0.06	-	0.09

The Al^{3+} for Si^{4+} substitution in natural and synthetic 11Å tobermorites is very common and it is accompanied by a partial substitution of O^{2-} to OH^- to balance the charge [13]. The 11Å tobermorite has a wide range of Ca/(Al+Si) atomic ratio. The Ca/(Al+Si) atomic ratio of natural tobermorite is generally in the range of 0.71-1.14 [15]. Mitsuda *et al.* [16] showed that tobermorites in calcium silicate products have a mean Ca/(Al+Si) atomic ratio of 0.76-1.09. Our results showed that the atomic ratio of Ca/(Al+Si) is 0.88 a value which is in good agreement with that reported

previously. In addition the atomic ratio of Al/(Al+Si) value is in very good agreement with Sakiyama *et al.* [17] who indicated that the maximum substitution of Al/(Al+Si) in 11Å tobermorite is 0.13-0.14.

Mitsuda and Taylor [15] reported the following differences between the normal and anomalous types of 11Å tobermorite based on examination of published data for natural tobermorites. Normal tobermorite has a higher Ca/(Al+Si) atomic ratio as very low contents of Al^{3+} and little or no alkali (such as Na and K) are present in the structure where as anomalous type has a lower Ca/(Al+Si) ratio and relatively higher contents of Al and alkali. Based on these observations and the results from EPMA (Table IV-4) we believe that the anomalous type of 11Å tobermorite is present in the $CaO\text{-}SiO_2\text{-}Al_2O_3\text{-}H_2O$ (CASH) hydroceramic system.

Other elements are also present in the tobermorite structure, namely iron, sodium, potassium and magnesium. The isomorphous substitution between Fe^{+3} and Si^{4+} is not rare in tobemorite as it has been reported in the natural and synthetic type of this mineral [18,19]. It has also been reported that the substitution of Al^{3+} for Si^{4+} is greater than Fe^{3+} for Si^{4+} which is confirmed by these measurements. Substituted tobermorites with Fe^{3+} or Al^{3+} atoms for Si^{4+} usually incorporate in their structure univalent cations such as Na^+ and K^+ in order to maintain the charge neutrality. Usually tobermorites exhibit selectivity for the substitution of these elements in the order $Na^+ < K^+$ [20]. In the EPMA measurements this selectivity has been confirmed (Table IV-4). Finally the amount of Mg is low confirming the suggestion that tobermorite can not accommodate appreciable amounts of Mg [9,15,19].

The tobermorite study is found in the sample containing 30 wt % of silica flour and cured at 200 ℃. According to X-ray diffr action (Chapter II) this sample contains large amounts of xonotlite (90 %). Knowing the chemical formulae of tobermorite (Table IV-4) and xonotlite (Table IV-1) present in this sample as well as the percentage of each phase (Chapter II, Table II-4) we can estimate the amount of the elements absorbed from cement.

The amount of CaO and SiO_2 that the whole sample contains is equal to the amount of xonotlite and tobermorite (Figure IV-8). This suggests that the sample reached chemical equilibrium. The small increase in the SiO_2 that the two phases contain compare to the whole sample is probably due to overestimation of this oxide from EPMA. Also there is a possibility that one or both of these phases has been overestimated from the Rietveld refinement process.

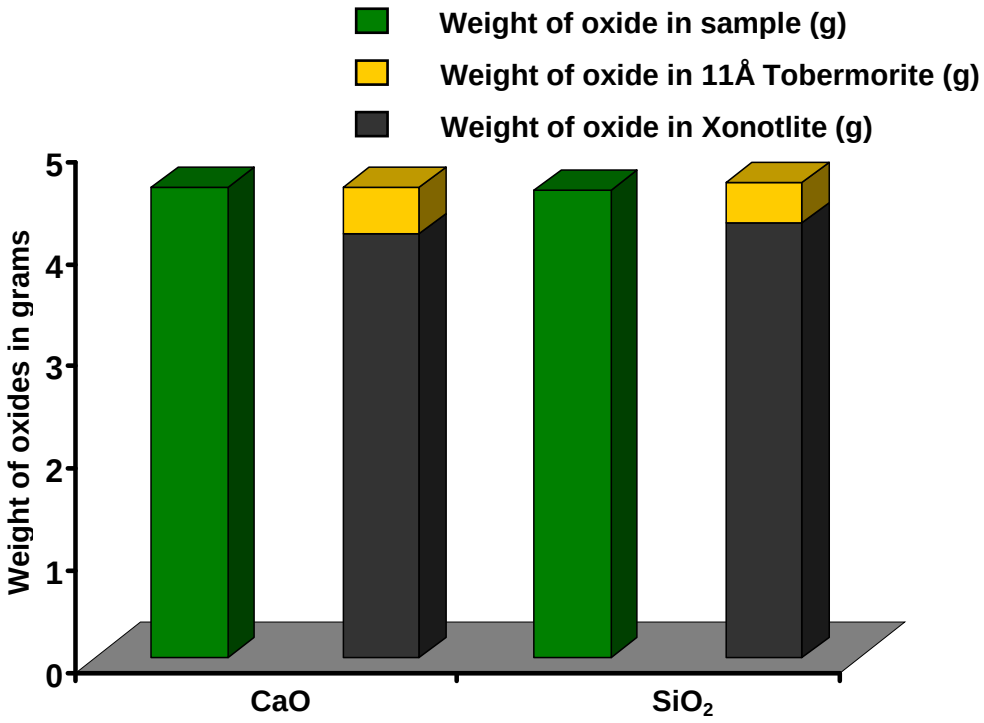

Figure IV-8: Plot comparing the weight of CaO and SiO_2 in sample cured at 200 ℃ containing 30 wt% of silica flour and in xonotli te and 11 Å tobermorite.

When both of these phases are present in a sample all the alumina contained in cement is distributed between the two (Figure IV-9). Also more than 60 % of the iron from the ferrite phase of cement is incorporated in the structures of xonotlite and tobermorite. Although the percentage of tobermorite in the sample is much lower than xonotlite, this phase contributes in the absorption of iron almost equally with xonotlite. In addition the amount of sodium and potassium is totally distributed between xonotlite and tobermorite. Finally more than 70 % of magnesium and 50 % of sulphur is present in the structure of these two minerals. It is unclear at present where the remainder of these oxides are located.

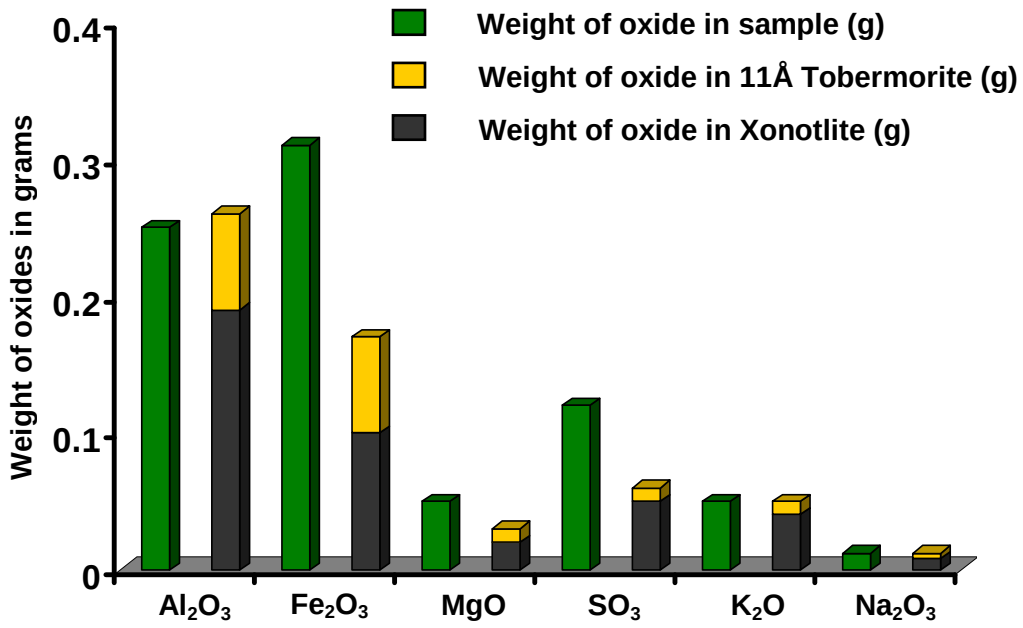

Figure IV-9: Plot comparing the weight of Al_2O_3, Fe_2O_3, MgO, SO_3, K_2O and Na_2O in sample cured at 200 ℃ containing 30 wt% of si lica flour and in xonotlite and 11Å tobermorite.

Polytypism in tobermorite is very common. The crystal system of 11Å tobermorite can be either monoclinic or orthorhombic [13]. It has been reported that this mineral forms either pseudohexagonal platy crystals or needle shaped aggregates [21,22]. In order to simulate the two types of crystals, data from the ICSD has been used [13,23]. The crystal system used in both cases was monoclinic.

In Figure IV-10 a thin pseudohexagonal platy crystal is shown as simulated using WinXmorph. This crystal is parallel to the *b* axis and has a *0 0 1* cleavage. In Table IV-5 are shown the distances of each face used to simulate the tobermorite crystal. These crystals are thin as the *0 0 1* face is not growing very fast and the pseudoxehagonal shape is due growth on the *1 1 0* face. Taylor [24] reported that the normal type of 11Å tobermorite is formed in this shape.

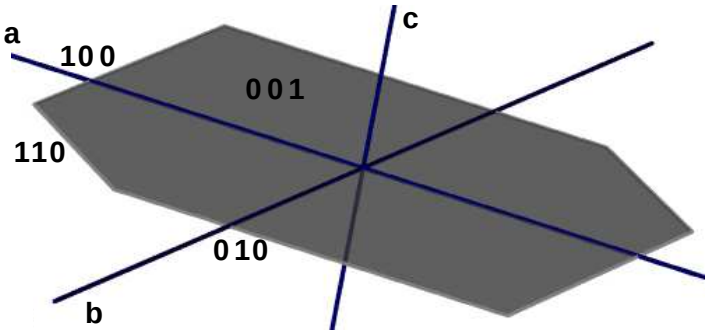

Figure IV-10: 11Å (normal) Tobermorite crystal with growth faces, as simulated using WinXmorph.

Table IV-5: Distances of faces from the centre of the crystal.

Indices	Distance
1 0 0	1
0 1 0	1
0 0 1	0.001
1 1 0	1

Figure IV-11 shows the fibrous form of tobermorite which is elongated parallel to the *b* axis. The fast growing face is the *0 1 0* and again the slow growing face is the *0 0 1* which is responsible for creating thin crystals (Table IV-6). It has been reported that the anomalous form of 11Å tobermorite has this shape [24].

In the specific sample examined 90 % consists of xonotlite which forms needle shaped crystals, and the rest is 11Å tobermorite. The SEM images show no evidence of a thin platy crystal. Therefore our belief from the chemistry of this mineral, that the anomalous type of 11Å tobermorite is present in the hydroceramic system, now is verified. However it was very difficult to distinguish between the needle shaped crystals as to which is tobermorite or which is xonotlite.

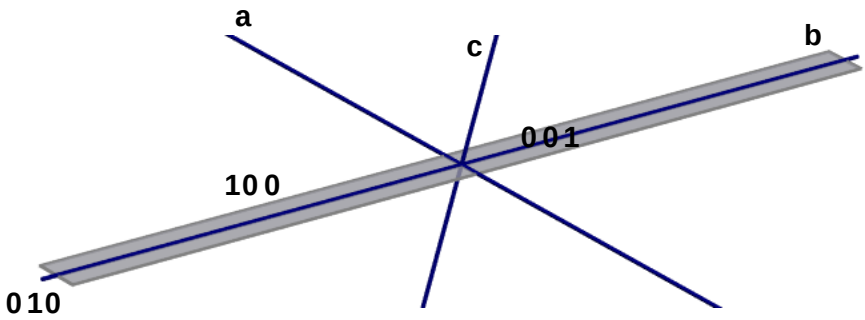

Figure IV-11: 11Å (anomalous) Tobermorite crystal with growth faces, as simulated using WinXmorph.

Table IV-6: Distances of faces from the centre of the crystal.

Indices	Distance
1 0 0	1
0 1 0	30
0 0 1	0.001

IV- 2.3 Gyrolite $Ca_{16}Si_{24}O_{60}(OH)_8•(14+n)H_2O$, $(0 \leq n \leq 3)$

Gyrolite is present in the CaO-SiO_2-Al_2O_3-H_2O (CASH) hydroceramic system when more than 40 wt % of silica flour is added at 200 ℃ and 250 ℃. The chemistry of this calcium silicate hydrate mineral has been studied using EPMA. The sample used contained 40 wt % of silica flour and was cured at 200 ℃. The analysis is based on 82 oxygens and the weight percent of water is calculated as the difference from 100 % of the total. A typical error between these measurements is less than 5 %.

In Table IV-7 the average of at least 20 gyrolite measurements is shown. The chemical formula of gyrolite as revealed from EPMA is:

$$(K_{0.1}Mg_{0.11}Na_{0.04}\,Fe_{0.24}Ca_{16.37})_{\Sigma=16.86}(Si_{22.15}Al_{1.15}S_{0.08})_{\Sigma=22.38}\,O_{60}\,(OH)_8•14.07H_2O$$

Table IV-7: EPMA results of gyrolite. Sample containing 40 wt % of silica flour and cured at 200 ℃. The ideal formula and previous analysis on a natural sample is also presented.

Temperature	200 ℃	Ideal formula	Previous analysis after Merlino [25]
	Weight percent of oxides		
CaO	33.87	33.01	28.54
Na_2O	0.05	-	0.67
K_2O	0.17	-	0.35
MgO	0.17	-	1.98
SiO_2	49.30	53.06	50.60
Al_2O_3	2.17	-	5.54
Fe_2O_3	0.70	-	0.41
SO_3	0.24	-	-
H_2O	13.33	13.92	12.69
	Formula based on 85 oxygens		
Ca	16.37	16	13.32
Na	0.04	-	0.57
K	0.10	-	0.19
Mg	0.11	-	0.28
Si	22.15	24	22.04
Al	1.15	-	2.84
Fe^{3+}	0.24	-	0.14
S	0.08	-	-
H	39.73	42	38.42
Ca/(Al+Si)	0.70	-	0.53
Al/(Al+Si)	0.95	-	0.11

According to the general formula of gyrolite the water content in the structure is variable ($Ca_{16}Si_{24}O_{60}(OH)_8 \bullet (14+n)H_2O$, $0 \leq n \leq 3$). The EPMA results show that the x value for the gyrolite formed in the hydroceramic system is 0.7.

The presence of aluminum, replacing silicon atoms, in the gyrolite structure is very common in natural and synthetic species [25,26]; however natural gyrolites (eg. in Cornwall, England) with no aluminum may rarely occur [27,28]. The EPMA measurements in Table IV-7 show that the atomic ratio of Ca/(Al+Si) and Al/(Al+Si) are in good agreement with that reported for natural and synthetic gyrolites, (Ca/(Al+Si) ranges from 0.54 to 0.74 and Al/(Al+Si) from 0.005 to 0.11) [25]. In addition the weight percent of the two major oxides CaO and SiO_2 are in good agreement with that of the pure phase (33.68 wt % CaO and 54.13 wt % SiO_2).

Minor/trace elements, such as iron, magnesium, sodium, potassium and sulphur, the source of which is the Dyckerhoff cement, are present in gyrolite structure. The amount of iron incorporated in the structure, substituting calcium, reflects the amount of iron in the system, however natural gyrolites may contain less than 6 wt % [25]. The replacement of Si^{4+} with Al^{3+} and Ca^{2+} with Fe^{3+} creates a charge imbalance. Therefore univalent cations such as Na^+ and K^+ are present in the structure of gyrolite to maintain charge neutrality. It has been reported that substituted gyrolites exhibit a selectivity for univalent cations in the order $Na^+ < K^+$ [29], which is confirmed from this EPMA measurements (Table IV-7). In addition the presence of magnesium and sulphur is not rare in natural and synthetic gyrolites [25].

In addition to gyrolite, the sample studied contains xonotlite and unreacted silica flour in the form of quartz (Chapter II). Figures IV-12 and IV-13 compare the amount of the oxides in the whole sample with that contained in gyrolite and xonotlite structures. Figure IV-12 shows that the sample has reached equilibrium as all the calcium has entered into xonotlite and gyrolite. Most of the silicon is distributed between these two phases and the remainder is quartz as there is insufficient calcium to produce further gyrolite or xonotlite. Almost all the magnesium, potassium and sodium are incorporated in the gyrolite structure alone. In addition 70 % of the total aluminum, is present in gyrolite and the remainder (30 %) resides in xonotlite. The small increase of aluminum that both phases contain compare to the whole sample is probably due to an overestimation of this oxide from EPMA in one or both of the phases or an overestimation of these phases from the Rietveled refinement process (Chapter II). The amount of iron contained in xonotlite

and gyrolite is small compared to the whole sample. Most of the iron is present in gyrolite. In contrast more than 60 % of the sulphur is incorporated in the xonotlite structure and 20 % in gyrolite.

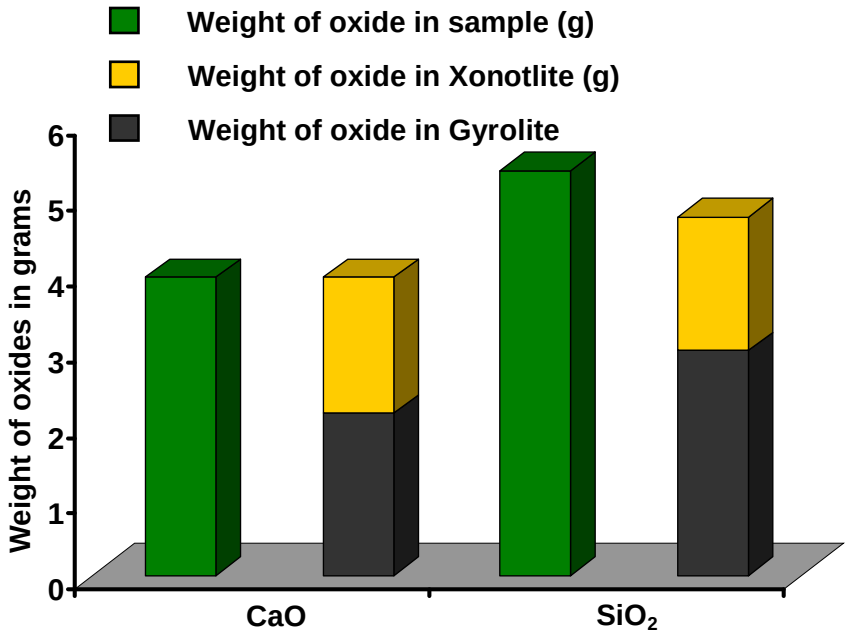

Figure IV-12: Plot comparing the weight of CaO and SiO_2 in sample cured at 200 ℃ containing 4 0 wt% of silica flour and in xonotlite and

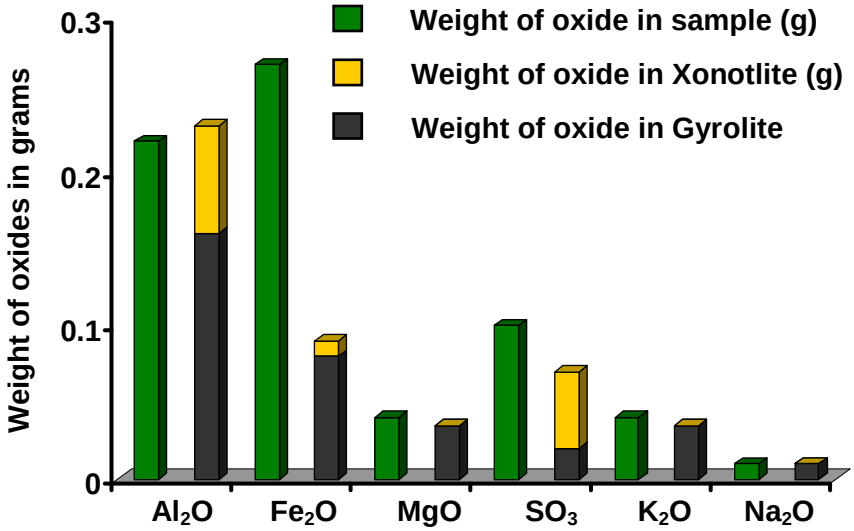

Figure IV-13: Plot comparing the weight of Al_2O_3, Fe_2O_3, MgO, SO_3, K_2O and Na_2O in sample cured at 200 ℃ containing 40 wt% of silica flour and in xonotlite and gyrolite.

Natural and synthetic gyrolites form crystals which have a thin, platy, pseudohexagonal shape [26,30]. In the $CaO\text{-}SiO_2\text{-}Al_2O_3\text{-}H_2O$ (CASH) hydroceramic system gyrolite crystals have such a shape, however the edges of the crystals are more rounded as shown in Figures IV-14 to IV-17. The needle shaped crystals shown in Figure IV-15 are of xonotlite. The samples in these figures, cured at two different temperatures 200 ℃ and 250 ℃, contain t he same amount of silica flour (40 wt %).

Gyrolite belongs to the triclinic system. Using WinXmorph and data from the International Crystal Structure Database (ICSD) [25] gyrolite crystals have been simulated. The image in Figure IV-18 shows a thin platy pseudohexagonal crystal as generated from WinXmorph. Table IV-8 shows the faces used along with the respective distances from the centre of the crystal. The slow growing face *0 0 1* is responsible for the thin shape of the crystal. In addition the *1 1 1* face which is growing gives the pseudohexagonal shape to gyrolite.

The SEM micrographs of gyrolite crystals do not match perfectly with that generated using WinXmorph. The real crystals tend to have round edges compare to the simulated one. The reason for this is not clear yet. It is possible that another face is growing in the real crystals (as minor elements, present in the structure can disrupt crystal shapes) which could not be simulated.

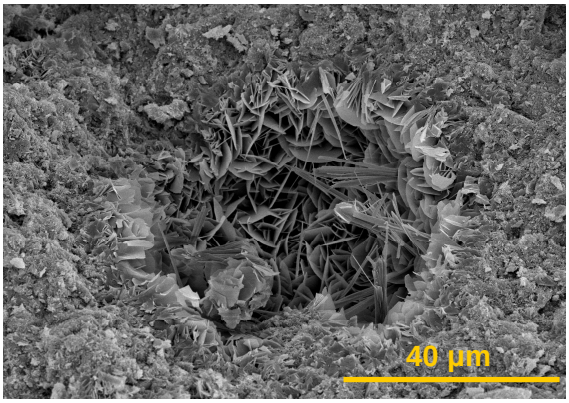

Figure IV-14: SEM micrograph of gyrolite crystals in sample cured at 200 ℃, containing 40 wt% of silica flour

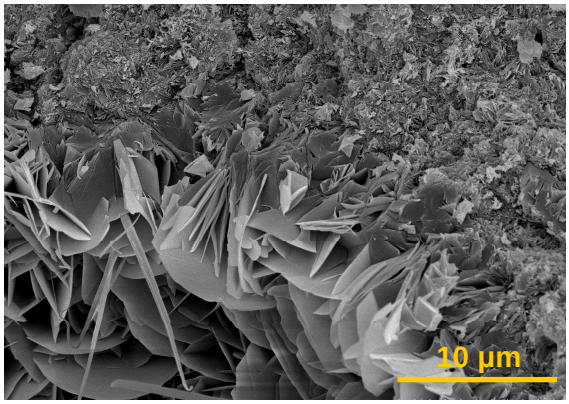

Figure IV-15: Increased magnification of the previous image presenting platy gyrolite crystals.

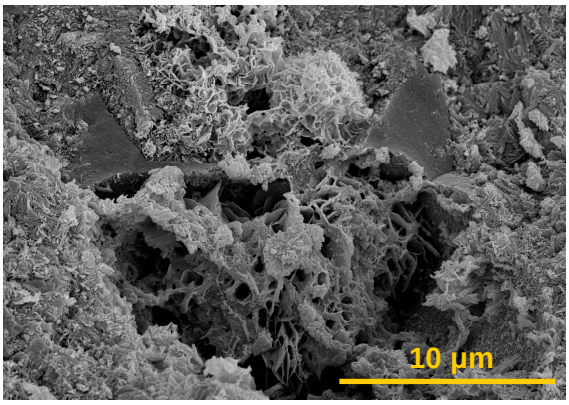

Figure IV-16: SEM micrograph of gyrolite crystals in sample cured at 250 ℃, containing 40 wt% of silica flour.

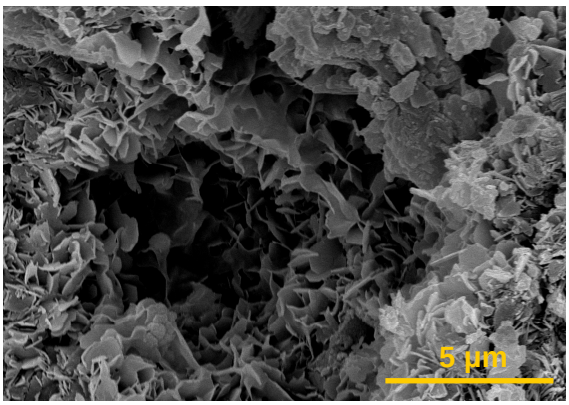

Figure IV-17: SEM micrograph of gyrolite crystals in sample cured at 250 ℃, containing 40 wt% of silica flour.

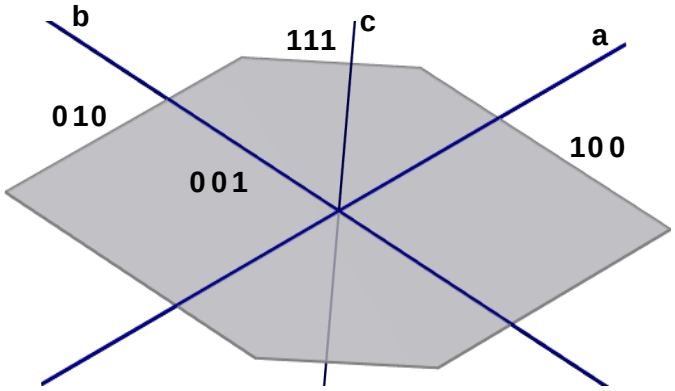

Figure IV-18: Gyrolite crystal along with the faces growing as simulated using WinXmorph.

Table IV-8: Distances of faces from the centre of the crystal.

Indices	Distance
1 0 0	1
1 1 1	0.8
0 1 0	1
0 0 1	0.001

IV- 2.4 Truscottite $Ca_{14}Si_{24}O_{62}•(4+z)H_2O$, $(0 \leq z \leq 6)$

Truscottite is a calcium silicate hydrate mineral structurally related to gyrolite [31]. In the $CaO\text{-}SiO_2\text{-}Al_2O_3\text{-}H_2O$ (CASH) hydroceramic system it is formed when more than 35 wt % of silica flour is added at temperatures more than 250 ℃ where it replaces gyrolite (Chapter II). The EPMA measurements carried out on a sample containing 40 wt % of silica flour and cured at 300 ℃ were unsuccessful. Therefore the chemistry of this mineral in the hydroceramic system has not been identified.

Truscottite forms thin platy hexagonal crystals. Figures IV-19 to IV-22 show truscottite crystals formed in the (CASH) hydroceramic system. The samples

examined, using SEM, were cured at two different temperatures 300 ℃ and 350 ℃ and both contain the same amount of silica flour (40 wt %).

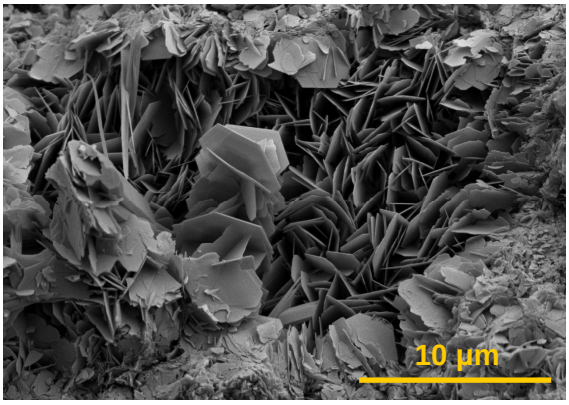

Figure IV-19: SEM micrograph of truscottite crystals in sample cured at 300 ℃, containing 40 wt% of silica flour.

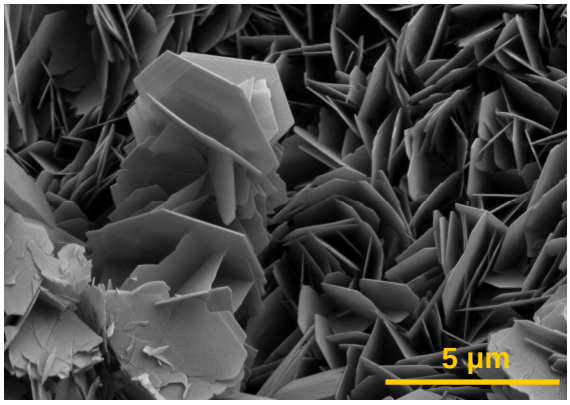

Figure IV-20: SEM micrograph of truscottite crystals in sample cured at 300 ℃, containing 40 wt% of silica flour.

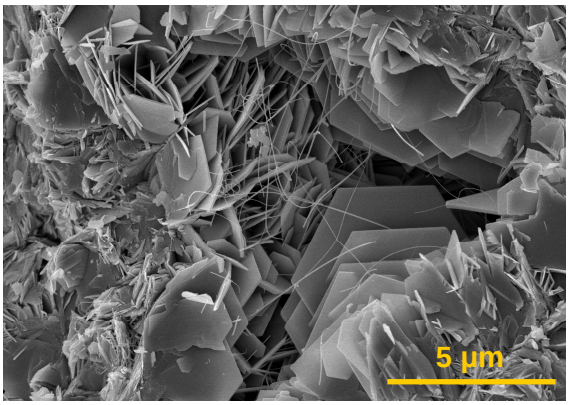

Figure IV-21: SEM micrograph of truscottite crystals in sample cured at 350 ℃, containing 40 wt% of silica flour. Needles observed are of xonotlite

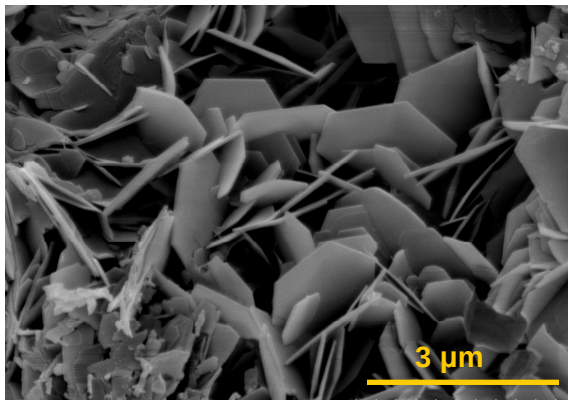

Figure IV-22: SEM micrograph of truscottite crystals in sample cured at 350 ℃, containing 40 wt% of silica flour.

Truscottite crystals belongs to the hexagonal system. Using WinXmorph and data from the International Crystal Structure Database (ICSD) [32] truscottite crystals have been simulated. The image in Figure IV-23 shows a thin platy hexagonal crystal as generated from WinXmorph which is identical with the SEM micrographs taken from CASH hydroceramics. In Table IV-9 the faces used to simulate the crystal along with the distances from the centre of the crystal are shown. According to WinXmorph, truscottite has a principle cleavage, parallel to the

0 0 1 face, perpendicular to the *c* axis. This face grows slower than the others as it has the less distance from the centre of the crystal (Table IV-9), hence the thin truscottite crystals. These results are in very good agreement with observations of natural and synthetic truscottites [32].

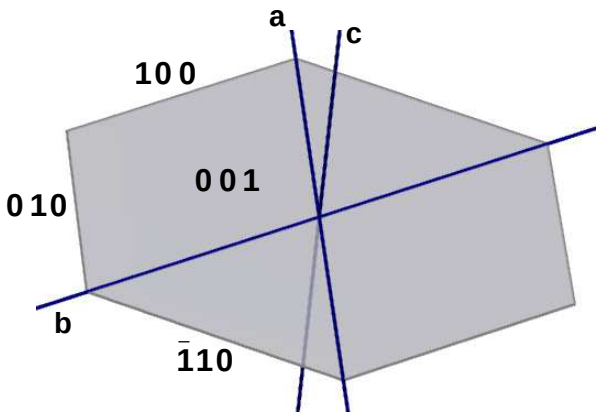

Figure IV-23: Truscottite crystal along with the faces growing as simulated using WinXmorph.

Table IV-9: Distances of faces from the centre of the crystal.

Indices	Distance
1 0 0	1
0 1 0	1
0 0 1	0.001

IV- 3. Conclusions

Four calcium silicate hydrate minerals in the $CaO\text{-}SiO_2\text{-}Al_2O_3\text{-}H_2O$ (CASH) hydroceramic system have been studied: xonotlite, 11Å tobermorite, gyrolite and truscottite. These minerals form in the hydroceramic system at temperatures between 200 ℃ to 350 ℃ and have CaO/SiO_2 mole ratio ≤1.

The CaO/SiO_2 mole ratio of xonotlite is found to be in good agreement with that of the pure phase. However the weight percent of Ca and Si was lower than expected and the water content was higher. We believe that high water content is associated with Ca and Si deficiency in order for the mineral to obtain the charge balance by incorporating water molecules in the structure. Xonotlite is believed to form topotactically from tobermorite; hence the Ca deficiency. The silicon deficiency can be explained as the tobermorite structure is also deficient in Si in the CASH hydroceramic system as revealed from EPMA.

The substitution of Al for Si is not rare in xonotlites and we have shown here that temperature does not affect the amount of aluminum present in the structure. In addition a correlation between temperature and the Al_2O_3/Fe_2O_3 ratio exists. As temperature increases the amount of iron in xonotlite increases. Possibly other phases present in the sample, which incorporate iron in their structure, might affect the iron absorption of xonotlite. Other elements are present in xonotlite, such as magnesium, potassium, sodium and sulphur. However some of these elements are absent from xonotlite when it coexists with other phases. When gyrolite is formed in sample containing 40 wt % of silica flour and cured at 200 ℃ xonotlite does not contain sodium, potassium and magnesium as most of these elements are incorporated in gyrolite. Additionally when truscottite is formed in sample cured at 300 ℃ and containing 40 wt % of silica flour xonotlite contains no sodium or potassium.

Xonotlite forms needle shaped crystals. The simulated crystals generated with WinXmorph were identical with those shown in the SEM micrographs. Using WinXmorph we have shown here that the crystals are elongated parallel to the *b* axis and the growth face is the *0 1 0*; hence producing the needle shape.

Tobermorite chemistry studied here uses one sample, containing 30 wt % of silica flour and cured at 200 ℃. The results indicate that the amount of water in the structure corresponds to 11Å tobermorite. The Ca/(Al+Si) and Al/(Al+Si) atomic ratios are in good agreement with reports on natural and synthetic specimens of

these minerals. In addition substitution of iron for silicon is lower than aluminum for silicon as shown from the EPMA measurements. This substitution creates a charge imbalance and in order to maintain charge neutrality univalent cations such as sodium and potassium are incorporated in tobermorite structure with the following order $Na^+ < K^+$. In addition the low Ca/(Al+Si) atomic ratio due to high Al and the high contents of alkali present such as Na and K suggest the presence of the anomalous type, in accordance with previous authors observations.

In addition to 11Å tobermorite, the sample studied contains xonotlite and it is shown that the sample reached equilibrium. Moreover, when xonotlite and tobermorite are present all aluminium, potassium and sodium in the sample is distributed between these two phases.

11Å tobermorite crystallizes in two different shapes: thin, platy, pseudohexagonal and needle-like, corresponding to the normal and the anomalous type respectively. Both of these types have been simulated using WinXmorph. According to these results slow growth on the *0 0 1* face produces the thin shape, where as rapid growth on the *0 1 0* along the *b* axis hence produces the needle shape of the anomalous form. The SEM results showed no evidence of platy crystals in the sample examined reinforcing the conclusion from the EPMA that the anomalous type of 11Å tobermorite is present in the CASH hydroceramic system.

Gyrolite water content is variable with the *n* value in the chemical formula, lying between 0 and 3. EPMA results show here that the *n* value in gyrolite present in the hydroceramics is 0.7. In addition the atomic ratios of Ca/(Al+Si) and Al/(Al+Si) are in good agreement with previous authors. The coupled substitution between Al^{3+} for Si^{4+} and Fe^{3+} for Ca^{2+} creates a charge imbalance. Therefore sodium and potassium are incorporated in the structure to maintain neutrality. Gyrolites exhibit selectivity in these elements in the order of $Na^+ < K^+$ which is confirmed here.

The sample containing gyrolite also contains xonotlite. When these two phases are present all the magnesium, potassium and sodium is incorporated in the gyrolite structure, where as the aluminum is distributed between the both.

The SEM micrographs taken from samples cured at different temperatures show that the shape of gyrolite in the hydroceramic system is thin plates but the edges are more rounded than the pseudohexagonal form previously reported. The simulated crystals from WinXmorph were not identical with those observed from the SEM. Possibly another face is growing which could not be simulated. In addition the information obtained using WinXmorph shows that the *0 0 1* face of gyrolite grows

slowly, hence the thin shape and the growth of *1 1 1* face is responsible for the pseudohexagonal shape.

Truscottite chemistry has not been discussed here as the EPMA measurements were unsuccessful. The SEM micrographs of truscottite show that this mineral forms thin hexagonal crystals. The simulated crystal generated using WinXmorph was identical with the real ones found in the hydroceramics. In addition according to the information revealed from the simulated crystals truscottite has the principal cleavage, parallel to the *0 0 1* face, perpendicular to the *c* axis.

IV- 4. References

1. S. A. Bilgrami and R. A. Howie, "The mineralogy and petrology of a Rodingite Dike, Hindubagh, Pakistan," *American Mineralogist,* **45** [7-8] 791-801 (1960).

2. A. R. Grimmer and W. Wieker, "Determination of type of water bond in xonotlite $6CaO6SiO_2H_2O$," *Zeitschrift für Anorganische und Allgemeine Chemie,* **384** [1] 34-& (1971).

3. G. L. Kalousek, T. Mitsuda, and H. F. W. Taylor, "Xonotlite: cell parameters, thermogravimetry and analytical electron microscopy," *Cement and Concrete Research,* **7** 305-312 (1977).

4. H. F. W. Taylor, "The transformation of tobermorite into xonotlite," *Mineralogical Magazine,* **32** [245] 110-116 (1959).

5. J. J. Esteban, J. Cuevas, and J. M. Tubia, "Xonotlite in rodingite assemblages from the Ronda Peridotites, Betic Cordilleras, southern Spain," *The Canadian Mineralogist,* **41** 161-170 (2003).

6. C. Hejny and T. Armbruster, "Polytypism in xonotlite $Ca_6Si_6O_{17}(OH)_2$," *Zeitschrift fur Kristallographie,* **216** [7] 396-408 (2001).

7. H. Noma, Y. Adachi, Y. Matsuda, and T. Yokoyama, "^{29}Si and ^{1}H NMR of natural and synthetic xonotlite," *Chemistry Letters,* [3] 219-220 (1998).

8. Q. Guangren, X. Guangling, L. Heyu, and L. Aimei, "Mg-Xonotlite and it's co-existing phases," *Cement and Concrete Research,* **27** 315-320 (1997).

9. O. P. Shrivastava, S. Komarneni, and E. Breval, "Mg^{2+} uptake by synthetic tobermorite and xonotlite," *Cement and Concrete Research,* **21** [1] 83-90 (1991).

10. H. de Bruiyn, A. E. Schoch, W. A. van der Westhuizen, and G. J. Beukes, "The chemical composition of xonotlite and associated inesite from the Nchwaning and Wessels mines, Kalahari manganese field, South Africa," *Neues Jahrbuch Fur Mineralogie-Monatsheft,* [5] 212-222 (1999).

11. K. Garbev, L. Black, G. Beuchle, and P. Stemmermann, "Inorganic polymers in cement based materials," *Wasser und Geotechnologie,* **2** 19-30 (2002).

12. E. Bonaccorsi, S. Merlino, and A. R. Kampf, "The crystal structure of tobermorite 11Å (Plombierite), a C-S-H phase," *Journal of the American Ceramic Society,* **88** [3] 505-512 (2005).

13. S. Merlino, E. Bonaccorsi, and T. Armbruster, "Tobermorites: Their real structure and order-disorder (OD) character," *American Mineralogist,* **84** 1613-1621 (1999).

14. S. Merlino, E. Bonaccorsi, and T. Armbruster, "The real structures of clinotobermorite and tobermorite 9Å: OD character, polytypes, and structural relationships," *European Journal of Mineralogy,* **12** [2] 411-429 (2000).

15. T. Mitsuda and H. F. W. Taylor, "Normal and anomalous tobermorites," *Mineralogical Magazine,* **42** 229-235 (1978).

16. T. Mitsuda, K. Sasaki, and H. Ishida, "Phase evolution during autoclaving process of aerated concrete," *Journal of the American Ceramic Society,* **75** [7] 1858-1863 (1992).

17. M. Sakiyama, T. Maeshima, and T. Mitsuda, "Al-substituted tobermorite 11 Å: Synthesis, analytical electron microscopy, NMR spectroscopy and cell parameters", pp. 899-902 in *Applied Mineralogy, Vols 1 and 2 - Research, Economy, Technology, Ecology and Culture***.** Edited by D. Rammlmair, J. Mederer, T. Oberthur, R. B. Heimann, and H. Pentinghaus. A. A. Balkema, Rotterdam, 2000.

18. T. Pannaparayil, S. Komarneni, E. Breval, D. M. Roy, and L. N. Mulay, "Fe^{3+}-substituted tobermorites: Synthesis and characterization by Mossbauer spectroscopy and other techniques," *Materials Research Bulletin,* **20** [12] 1393-1400 (1985).

19. S. Diamond, J. L. White, and W. L. Dolch, "Effects of isomorphous substitution in hydrothermally-synthesized tobermorite," *American Mineralogist,* **51** 388-401 (1966).

20. M. Miyake, S. Komarneni, and R. Roy, "Kinetics, equilibria and thermodynamics of ion-exchange in substituted tobermorites," *Materials Research Bulletin,* **24** [3] 311-320 (1989).

21. G. L. Kalousek and A. F. Prebus, "Crystal chemistry of hydrous calcium silicates: III, morphology and other properties of tobermorite and related phases," *Journal of the American Ceramic Society,* **41** 124-132 (1958).

22. G. L. Kalousek, "Crystal chemistry of hydrous calcium silicates: I, substitution of aluminum in lattice of tobermorite," *Journal of the American Ceramic Society,* **40** 74-80 (1957).

23. S. Merlino, E. Bonaccorsi, and T. Armbruster, "The real structure of tobermorite 11Å: normal and anomalous forms, OD character and polytypic modifications," *European Journal of Mineralogy,* **13** 577-590 (2001).

24. H. F. W. Taylor,"*Cement Chemistry*" 2nd. London, Thomas Telford Publishing, 1997.

25. S. Merlino, "Gyrolite: its crystal structure and crystal chemistry," *Mineralogical Magazine,* **52** [366] 377-387 (1988).

26. A. L. Mackay and H. F. W. Taylor, "Gyrolite," *Mineralogical Magazine,* **30** 80-91 (1953).

27. R. N. Sukheswa, R. K. Avasia, and Gangopad.M, "Zeolites and associated secondary minerals in deccan traps of western India," *Mineralogical Magazine,* **39** [306] 658-671 (1974).

28. N. J. Elton, J. J. Hooper, and V. A. D. Holyer, "Al-free gyrolite from the Lizard, Cornwall, England," *Mineralogical Magazine,* **62** [2] 271-272 (1998).

29. M. Miyake, M. Iwaya, T. Suzuki, H. Kakehi, and T. Mitsuda, "Aluminum-substituted gyrolite as cation exchanger," *Journal of the American Ceramic Society,* **73** [11] 3524-3527 (1990).

30. J. W. Meyer and K. L. Jaunarajs, "Synthesis and crystal chemistry of gyrolite and reyerite," *The American Mineralogist,* **46** [7-8] 913-933 (1961).

31. J. A. Gard, T. Mitsuda, and H. F. W. Taylor, "Some observations on Assarsson's Z-phase and its structural relations to gyrolite, truscottite and reyerite," *Mineralogical Magazine,* **40** [312] 325-333 (1975).

32. A. L. Mackay and H. F. W. Taylor, "Truscottite," *Mineralogical Magazine,* **30** 450-457 (1954).

CHAPTER V

CALCIUM ALUMINUM SILICATE HYDRATE (CASH) MINERALS

V- 1. Introduction

Minerals of the grossular – katoite hydrogarnet series $Ca_3Al_2(SiO_4)_{3-y}(OH)_{4y}$ ($0 \leq y \leq 3$) are major products of the hydration of calcium aluminate cements [1], and are produced in small amounts in Portland cements hydrated at ambient temperatures [2]. At elevated temperatures hydrogarnets are also observed in cement based hydroceramic well sealants where the alumina content exceeds 5 weight percent. Meller *et al.* [3,4] have recently designed materials based on the $CaO\text{-}SiO_2\text{-}Al_2O_3\text{-}H_2O$ (CASH) system at 200 to 350 ℃ for use under hydr othermal conditions. In alumina-rich CASH systems hydrogarnets are the major products.

Calcium aluminum oxide hydrate ($Ca_4Al_6O_{13}\bullet 3H_2O$) which is known as well as tetracalcium trihydrotrialuminate is another phase present in the CASH hydroceramic system. In contrast with hydrogarnets, which form in the whole range of temperatures (200-350 ℃), this phase is present only at higher temperatures (300 and 350 ℃) when the alumina addition exceeds 15 weight percent (see Chapter II).

The present study investigates the chemistry of hydrogarnets and calcium aluminum oxide hydrate using electron probe microanalysis. In addition the hydrogarnets chemistry has been studied further using X-ray diffraction as well as the crystal shape of this phase using scanning electron microscopy (SEM) and WinXmorph. The experimental techniques used are described in detail in Chapters II and III.

V- 2. Results and Discussion

V- 2.1 Hydrogarnets $Ca_3Al_2(SiO_4)_{3-y}(OH)_{4y}$, $0 \leq y \leq 3$

V- 2.1.1 X-ray diffraction

When alumina is added to cement, hydrogarnet is the most common aluminum-bearing phase formed at these curing temperatures. This phase is also present when hydrating cement alone without additions, although at temperatures 200 and 250 ℃ the relatively small amounts cannot be quantified as hydrogarnet peaks overlap those of other phases (Table V-1). The mineralogy of the samples cured at 200 and 250 ℃ is similar. On adding small amounts of alumina, portlandite [$Ca(OH)_2$] and jaffeite [$Ca_6(Si_2O_7)(OH)_6$] form together with the hydrogarnet phase.

In these samples reinhardbraunsite [$Ca_5(SiO_4)_2(OH)_2$] is also present at 250 ℃ rather than α-dicalcium silicate hydrate [α-$Ca_2SiO_3(OH)_2$] which is formed at 200 ℃. As more alumina is added, jaffeite is the only phase to co-exist with hydrogarnet at these temperatures together with some relict corundum. At 300 ℃ calcium aluminum oxide hydrate (also known as tetracalcium trihydrotrialuminate, $Ca_4Al_6O_{13}•3H_2O$) forms in addition to the phases mentioned previously, and at 350 ℃ bicchulite [$Ca_8(Al_2SiO_6)_4(OH)_8$] is present (Table V-1).

When small amounts of both silica and alumina are added to cement at 200 ℃, kilchoanite [$Ca_6(SiO_4)(Si_3O_{10})$] and tobermorite [$Ca_5Si_6O_{17}•5(H_2O)$] form, together with jaffeite, hydrogarnet and corundum. As more silica is added to the system, xonotlite [$Ca_6Si_6O_{17}(OH)_2$] replaces kilchoanite. At 250 ℃ kilchoanite is no longer found and only jaffeite, hydrogarnet, tobermorite, xonotlite and corundum form, the amounts depending on the proportions of the starting materials (Table V-1). The same minerals form at 300 ℃ and. At 350 ℃ when on ly small amounts of silica and alumina are added we also observe foshagite [$Ca_4(Si_3O_9)(OH)_2$]. As can be seen from Table V-1 the mineralogy of this system (CASH) is complicated. A full quantitative and qualitative description of this CASH system is given in Chapter II and elsewhere [3-5]. Here data concerning only the hydrogarnets will be reported.

Table V-1: Phases identified in each sample and weight percent of hydrogarnet present as estimated by Rietveld refinement. Codes for phases: *a* α-dicalcium silica hydrate; *b* bicchulite; *c* corundum; *d* calcium alumina hydrate; *f* foshagite; *hgnt* hydrogarnet; *j* jaffeite; *k* kilchoanite; *p* portlandite; *q* quartz; *r* reinhardbraunsite; *t* 11Å tobermorite; *x* xonotlite.

Proportions (wt %)			200 ℃			250 ℃			300 ℃			350 ℃		
Dyckerhoff cement	**Silica flour**	**a-Al_2O_3**	**% hgnt**	***y***	**Other phases**	**% hgnt**	***y***	**Other phases**	**% hgnt**	***y***	**Other phases**	**% hgnt**	***y***	**Other phases**
100	0	0			*p, j, a*			*p, j, r*	16	1.6	*p, j, r*	15	1.3	*p, j, r*
95	0	5	40	1.9	*p, j, a*	47	1.8	*p, j, r*	61	1.8	*p, j*	69	1.7	*p, j*
90	0	10	64	2.0	*p, j*	87	2.1	*p, j, r*	76	1.9	*p, j*	82	1.8	*p, j*
85	0	15	82	2.0	*p, j*	87	2.1	*p, j*	88	2.0	*p, j*	81	2.0	*p, j, d*
80	0	20	97	2.1	*j*	92	2.1	*j*	83	2.1	*j, d*	72	2.0	*p, j, d, b*
75	0	25	88	2.2	*j, c*	82	2.1	*j, c*	$hgnt_1$ = 71 $hgnt_2$ = 3	2.1 1.0	*j, d*	60	2.0	*j, c, d, b*
70	0	30	80	2.1	*j, c*	75	2.1	*j, c*	$hgnt_1$ = 63 $hgnt_2$ = 4	2.1 1.0	*j, d*	56	2.0	*d, b, c*
65	0	35	74	2.1	*j, c*	70	2.1	*j, c*	62	2.0	*j, c, d*	51	2.0	*d, b, c*
60	0	40	73	2.1	*j, c*	62	2.1	*j, c*	47	2.0	*j, c, d*	43	2.0	*d, b, c*
55	0	45	60	2.1	*j, c*	55	2.1	*j, c*	49	2.1	*j, c, d*	40	2.0	*d, b, c*
50	0	50	55	2.2	*j, c*	51	2.2	*j, c*	44	2.0	*j, c, d*	35	2.0	*d, b, c*
80	10	10	49	1.6	*j, k, t, c*	89	1.5	*j*	93	1.4	*j*	75	1.3	*p, j, f, x*
70	10	20	61	1.6	*j, k, t, c*	88	1.5	*c*	$hgnt_1$ = 62 $hgnt_2$ = 31	1.4 1.0	*j*	$hgnt_1$ = 46 $hgnt_2$ = 33	1.2 0.9	*p, x*
70	20	10	30	1.4	*t, x, c*	48	1.3	*t, x, c*	63	1.0	*x*	$hgnt_1$ = 44 $hgnt_2$ = 35	1.2 0.8	*x*
60	10	30	68	1.5	*j, t, c*	67	1.4	*t, c*	$hgnt_1$ = 47 $hgnt_2$ = 35	1.5 0.9	*c*	$hgnt_1$ = 37 $hgnt_2$ = 36	1.1 0.7	*x*
60	20	20	26	1.4	*t, x, c*	34	1.2	*t, x, c*	$hgnt_1$ = 12 $hgnt_2$ = 21	1.1 0.8	*x*	14	0.8	*c*
50	10	40	54	1.5	*t, c*	48	1.3	*t, x, c*	$hgnt_1$ = 35 $hgnt_2$ = 28	1.3 0.9	*x*	65	0.8	*c, b*

It is known that hydrogarnets $Ca_3Al_2(SiO_4)_{3-y}(OH)_{4y}$ form a solid solution from grossular (y=0) to katoite (y=3) [6] with the existence of a miscibility gap reported at 95 ℃ between compositions $2.24< y<2.58$ [7]. To distinguish the intermediate members of this mineral series, Passaglia and Rinaldi [8] proposed the mineral name hibschite for the silica-rich members (50-100 % grossularite composition, $0\leq y\leq 1.5$) and katoite for the water-rich members (0-50 % grossularite composition, $1.5\leq y\leq 3$). In order to find the chemical composition of the hydrogarnets present in the CASH system three simple linear regression equations have been used, obtained by plotting the y value against the d-spacings of three major peaks (400, 420, and 521) of known hydrogarnet patterns from the International Centre for Diffraction Data (ICDD) database. These equations are then used to estimate the y value of the hydrogarnets present in the CASH system from the observed d-spacings (Figure V-1). The reason for obtaining the y value from three different equations is for accuracy therefore the results presented here are an average of these three values. The error in y is typically less than 5 %. In some cases (Figure V-1 lower pattern) more than one hydrogarnet is present therefore two y values were calculated. The splitting of the X-ray diffraction peaks has also been observed from Jappy and Glasser [7]. They confirmed by small area electron diffraction that the two different peaks did not represent two different hydrogarnet crystal structures or polymorphs but rather different chemical compositions (y values) of the same structure. It is possible that the broad peaks observed for some hydrogarnets, where only one peak is observed (Figure V-1 upper pattern), may represent a range of compositions and our estimate of y therefore represents an average composition for the sample.

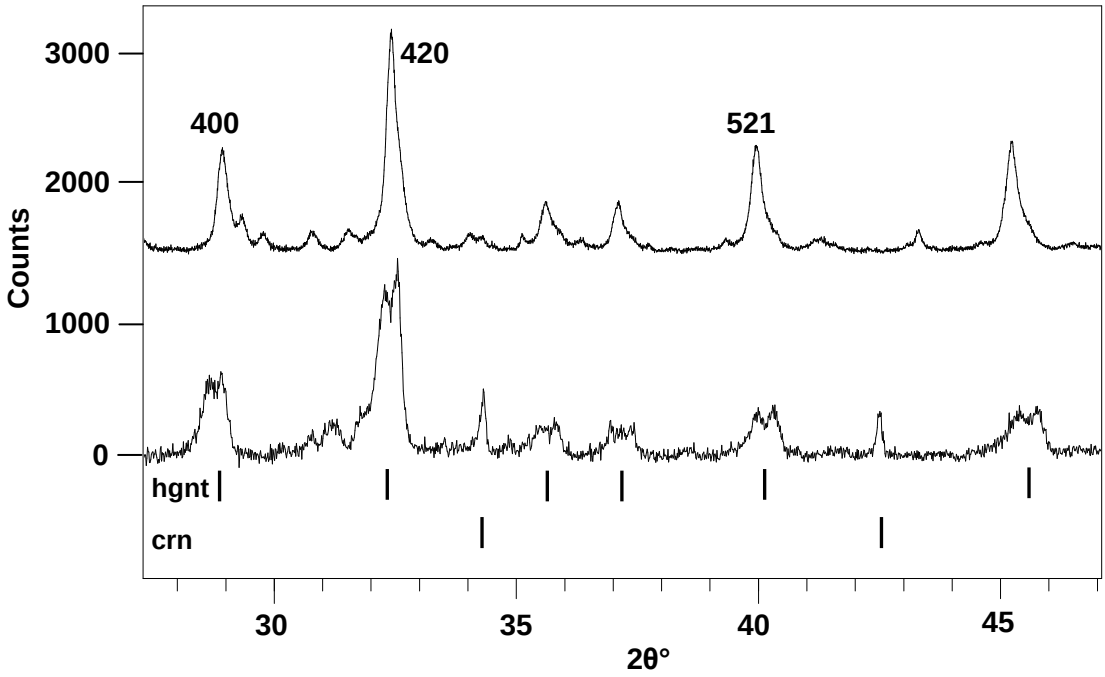

Figure V-1: X-ray diffraction profiles of samples containing hydrogarnets (*hgnt*). The upper sample was synthesized at 200 ℃ and contains 20 wt% of alumina. The lower sample was synthesized at 350 ℃ and contains 20 wt % silica flour and 10 wt% alumina illustrating the presence of two distinct hydrogarnets (*hgnt*) with split 400, 420 and 521 peaks. Some relict alumina as corundum (*crn*) is present in the lower pattern.

Plotting $CaO/(CaO+Al_2O_3)$ in terms of molar proportions against *y* (Figure V-2a) shows that when up to 15 wt % of alumina ($CaO/(CaO+Al_2O_3)$ = 0.85) is added to the system *y* has a small increase, and above this value the composition remains constant close to the katoitic form of hydrogarnet ($y \approx 2.1$). When plotting $CaO/(CaO+SiO_2)$ in terms of molar proportions against *y*, (Figure V-2b) a continuous decrease of *y* is observed as more silica is added to the system suggesting that the composition of hydrogarnets tends towards the hibschitic area ($y<1.5$). In addition temperature also appears to influence *y* in both cases, and there is a tendency to move towards lower *y* values at higher temperatures. Whether this is because the upper temperature limit of katoitic hydrogarnet is being approached or the calcium, aluminum and water are entering a new phase ($Ca_4Al_6O_{13}\bullet 3H_2O$ or bicchulite) above 250 ℃ is unclear. However hydrogarnet compositions with *y* values more than 2.2 have not been observed in the CASH hydroceramic system, although it could be possible according to the stoichiometry (cement + additives). These results are consistent with the view of Jappy and Glasser [7] that a miscibility gap exists in the

hydrogarnet series between compositions 2.24<*y*<2.58, although we could not verify the upper limit of the miscibility gap in these temperatures (200–350°C).

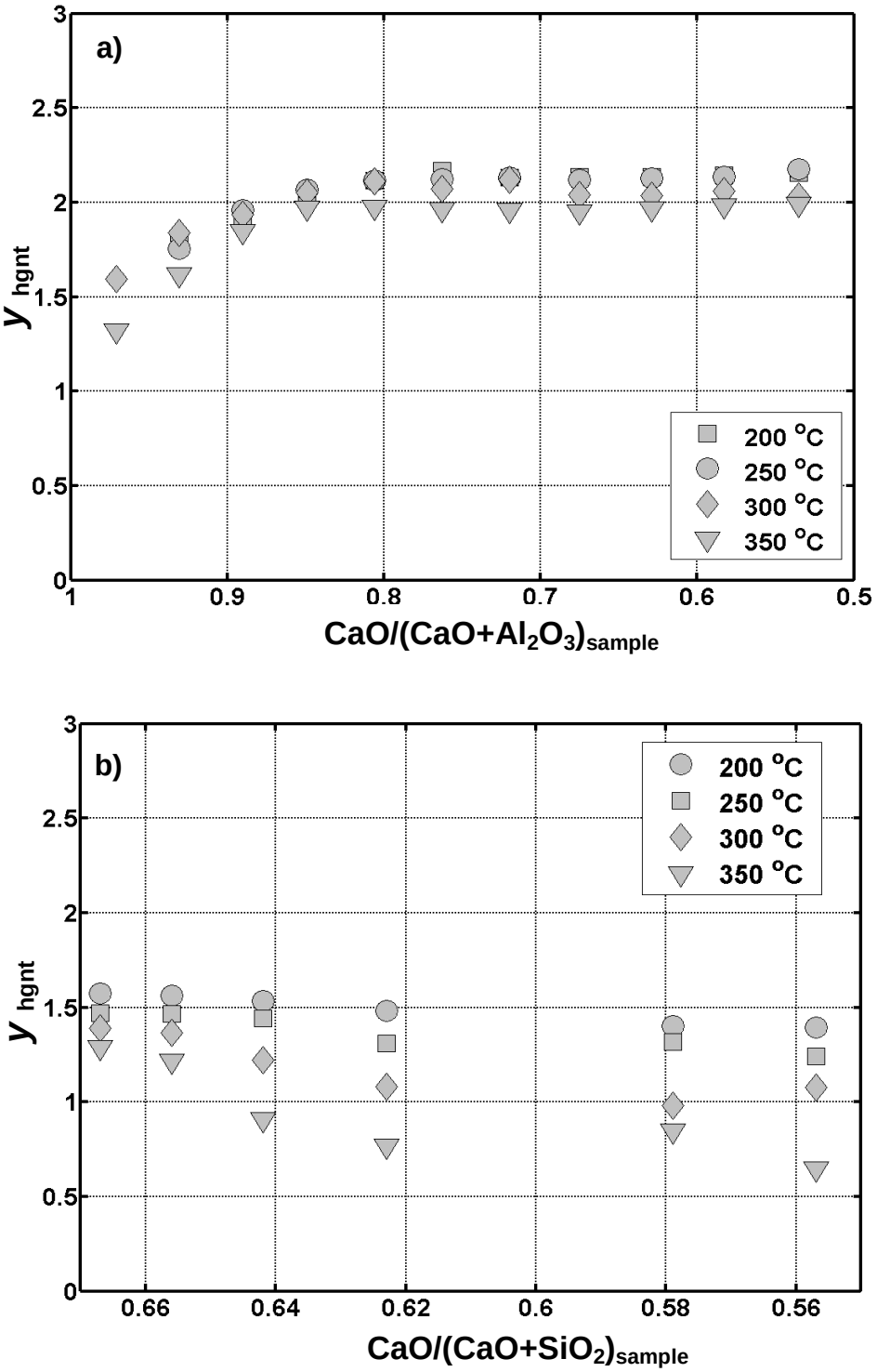

Figure V-2: The *y* value of hydrogarnets measured from X-ray diffraction patterns at different temperatures plotted against the molar proportions of the sample: a) $CaO/(CaO+Al_2O_3)$, b) $CaO/(CaO+SiO_2)$.

Once the *y* value is calculated the occupancy factors of Si and H are determined and fed into the Rietveld refinement process to calculate the unit cell size. As the *d*-spacing is directly proportional to the unit cell size a correlation between the *y* and the unit cell size is expected as well. Two structures are used for this process: the Sacerdoti [9] katoite structure as default but where the *y* value is significantly low (<0.8) the Cohen-Addad [10] hibschite structure is used. Indeed Figure V-3 shows that there is a correlation between the *y* and the unit cell size, an observation noted by others [11,12], and enhances our confidence that Rietveld refinement is a reliable tool for the quantification of these types of materials. In addition it is noted that the unit cell size is dependent on the chemistry of the hydrogarnet (Figure V-3). As temperature is increased the unit cell size of the hydrogarnets tends to lower values, suggesting that when fewer $(OH)^-$ groups are present in the structure the unit cell size tends towards to lower values i.e. at higher temperatures the hydrogarnet becomes more anhydrous (dehydrated).

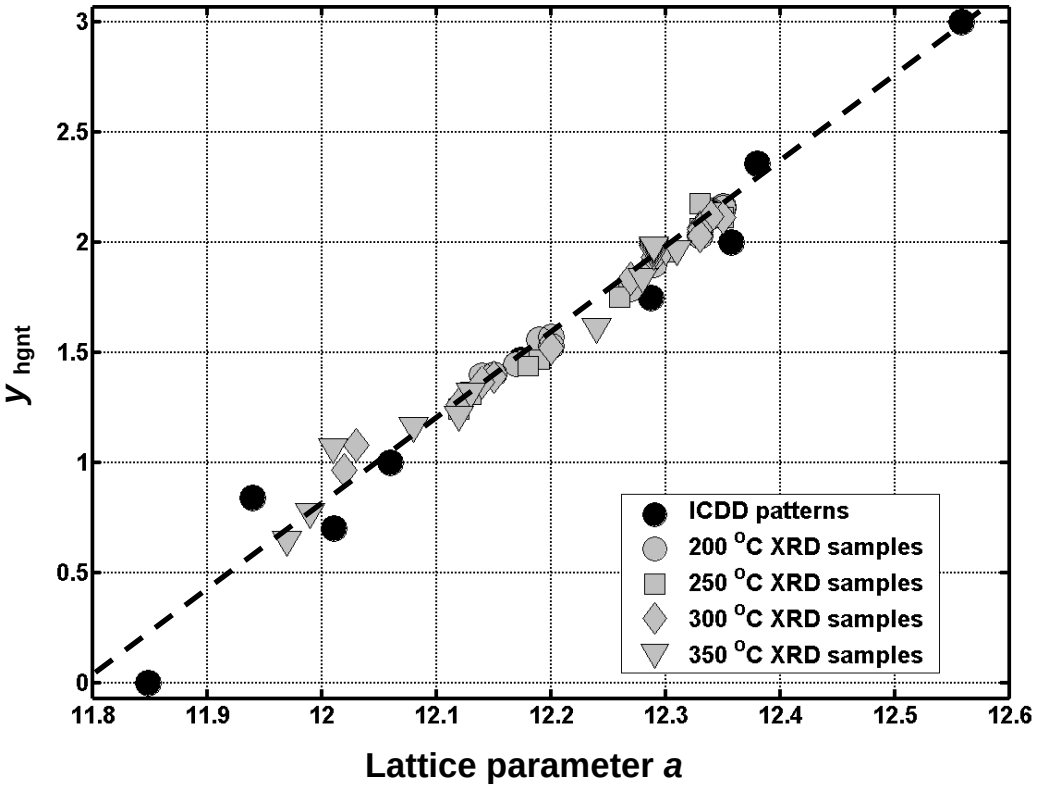

Figure V-3: Plot presenting the *y* value of hydrogarnet against the unit cell size at different temperatures.

V- 2.1.2 Electron Probe Microanalysis (EPMA)

EPMA analysis has been carried out on samples cured at 200 ℃, 250 ℃ and 300 ℃ to verify the composition of the hydrogarnets calculated from XRD measurements. Each sample has been measured in different areas. The results obtained in Table V-2 are in most cases an average of at least 25 measurements on each sample (with a minimum of 10 measurements in a few cases). Note that the electron microprobe measurements have been carried out on hydrogarnet aggregates (we have observed that hydrogarnets form aggregates of approx 15 µm see Chapter VI) and not on individual crystallites. It is considered that the statistics are sufficiently good to provide reliable compositional information. There was little evidence of heterogeneity in composition in the hydrogarnets. The backscattered images of the hydrogarnet areas were generally uniform and apparently compositionally homogeneous. A typical error between these measurements is less than 10 %. The analysis was based on 12 oxygens and the weight percent of water is calculated as the difference from 100 % of the total.

The analyses reveal the presence of minor elements such as Fe, Mg and S in addition to Ca, Si and Al. According to the general chemical formula of hydrogarnets $Ca_3Al_2(SiO_4)_{3-y}(OH)_{4y}$ a substitution of $4OH^-$ for SiO_4^{4-} occurs, as first described by Cohen-Addad [10]. Naturally occurring hydrogarnets as well as hydrogarnets growing in cements lie on the composition of $Ca_3(Al,Fe)_2(SiO_4)_{3-y}(OH)_{4y}$ exhibit a substitution between Al^{3+} and Fe^{3+} [2]. In mature cement pastes Taylor and Newbury [13] proposed a composition of $Ca_3Al_{1.2}Fe_{0.8}SiO_{12}H_8$ for the hydrogarnet phase, but Rodger and Groves [14] suggested $Ca_3Al_{0.6}Fe_{0.6}(SiO_4)(OH)_y$. Our results (Table V-2) showed that Fe is present in lower concentrations, between 0.04 and 0.22 and that Mg and S are present as well. The presence of these elements is not rare in naturally occurring hydrogarnets [8,15,16], Mg substitutes for Al in the octahedral sites creating a charge imbalance of +1. This imbalance is partially compensated by sulfur, as sulfate, which substitutes $(SO_4)^{2-}$ and the presence of extra water in the structure. Indeed the composition we find for the hydrogarnet formed in the CASH system with 20 wt % of corundum cured at 200 ℃ is

$$Ca_{3.3}\,(Al_{1.87}\,Fe_{0.04}\,Mg_{0.04})_{\Sigma=1.95}\,(Si_{1.15}\,S_{0.07})_{\Sigma=1.22}\,O_{5.66}\,(OH)_{6.31}$$

Table V-2: Electron probe microanalysis of samples containing hydrogarnets. The values for each sample are an average of at least 10 measurements in different areas of the sample.

Temperature	**200 ℃**							**250 ℃**	**300 ℃**			
Cement (wt %)	90	80	70	55	70	60	50	70	90	80	70	55
α-alumina (wt %)	10	20	30	45	20	30	40	30	10	20	30	45
Silica flour (wt %)	0	0	0	0	10	10	10	0	0	0	0	0
Wt percent of oxides												
CaO	43.26	44.43	44.35	40.55	40.33	40.63	40.97	41.13	43.79	43.70	40.00	41.37
SiO_2	17.32	16.42	15.99	15.37	23.96	23.98	24.19	13.55	16.85	16.90	14.92	13.21
Al_2O_3	20.44	22.63	22.93	24.35	13.98	18.04	18.10	23.52	18.35	20.51	26.29	23.96
MgO	0.40	0.35	0.30	0.30	0.75	0.62	0.52	0.58	0.61	0.40	0.41	0.59
Fe_2O_3	0.85	0.90	1.10	1.12	4.30	2.34	1.25	2.90	2.63	1.36	0.84	0.91
SO_3	2.13	1.45	1.55	1.42	1.86	1.36	1.45	1.40	2.30	1.20	1.14	0..90
TOTAL	84.44	86.18	86.22	83.11	85.18	86.97	86.48	83.08	84.53	84.07	83.06	80.84
H_2O	15.60	13.82	13.78	16.89	14.82	13.03	13.52	16.92	15.75	15.93	16.4	19.16
Formula based on 12 oxygens												
Ca	3.20	3.30	3.30	2.94	2.98	3.02	3.02	2.86	3.20	3.20	2.96	2.99
Si	1.19	1.15	1.12	1.00	1.65	1.66	1.66	1.07	1.17	1.16	1.02	0.88
Al	1.66	1.87	1.90	1.94	1.14	1.47	1.47	1.73	1.5	1.67	2.1	1.90
Mg	0.04	0.04	0.03	0.03	0.07	0.06	0.05	0.05	0.06	0.04	0.04	0.04
Fe^{3+}	0.04	0.04	0.06	0.06	0.22	0.12	0.06	0.15	0.14	0.06	0.04	0.04
S	0.10	0.07	0.08	0.07	0.09	0.07	0.07	0.06	0.10	0.06	0.06	0.05
H	6.81	6.31	6.34	7.35	6.45	5.84	6.07	8.10	6.9	7.10	6.78	8.08
y	1.89	1.85	1.88	2.00	1.35	1.34	1.34	1.93	1.83	1.90	1.98	2.12

showing more water in structure, confirming our previous suggestion, as well as almost all the samples examined in Table V-2. Paul and Glasser [17] discussed the composition of hydrogarnets found in prolonged warmed-cured Portland cement pastes at 85 ℃ confirming the existence of iron, magnesium and sulfur in their structure. The amounts found in their experiments were higher than this study although the Portland cement that they used had a different composition than ours. It has been reported [18] that titanium can also be present in hydrogarnets although in this study it has not detected by EPMA although this oxide is present in the cement used (Chapter II, Table II-1).

The amount of Fe_2O_3, MgO and SO_3 that the hydrogarnet phase absorbs from the cement (Chapter II, Table II-1) can be calculated. The weight percent of the hydrogarnets from the Rietveld refinement is known in each sample (Table V-1). In addition the total mass of the reagents used is also known; therefore from mass/matter conservation and the EPMA chemical formulae (Table V-2) we can estimate the mass of Fe_2O_3, MgO and SO_3 that hydrogarnets contain and compare it with that of the whole sample. Figure V-4 shows that almost all the SO_3 and the MgO from the cement are incorporated into the hydrogarnet structure whereas only part of the Fe_2O_3 is incorporated into the hydrogarnet. In some cases the values of SO_3 or MgO in Figure V-4 are slightly higher in the hydrogarnet compared to the whole sample, suggesting an overestimation of the amount of hydrogarnet by the Rietveld refinement process. When alumina only is added to the system at 200 ℃ Fe_2O_3 is in very low concentrations in the hydrogarnet and seems to increase when adding more alumina. On the other hand when both alumina and silica are added the amount of Fe_2O_3 in the structure is high at low additions of alumina and decreases as the amount of alumina is increased. At 300 ℃ when alumina is added the behaviour of the system is the same as at 200 °C. The reason for the differences in the amount of iron present in hydrogarnet is probably related to the other phases growing in the system and their ability to contain iron in their respective structures.

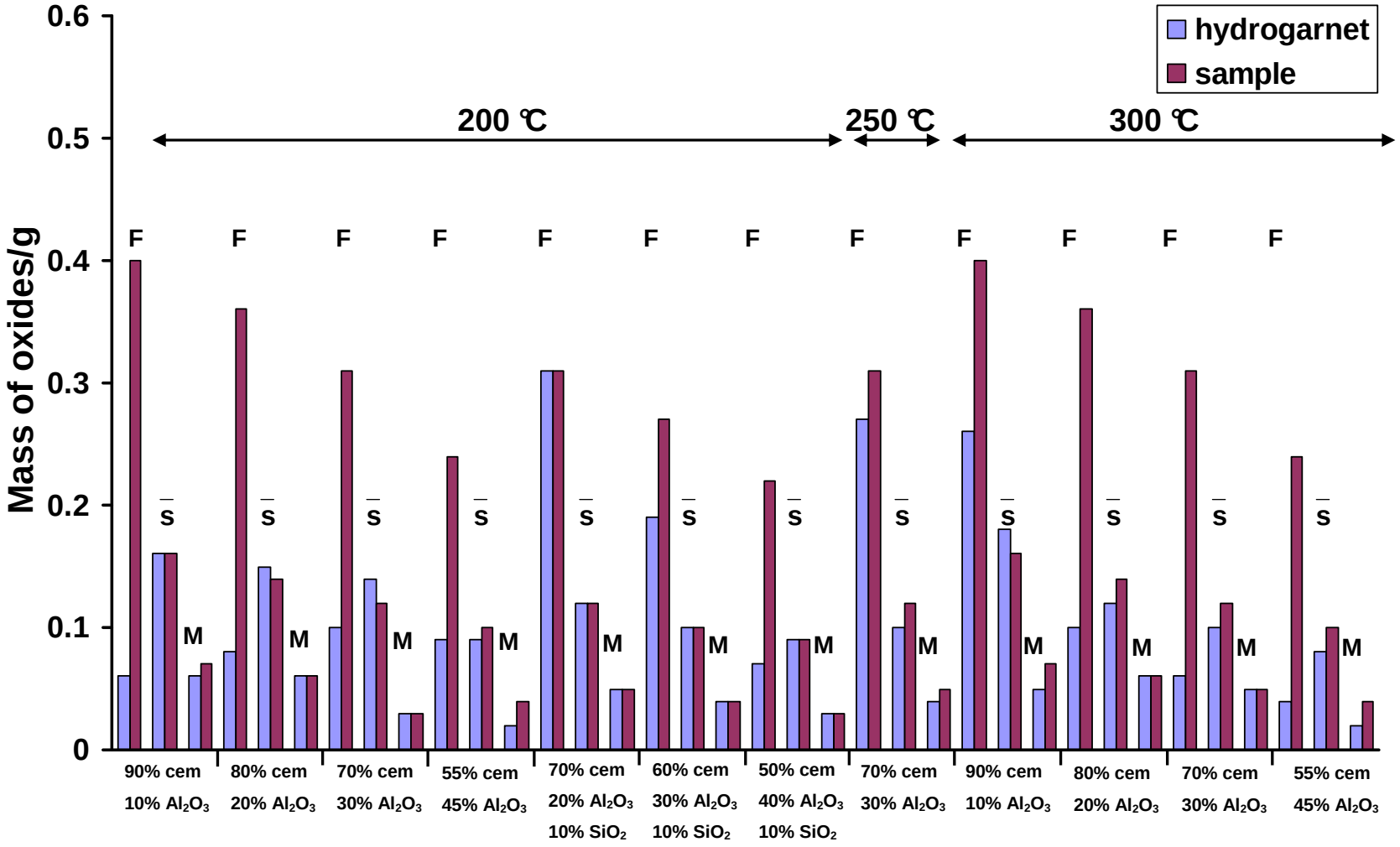

Figure V-4: Plot illustrating the weight of F=Fe_2O_3, $\bar{S}$=SO_3 and M=MgO contained in hydrogarnet structure and in the whole sample.

The *y* value can be calculated from the chemical formulae of each sample measured with the EPMA from the relation $y = 3 - (Si)$. A good agreement between the estimates for *y* from XRD and EPMA is observed in Fig. 5. The slight overestimate of the XRD values is probably due to the minor elements present in the hydrogarnet structure.

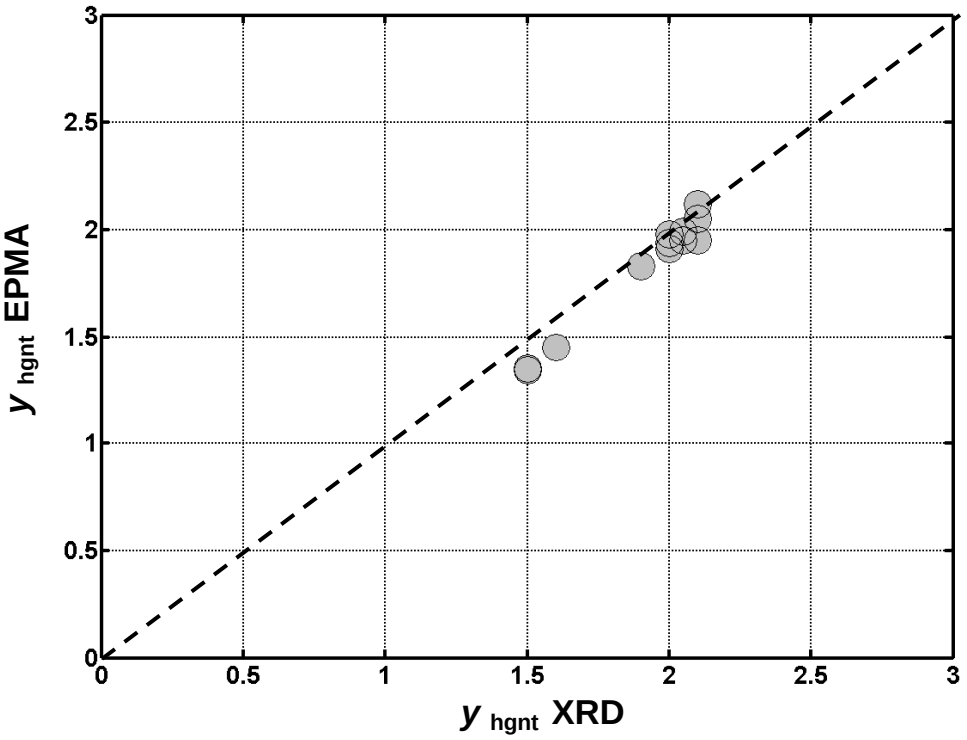

Figure V-5: Comparison of *y* value of hydrogarnet calculated with electron probe microscopy and with x-ray diffraction.

V- 2.1.3 Scanning Electron Microscopy (SEM)

SEM images reveal the presence of two different hydrogarnet crystal shapes (Figure V-6). Figure V-6a illustrates the octahedral morphology of a hydrogarnet crystal with an approximate size of 500 nm grown in a sample containing 10 wt % alumina and cured at 200 ℃. This morphology is com mon and it has been reported for hydrogarnets growing both in nature [8,15] and in cement pastes [19-22]. Figure V-6c shows an icositetrahedral (trapezohedron) hydrogarnet (~ 500nm size) grown in a sample containing 10 wt % alumina and cured at 300 ℃. This shape is reported

here for the first time in cement pastes at these temperatures but it has been observed before in cements at ambient temperature [23,24].

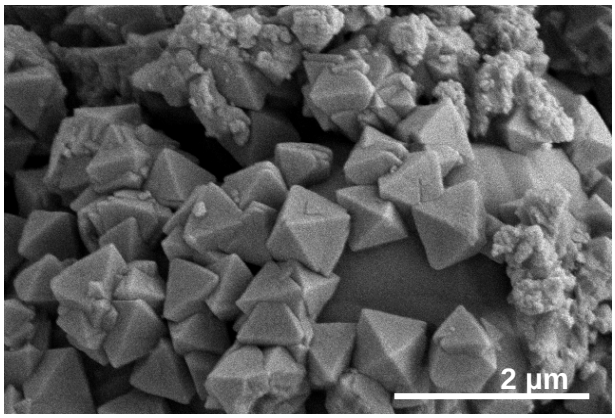

a)

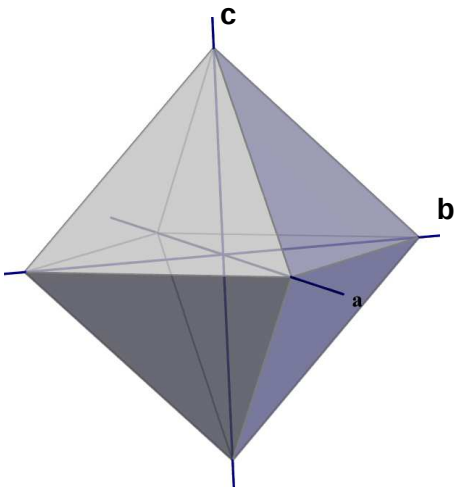

b)

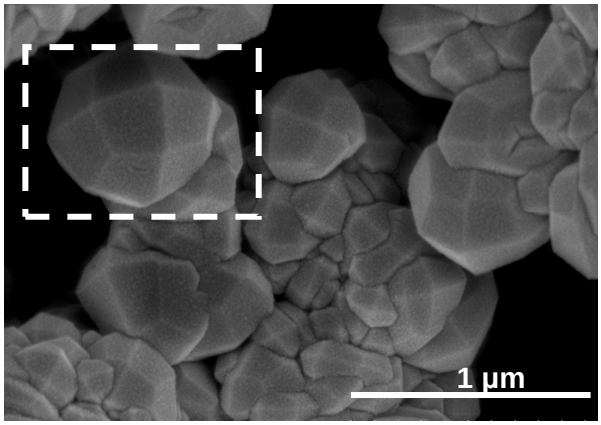

c)

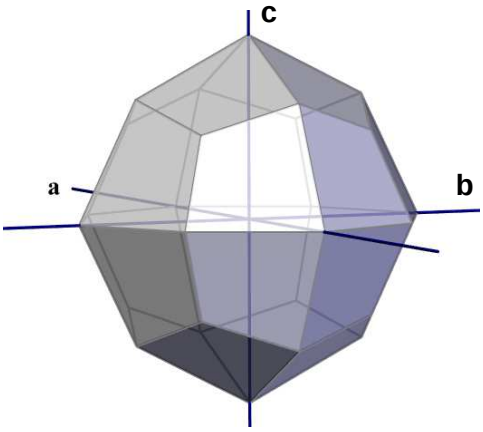

d)

Figure V-6: SEM images illustrating the different hydrogarnet shapes grown in cement pastes at elevated temperatures. **(a)** octahedral hydrogarnet grown in sample containing 10 wt% of alumina cured at 200 ℃, **(b)** crystal habit, predicted using WinXmorph, is dominated by the 1 1 1 family faces, **(c)** icositetrahedral hydrogarnet grown in sample containing 10 wt% of alumina cured at 300 ℃, **(d)** crystal habit is dominated by the 1 1 2 family faces.

Different crystal habits exist for garnets [25] and in order to simulate the hydrogarnet crystal shape, we have used the WinXMorph program [26,27]. In this study data from the International Crystal Structure Database (ICSD) [28,29] has been used. Since the crystal system of hydrogarnets is cubic (isometric), Figure V-6b shows that the octahedral crystal habit, predicted using WinXmorph, is dominated by the family of the 1 1 1 faces whereas in the icositetrahedral shape (Figure V-6d) the observed crystal habit is dominated by the 1 1 2 family.

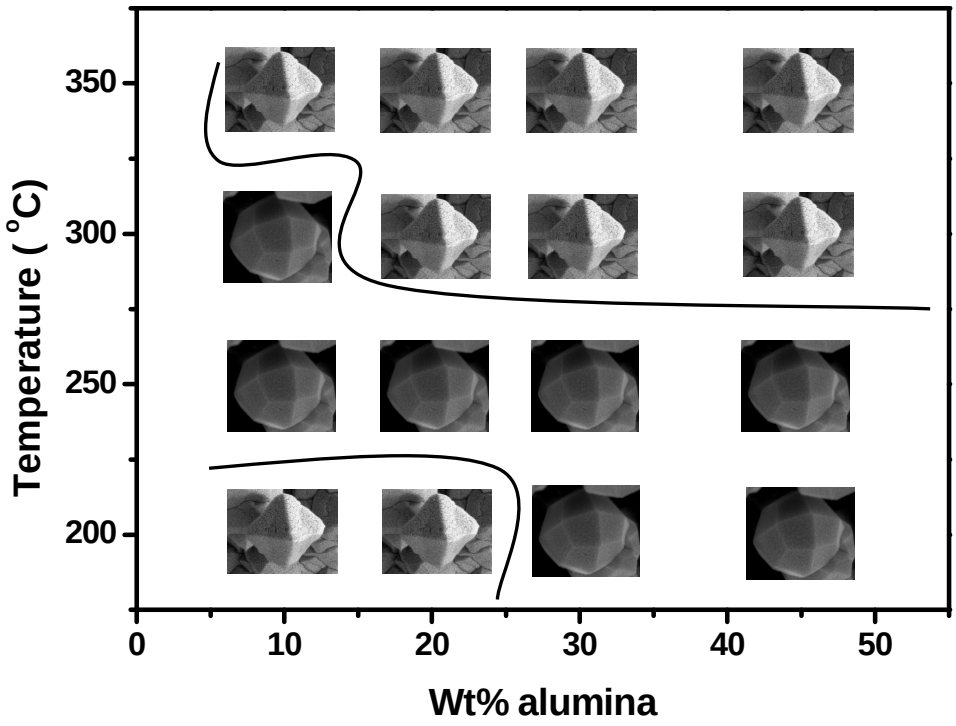

Figure V-7: Plot illustrating the different hydrogarnet shapes in samples with alumina additions only.

When both alumina and silica are added to the system the hydrogarnets have the octahedral shape at all temperatures, suggesting that when this phase is in the hibschitic region (y~1) the shape remains constant regardless of the chemistry. On the other hand Figure V-7 shows the differences in morphology when adding alumina only to the system so the hydrogarnet is in the katoitic area (y~2). The icositetrahedral shape is present in samples cured at 200 ℃ and containing 30 and 45 wt % of alumina, in all the samples cured at 250 ℃ and in sample containing 10 wt % of alumina cured at 300 ℃. The reason for the different crystal habits is still

unclear. We note however that the trace elements are in high concentrations in these samples e.g. Fe^{3+} (as seen from EPMA measurements) and this, combined perhaps with the low silicon content (due to high *y*) may favor the 1 1 2 family of faces through a crystal growth inhibition mechanism as yet unidentified.

V- 2.2 Calcium Aluminum Oxide Hydrate $Ca_4Al_6O_{13}•3H_2O$

Calcium aluminum oxide hydrate, a phase which is met regularly in the hardening of high alumina-cements [30], is present in the CaO-SiO_2-Al_2O_3-H_2O (CASH) hydroceramic system when more than 15 wt % of alumina is added at temperatures between 300 and 350 ℃. The chemistry of this phase has been studied using EPMA. Two different samples have been examined, cured at the same temperature (300 ℃) but with different amounts of alumina added. The analysis of calcium aluminum oxide hydrate is based on 15 oxygens and the weight percent of water is calculated as the difference from 100 % of the total. A typical error between these measurements is less than 8 %.

In Table V-3 are presented the results from the electron probe microanalysis. In these two samples 20 and 30 wt % of alumina is added respectively. The results are an average of at least 20 measurements carried out in calcium aluminum oxide hydrate grains.

Table V-3: EPMA results of calcium aluminum oxide hydrate. Both samples cured at 300 ℃ but contain different amounts of alumina.

Temperature	300 ℃	
Cement (wt %)	80	70
α-alumina (wt %)	20	30
	Wt percent of oxides	
CaO	39.85	38.39
SiO_2	3.45	1.37
Al_2O_3	45.47	48.58
Fe_2O_3	0.42	0.33
TOTAL	89.19	88.67
H_2O	10.81	11.33
	Formula based on 15 oxygens	
Ca	3.85	3.70
Si	0.30	0.12
Al	4.85	5.13
Fe^{3+}	0.03	0.02
H	6.35	6.64

Figure V-8a shows a general view of a sample containing the calcium aluminum oxide hydrate phase. The specific sample cured at 300 ℃ and 30 wt % of alumina is added. In Figure V-8b the same sample is presented at higher magnification along with the calcium aluminum oxide hydrate phase examined using EPMA. The five different points analysed on the specific phase are also indicated. The black colour around the part examined is a pore and the darker grey colour grains around are of hydrogarnet previously studied. From these two images (the circles in Figure V-8a are showing other examples similar to Figure V-8b) it can be concluded that this phase grows between the hydrogarnet aggregates.

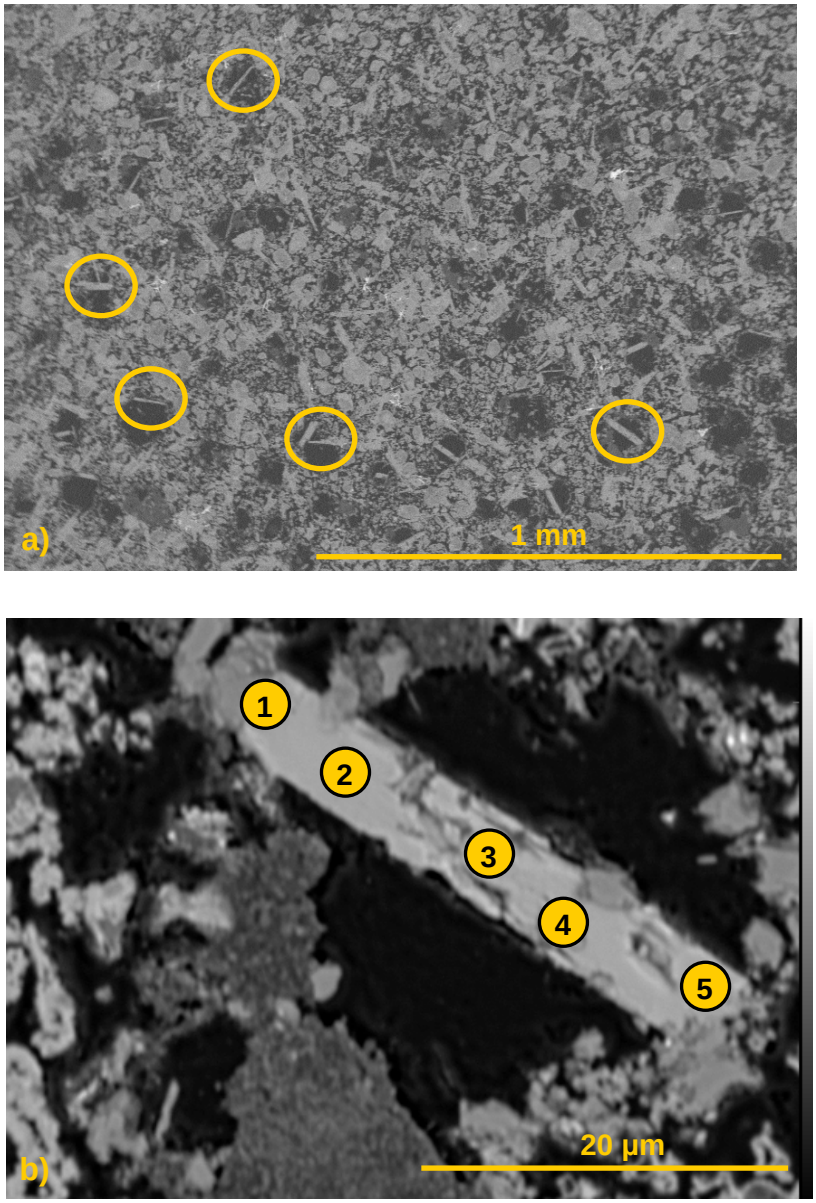

Figure V-8: a) Low magnification view of a sample containing calcium aluminum oxide hydrate. The sample cured at 300 ℃ and contains 30 wt % of alumina. **b)** Backscattered image presenting a grain of calcium aluminum oxide which is studied using EPMA found in the same sample.

The chemistry of this phase as revealed from the EPMA in the samples containing 20 and 30 wt % of alumina respectively is:

$$Ca_{3.85}Si_{0.30}Al_{4.85}Fe_{0.03}O_{11.78} \bullet 3.17H_2O$$

$$Ca_{3.70}Si_{0.12}Al_{5.13}Fe_{0.02}O_{11.67} \bullet 3.32H_2O$$

According to my knowledge the chemistry of this phase in cement based materials is studied here for the first time. However its crystal structure has been examined previously by others [30,31].

The chemical formulae of calcium aluminum oxide hydrate shows lack of calcium and aluminum in the structure. However two other elements are present. Iron probably substitutes aluminum in the structure. Silicon is present in higher amounts compared to iron although it is uncertain which element substitutes. While the substitution of iron with aluminum does not influence the charge balance the silicon substitution creates a charge imbalance. This is probably neutralized by the incorporation of more water molecules in the structure as shown from the chemical formulae. In addition a decrease is observed in the amount of silicon and an increase in the amount of aluminum in these two formulae. The explanation is that as more alumina is added to the system (from 20 wt % to 30 wt %) more aluminum is incorporated in the structure. The decrease in silicon has to do with the decrease in the amount of cement (which is the source of silica in these samples) as more alumina is added.

V- 3. Conclusions

An examination has been carried out on the properties of hydrogarnets produced by curing cements at elevated temperatures with silica and alumina additions. An intimate relationship exists between the chemistry, the crystal structure and the crystal shape of the hydrogarnets formed under such conditions and our main conclusions can be summarized as follows:

Hydrogarnet is the dominant aluminum bearing phase when pastes of cement and alumina are cured at temperatures between 200 and 350 ℃.

The composition of hydrogarnets depends on the amount of silica in the CASH system and strongly on the curing temperature.

The unit cell size depends on the *y* value and hence the chemical composition of the hydrogarnet.

Hydrogarnets with $y > 2.2$ have not been observed in the CASH system, thus supporting the view of Jappy and Glasser that there is a miscibility gap in the solid solution series.

Minor elements such as iron, magnesium and sulphur are present in the hydrogarnet structure, which are derived from cement. All the sulphur and magnesium contained in cement enters the hydrogarnet structure, whereas iron resides in other phases in addition to hydrogarnet.

Two different crystal shapes of hydrogarnets have been observed, octahedral and icositetrahedral and the shape is probably influenced by the presence of the minor elements.

In addition the chemistry of calcium aluminum oxide hydrate has been studied in this Chapter. The results showed that the amounts of calcium and aluminum in the structure are not in good agreement with the ideal phase. In addition two other elements are present such as iron and silicon. This phase appears to grow between the hydrogarnet aggregates.

V- 4. References

1. J. Bensted, "Calcium aluminate cements", pp. 114-138 in *Structure and Performance of Cements***.** Edited by J. Bensted and P. Barnes. Spon Press, London, 2002.

2. H. F. W. Taylor, "*Cement Chemistry*", London, Thomas Telford Publishing, 1997.

3. N. Meller, C. Hall, and J. Phipps, "A new phase diagram for the CaO-Al_2O_3-SiO_2-H_2O hydroceramic system at 200 ˚C," *Materials Research Bulletin,* **40** [5] 715-723 (2005).

4. N. Meller, K. Kyritsis, and C. Hall, "The mineralogy of the CaO-Al_2O_3-SiO_2-H_2O (CASH) hydroceramic system from 200 to 350 ℃," *Cement and Concrete Research,* (accepted).

5. N. Meller, C. Hall, K. Kyritsis, and G. Giriat, "Synthesis of cement based CaO-Al_2O_3-SiO_2-H_2O (CASH) hydroceramics at 200 and 250 ℃: Ex-situ a nd in-situ diffraction " *Cement and Concrete Research,* **37** [6] 823-833 (2007).

6. M. Schoenitz and A. Navrotsky, "Enthalpy of formation of katoite $Ca_3Al_2[(OH)_4]_3$: Energetics of the hydrogarnet substitution," *American Mineralogist,* **84** [3] 389-391 (1999).

7. T. G. Jappy and F. P. Glasser, "Synthesis and Stability of Silica-Substituted hydrogarnet $Ca_3Al_2Si_{3-x}O_{12-4x}(OH)_{4x}$," *Advances in Cement Research,* **4** [1] 1-8 (1991).

8. E. Passaglia and R. Rinaldi, "Katoite, a new member of of the $Ca_3Al_2(SiO_4)_3$-$CaAl_2(OH)_{12}$ series and a new nomenclature for the hydrogrossular group of minerals," *Bulletin of Mineralogie,* **107** [5] 605-618 (1984).

9. M. Sacerdoti and E. Passaglia, "The crystal structure of katoite and implications within the hydrogrossular group of minerals," *Bulletin de Mineralogie,* **108** [1] 1-8 (1985).

10. C. Cohen-Addad, P. Ducros, and E. F. Bertaut, "Etude de la substitution du groupement SiO_4 par $(OH)_4$ dans les composes $Al_2Ca_3(OH)_{12}$ et $Al_2Ca_3(SiO_4)_2.16(OH)_{3.36}$ de type grenat," *Acta Crystallographica,* **23** 220-230 (1967).

11. R. Siauciunas and A. Baltusnikas, "Influence of SiO_2 modification on hydrogarnets formation during hydrothermal synthesis," *Cement and Concrete Research,* **33** [11] 1789-1793 (2003).

12. T. Matchei, B. Lothenbach, and F. P. Glasser, "Thermodynamic properties of Portland cement hydrates in the system CaO-Al_2O_3-SiO_2-$CaSO_4$-$CaCO_3$-H_2O," *Cement and Concrete Research,* **37** 1379-1410 (2007).

13. Taylor H. F. W. and Newbury D. E., "An Electron Microprobe Study of a Mature Cement Paste," *Cement and Concrete Research,* **14** [4] 565-573 (1984).

14. Rodger S. A. and Groves G. W., "Electron Microscopy Study of Ordinary Portland Cement and Orinary Portland Cement-Pulverized Fuel Ash Blended Pastes," *Journal of the American Ceramic Society,* **72** [6] 1037-1039 (1989).

15. A. Pabst, "Re-examination of Hibschite," *American Mineralogist,* **27** [12] 783-792 (1942).

16. R. Rinaldi and E. Passaglia, "Hibschite topotype: crystal chemical characterisation," *European Journal of Mineralogy,* **1** [5] 639-644 (1989).

17. M. Paul and F. P. Glasser, "Impact of prolonged warm (85 ^{o}C) moist cure on Portland cement paste," *Cement and Concrete Research,* **30** [12] 1869-1877 (2000).

18. Lachowski E. E., Mohan K., Taylor H. F. W., C. D. Lawrence, and A. E. Moore, "Analytical electron ,microscopy of cement pastes: III, Pastes hydrated for long times," *Journal of the American Ceramic Society,* **64** [6] 319-321 (1981).

19. D. S. Klimesch and A. S. Ray, "Effect of quartz content on the nature of Al-substituted 11Å tobermorite in hydrothermally treated CaO-Al_2O_3-SiO_2-H_2O systems," *Advances in Cement Research,* **11** [4] 179-187 (1999).

20. D. S. Klimesch and A. S. Ray, "Effects of quartz particle size on hydrogarnet formation during autoclaving at 180 ℃ in the CaO-Al_2O_3-SiO_2-H_2O system," *Cement and Concrete Research,* **28** [9] 1309-1316 (1998).

21. D. S. Klimesch and A. Ray, "Hydrogarnet formation during autoclaving at 180 ^{o}C in unstirred metakaolin-lime-quartz slurries," *Cement and Concrete Research,* **28** [8] 1109-1117 (1998).

22. S. Fujita, S. Suzuki, Y. Shibasaki, and Mori T., "Synthesis of hydrogarnet from molten slag and its hydrogen chloride fixation performance at high temperatures," *Journal of Material Cycles Waste and Management,* **4** [1] 70-76 (2002).

23. K. L. Scrivener and A. Capmas, "Calcium aluminate cements", pp. 713-775 in *Lea's chemistry of cement & concrete***.** Edited by P. C. Hewlett. Butterworth-Heineman, Oxford, 1998.

24. P. Meredith, A. M. Donald, N. Meller, and C. Hall, "Tricalcium aluminate hydration: microstructural observation by in situ electron microscopy," *Journal of Materials Science,* **39** [3] 997-1005 (2004).

25. K. Cornelis, C. S. Hurlbut , and D. J. Dana, "*Manual of Mineralogy*" New York, John Wiley & Sons, 1985.

26. Kaminsky W., "WinXMorph: a computer program to draw crystal morphology, growth sectors and cross sections with export files in VRML V2.0 utf8-virtual reality format," *Journal of Applied Crystallography,* **38** [3] 566-567 (2005).

27. Kaminsky W., "From CIF to virtual morphology using the WinXMorph program," *Journal of Applied Crystallography,* **30** [2] 382-385 (2007).

28. G. A. Lager, T. Armbruster, F. J. Rotella, and G. R. Rossman, "OH substitution in garnets: X-ray and neutron diffraction, infrared, and geometric-modeling studies," *American Mineralogist,* **74** [7-8] 840-851 (1989).

29. Lager G.A., Marshall W.G., Liu Z., and Downs R.T.V, "Re-examination of the hydrogarnet structure at high pressure using neutron powder diffraction and infrared spectroscopy.," *American Mineralogist,* **90** [4] 639-644 (2005).

30. V. I. Ponomarev, D. M. Kheiker, and N. V. Belov, "Crystal structure of tetracalcium trihydrotrialuminate $C_4A_3H_3$," *Doklady Akademii Nauk SSSR,* **194** 1072-1075 (1970).

31. A. Percival and H. F. W. Taylor, "Unit cell and space group of $4CaO.3Al_2O_3.3H_2O$," *Acta Crystallographica,* **14** [3] 324-& (1961).

CHAPTER VI

ENGINEERING PROPERTIES OF HYDROCERAMICS

VI- 1. Introduction

Cement is universally used in the construction of oil and geothermal wells. Cement slurries are placed primarily to secure and support the casing inside the well, but also to prevent entry of unwanted fluids into the well and communication between formation fluids at different levels [1]. These cements need to perform for many years at high temperatures and in severe chemical environments, such as in brines or ground waters containing carbon dioxide [2]. Such environments can cause the material of the well-casing to degrade resulting in reduced strength and increased permeability [3-6]. It is therefore necessary for cement formulations to be sufficiently durable and resistant to chemical attack in order to seal the well for its working life.

Typical working temperatures for these wells are between 200 ℃ and 350 ℃ and when the temperature exceeds 110 ℃ special cement formulations are used [1]. There have been several recent attempts to design cements which are more durable at higher temperatures. Meller *et al.* [7-10] have designed slurries based on the $CaO–Al_2O_3–SiO_2–H_2O$ (CASH) system, the aim being to develop formulations suitable for geothermal and deep, hot oil wells. These formulations contain minerals which occur in nature and hence have the potential properties required to be good well sealants, i.e. low permeability, high strength and long-term stability. The mineralogy and the quantification of the phases present in this system are described in detail in Chapter II.

The physical properties of cementitious materials required for such applications have been investigated previously [1,11-18] and it is considered that the minimum compressive strength of the hardened slurry should be at least 7 MPa and the maximum permeability approximately 9×10^{-17} m^2 (1×10^{-9} ms^{-1} or 0.1 mD) [19]. Although some work has been done on the mechanical properties of cement-based well sealants, little is known about the relationship between these bulk properties and the microstructure of these materials. This is addressed here with respect to the CASH hydroceramic system; in addition the measured permeability of real samples is compared with that calculated from microstructural information.

VI- 2. Experimental procedures

VI- 2.1 Materials synthesis

Three reagents were used in the synthesis of the hydroceramic materials described here. Dyckerhoff oilwell cement (API Class G) was the base component in all samples. Silica flour (HPF6 supplied by Sibelco) with a mean grain size of 53 μm and α-alumina (corundum, supplied by Sigma Aldrich) with a grain size of 50 μm to 150 μm were used as the sources of SiO_2 and Al_2O_3 respectively.

Two different sized specimens were made. To examine compressive strength, cylindrical polytetrafluoroethylene (PTFE) cups were used, 22 mm in diameter and 45 mm deep. For permeability measurements smaller cups were used of the same diameter but only 30 mm deep. A total of 30 g of the three starting materials was weighed out in different proportions (Table VI-1) and 12 g of water added corresponding to a water:solids ratio of 0.4.

Table VI-1: Proportions of starting materials in samples cured at 200, 250, 300 and 350 ˚C.

Proportions (wt %)		
Dyckerhoff cement	**Silica Flour HPF6**	**α-Alumina**
100	0	0
90	10	0
80	20	0
70	30	0
60	40	0
50	50	0
90	0	10
80	0	20
70	0	30
60	0	40
50	0	50
80	10	10
60	10	30
60	20	20
60	30	10
50	10	40
50	40	10

Each sample was mixed by hand for approximately 3 min and then loaded into the appropriate cup. For the samples cured at 350 ℃, stainless steel cups were used, as PTFE was close to its melting point. The samples were stacked in a stainless steel autoclave cell of 125 mL capacity with a pressure rating of 200 bar at the maximum working temperature of 350 ℃. Small notches were cut in the rims of the PTFE and steel cups to ensure a uniform water-saturated atmosphere throughout the vessel.

Once the cells were sealed, they were placed in the oven at the selected curing temperature in the range of 200 ℃ to 350 ℃ and left to equilibrate for 5 d. After 5 d, the cells were removed from the oven and left to cool slowly under vacuum to prevent cracking before removal from the cups.

VI- 2.2 Characterization techniques

VI- 2.2.1 Tensile tester

The experiments were performed using an Instron 3360 standard testing machine (Figure VI-1a) operated in strain control. The crosshead of the machine is moved by a high precision screw drive. The actual measured quantities are time and force. Time can then be translated into a machine extension. The imposed extension can be used to get an approximation of the strain in the sample if the sample dimensions are known.

$$\varepsilon = \frac{\Delta l}{l} \qquad \text{(VI-1)}$$

Where ε is the strain and l the length of the sample.

The force was measured by a load cell attached to the crosshead of the machine. The recorded force F can then be used to calculate the stress σ in the sample by using the equation (VI-2) and knowing the sample cross-section area A.

$$\sigma = \frac{F}{A} \qquad \text{(VI-2)}$$

The load cell contains four strain gauges which are assembled in a full bridge, which makes it insensitive to temperature variations. The cell was calibrated before every session using the automatic calibration function of the machine. In all the experiments compression method was used with the two stainless steel plates

depicted in Figure VI-1b transmitting the load onto the samples. This grip setup is rigid in the sense that it can only move in the direction of the axial applied load.

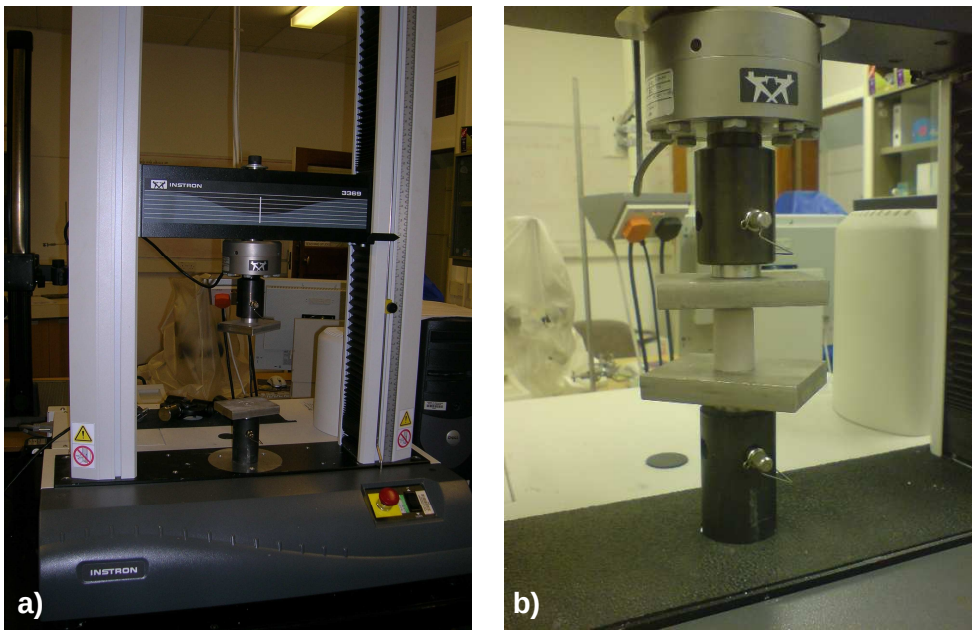

Figure VI-1: Instron tensile tester (Figure VI-1a) and compression stainless steel plates (b) used in the particular experiments are shown with a hydroceramic sample between the stamps.

Compressive strength was measured using a 50 kN load. All the compressive tests were carried out in accordance with the American Society for Testing and Materials (ASTM) C39-96 [20] on samples with an aspect ratio of 2. The sample was loaded at a displacement rate of 0.33 mm min^{-1}. Three samples of each composition were tested to check reproducibility. A typical standard deviation between triplicate specimens for compressive strength measurements was 2.2 MPa. The compressive strength was determined from the applied load at the point of sample failure.

VI- 2.2.2 Permeability

There are several methods of measuring the permeability of cement-based materials [21,22]. The permeability results reported here were obtained using a purpose-built Hassler cell permeameter. This type of cell is widely used in petroleum technology [23] and, more recently, has been used in measurements of the permeability of construction materials [24] and in the extraction of pore solution from cement materials [25]. A schematic diagram of the Hassler cell is shown in Figure VI-2 [26] and a full description of the technique and associated equipment is given be Green *et al.* [27] In brief, the Hassler cell is an axial flow permeameter designed to measure the satiated permeability of cylindrical specimens of ~25mm diameter and between 25 and 75mm in length. Before measurement, the specimen must be saturated with the test liquid, in this case de-ionised water. The specimen is placed inside a nitrile rubber sleeve to which a containing pressure is applied which exceeds the pressure of the liquid flowing through the sample. This containing pressure, which is monitored by a pressure transducer, seals the circumferential face of the sample and ensures axial flow. A constant flow of liquid through the sample is provided by a pulse-free chromatography pump and the pressure necessary to maintain this flow, the fluid pressure, is monitored by a second pressure transducer. Darcian flow through the sample is confirmed by an increase in flow rate resulting in a directly proportional increase in fluid pressure.

Permeability test specimens, 22 mm diameter $\times$ 30 mm length, were vacuum saturated with deionized water before being loaded into the Hassler cell. The containing pressure was maintained at 5 MPa for samples having a compressive strength greater than 10 MPa and at 2.5 MPa for those with a compressive strength less than 10 MPa. The saturated liquid conductivity (or intrinsic permeability), *K*, was calculated from the equation

$$K = \frac{Q * L}{P * A} \qquad \text{(VI-3)}$$

*w*here *Q* is the steady volumetric flow rate through the sample of length *L* and cross-sectional area *A* at inlet gauge pressure *P*. A typical standard deviation between triplicate specimens for permeability measurements was 1.8×10^{-17} m^2.

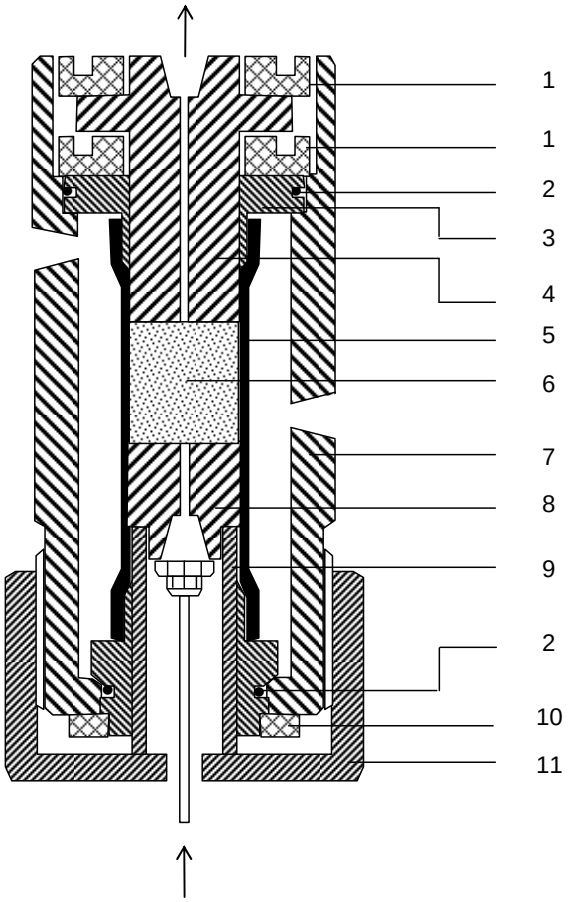

Figure VI-2: Hassler cell permeameter after Hall and Hoff [26]: 1 Retaining ring; 2 nitrile rubber O-ring seal and PTFE back-up ring; 3 sleeve carrier; 4 fixed platen; 5 nitrile rubber sleeve; 6 sample; 7 stainless steel case; 8 movable platen; 9 platen carrier; 10 retaining ring; 11 end cap.

VI- 2.2.3 Scanning Electron Microscopy (SEM)

To image the microstructure of the hydroceramic samples, a scanning electron microscope (SEM) was used with an acceleration voltage of 5 kV. To minimize charging, the samples were sputter-coated with approximately 8 nm of 60 % gold and 40 % palladium. The principles of the SEM have been described in detail in Chapter III.

VI- 2.2.4 Simulation Experiments

The basic goal in computing the permeability of a material is to apply a pressure gradient across the three-dimensional microstructure and compute the resultant flow. NIST has developed and recently distributed a three-dimensional

linear Stokes solver for performing this calculation for a three-dimensional microstructure consisting of pores and solids [28]. A finite difference solution of the linear Stokes equations for slow, incompressible, steady-state flow is utilized to determine the x, y, and z components of the fluid velocity in each porosity voxel. Once this finite difference solution converges sufficiently, the permeability, *k*, of the three-dimensional microstructure is calculated by volume averaging the local fluid velocity (in the direction of the flow) and applying the Darcy equation:

$$u = -\frac{k}{\eta}\frac{\Delta p}{L} \qquad \text{(VI-4)}$$

where *u* is the average fluid velocity in the direction of the flow (x-direction) for the microstructure, η is the fluid viscosity, and *L* is the length of the sample microstructure across which there is an applied pressure difference of Δ*P* [29]. For a given microstructure, three separate runs of the computer codes may be conducted to determine the (different) permeabilities for pressure driven flow in the x, y, and z directions. Obviously, for permeability predictions to be accurate, the three-dimensional microstructure used as input must adequately represent the pores (sizes, connectivity, and tortuosity) that are dominating the flow paths through the material.

VI- 3. Results and discussion

VI- 3.1 Mineralogy

The mineralogy of the CASH hydroceramic system has been described in detail in Chapter II. Here a brief description of the minerals present in these samples will be given, to help the reader with the interpretation of strength and permeability results.

By adding small amounts of silica flour (<20 wt %) to the cement, jaffeite, calcium silicate, kilchoanite, α-dicalcium silicate hydrate and 11Å tobermorite form at 200 ℃. In these samples reinhardbraunsite is prese nt instead of α-dicalcium silicate hydrate at 250 ℃, 300 ℃ and 350 ℃. Increasing th e amount of silica (>40 wt %) resulted in the formation of xonotlite, gyrolite and some relict quartz at 200 ℃ and 250 ℃. At temperatures of 300 ℃ and 350 ℃, trusc ottite is forming instead of

gyrolite. By adding small amounts of alumina, portlandite and jaffeite form together with the hydrogarnet phase. In these samples reinhardbraunsite is also present at 250 ℃ instead of α-dicalcium silicate hydrate which is formed at 200 ℃. As more alumina is added (>20 wt %), jaffeite is the only new phase co-existing with hydrogarnet at 200 ℃ and 250 ℃, together with som e relict corundum. At 300 ℃, calcium alumina hydrate forms in addition to the phases mentioned previously and at 350 ℃, bicchulite is present (Table VI-2).

When adding small amounts of silica and alumina to cement at 200 ℃, kilchoanite and tobermorite form, together with jaffeite, hydrogarnet and corundum. As more silica is added to the system, xonotlite replaces kilchoanite. At 250 ℃, kilchoanite is not present and only jaffeite, hydrogarnet, tobermorite, xonotlite and corundum form depending on the proportions of the starting materials (Table VI-2). The same minerals form at 300 ℃ and 350 ℃, the on ly difference being the absence of tobermorite and the presence of foshagite at 350 ℃ when small amounts of silica and alumina are added. Also truscottite forms instead of gyrolite when adding small amounts of alumina and high amounts of silica flour. As can be seen from Table VI-2, the mineralogy of this system (CASH) is complicated and it is described in more detail elsewhere [7,9,30]. Here, we have focus on the significance of the different minerals on the engineering properties of these materials.

Table VI-2: Phases identified in each sample as estimated by Rietveld refinement. Codes for phases: *a* α-dicalcium silica hydrate; *m* calcium silicate; *g* gyrolite; *b* bicchulite; *c* corundum; *d* calcium alumina hydrate; *f* foshagite; *h* hydrogarnet; *j* jaffeite; *k* kilchoanite; *p* portlandite; *q* quartz; *r* reinhardbraunsite; *t* 11Å tobermorite; *x* xonotlite.

Proportions (wt %)			200 ℃	250 ℃	300 ℃	350 ℃
Dyckerhoff cement	**SiO_2**	**a-Al_2O_3**				
100	0	0	p=8; j=74; a=18	p=5; j=76; r=19	p=14; j=36; r=34; h=16	p=18; j=20; r=47; h=15
90	10	0	j=9; a=6; m=49; k=27; t=9	j=2; r=6; m=84; x=8	j=2; r=11; m=74; x=12	j=10; r=68; f=8; h=14
80	20	0	j=1; m=37; k=10; t=16; x=31	m=82; x=18	m=73; x=27	x=100
70	30	0	t=8; x=92	x=100	x=98; v=2	x=60; v=40
60	40	0	x=36; g=59; q=6	x=18; g=56; v=26	x=35; v=65	x=10; v=90
50	50	0	g=70; q=30	g=64; v=21; q=21	v=88; q=12	v=84; q=16
90	0	10	p=6; j=30; h=64	p=5; j=8; r=7; h=87	p=7; j=17; h=76	p=12; j=6; h=82
80	0	20	j=3; h=97	j=7; h=92	j=6; h=83; d=11	p=1; j=3; h=72; b=4; d=10
70	0	30	j=3; h=80; c=16	j=8; h=75; c=16	j=5; h=67; c=11; d=16	h=56; c=13; b=11; d=20
60	0	40	j=3; h=73; c=30	j=6; h=62; c=32	j=4; h=47; c=31; d=18	h=43; c=29; b=10; d=18
50	0	50	j=2; h=60; c=43	j=5; h=51; c=44	j=3; h=44; c=42; d=11	h=35; c=42; b=8; d=15
80	10	10	j=7; k=26; t=12; h49; c=6	j=11; h=89	j=7; h=93	p=1; j=4; x=18; f=1; h=75
60	10	30	j=1; t=8; h=68; c=23	t=6; h=67; c=27	h= 83; c=19	x=4; h=73; c=20; b=4
60	20	20	t=18; x=36; h=26; c=20	t=7; x=40; h=34; c=19	x=45; h=33; c=21	x=56; h=14; c=30
60	30	10	t=19; x=64; h=5; c=12	x=84; c=16	x=55; v=31; c=13	x=21; v=58; h=6; c=14
50	10	40	t=9; h=54; c=36	t=4; x=10; h=48; c=38	x=3; h=63; c=33	h=65; c=32; b=2
50	40	10	g=83; q=8; c=9	g=64; v=20; q=4; c=12	x=13; v=71; q=2; c=15	x=4; v=76; q=6; c=14

VI- 3.2 Compressive strength

Samples cured at 200 ℃ and 250 ℃ have almost the same engineering properties, as their mineralogy is similar (Table VI-2). The ternary contour plot in Figure VI-3 shows the compressive strength of the samples cured at 200 ℃. The sample compositions are expressed as molar proportions of the 3 major oxides present in the system CaO, SiO_2 and Al_2O_3. When more than 20 wt % of silica only is added to the system at 200 ℃ the strength start s to improve. Xonotlite and 11Å tobermorite are responsible for this improvement as they grow at the expense of α-dicalcium silicate hydrate, which is known for strength retrogression in cement systems [1,4].

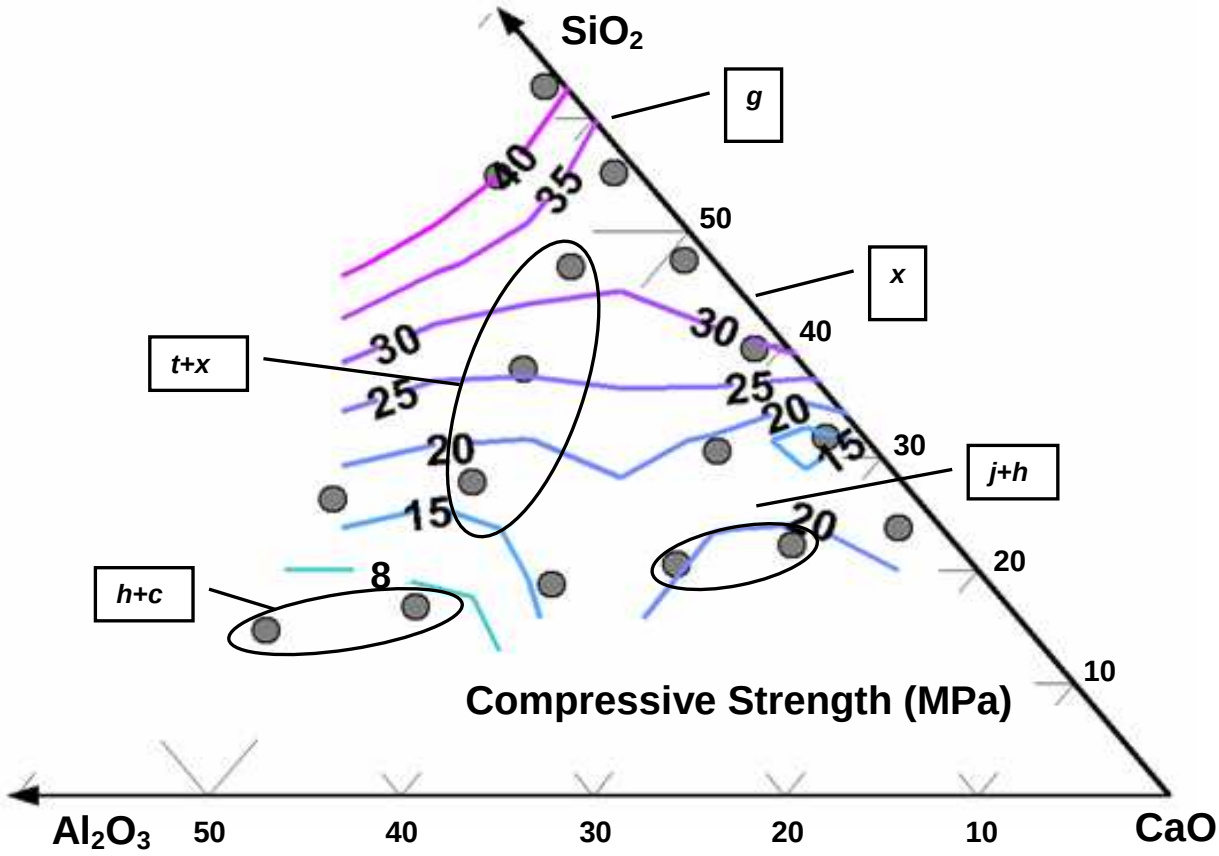

Figure VI-3: Ternary contour plot of compressive strength for samples cured at 200 ℃. Sample points (grey circles) are plotted in molar proportions of CaO, SiO_2 and Al_2O_3. Samples in circles indicate the dominant phases in different regions. Codes for phases are shown in Table VI-2.

Adding more silica causes platey crystals of gyrolite to form Figure VI-4, further improving the strength which attains a maximum value of 42 MPa. These results are in good agreement with Grabowski and Gillott [31] who studied similar cement slurries. On the other hand, the addition of small amounts of alumina (10-15 wt %) to the system only slightly improves the strength.

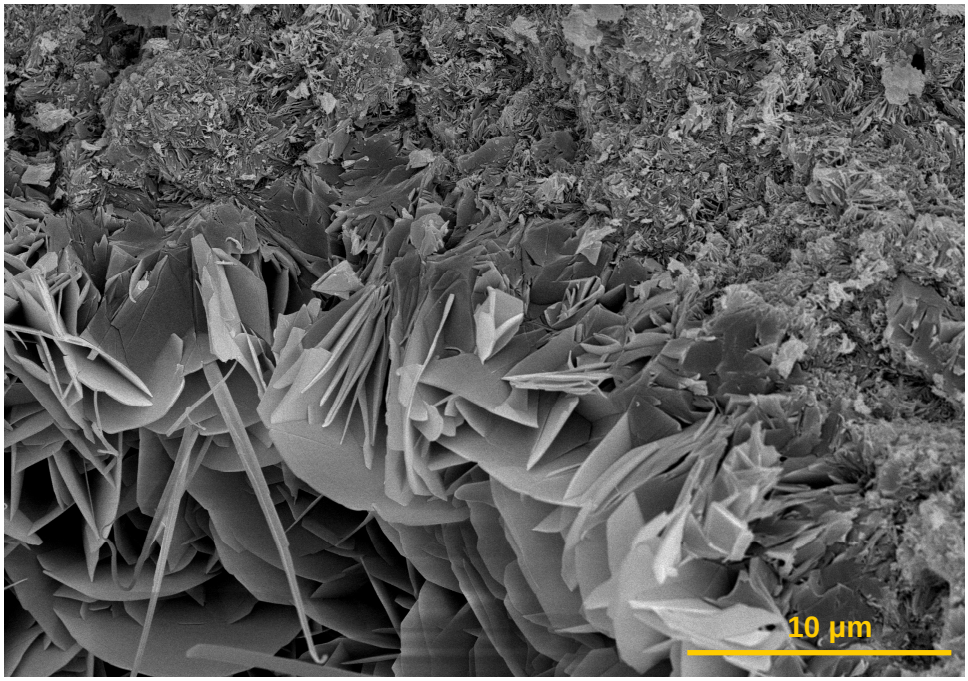

Figure VI-4: SEM image illustrating platey crystals of gyrolite growing in a sample containing 40 wt % of silica flour cured at 200 ℃. The compressive strength of this sample is 39 MPa.

With greater amounts of alumina the strength decreases. Figure VI-5a shows a sample containing 15 wt % of alumina where needle-shaped crystals of jaffeite form between the hydrogarnet crystals filling the pores between them and increasing the compressive strength. Once the amount of jaffeite present is significantly decreased (<20 wt %, Table VI-2) hydrogarnet and relict corundum are dominant and the strength is significantly decreased because of increased porosity Figure VI-5b. Kalousek [18] also reported that large amounts of hydrogarnet in these systems decrease strength, although his values are higher than those reported here, perhaps due to different mixing compositions and the different curing time used. When both silica and alumina are added at these temperatures, tobermorite forms in addition to hydrogarnet (Table VI-2). Tobermorite is known to improve and stabilize

strength in cement-based systems [11,15]; therefore the samples containing this mineral in significant amounts exhibit increased compressive strength as shown in Figure VI-3.

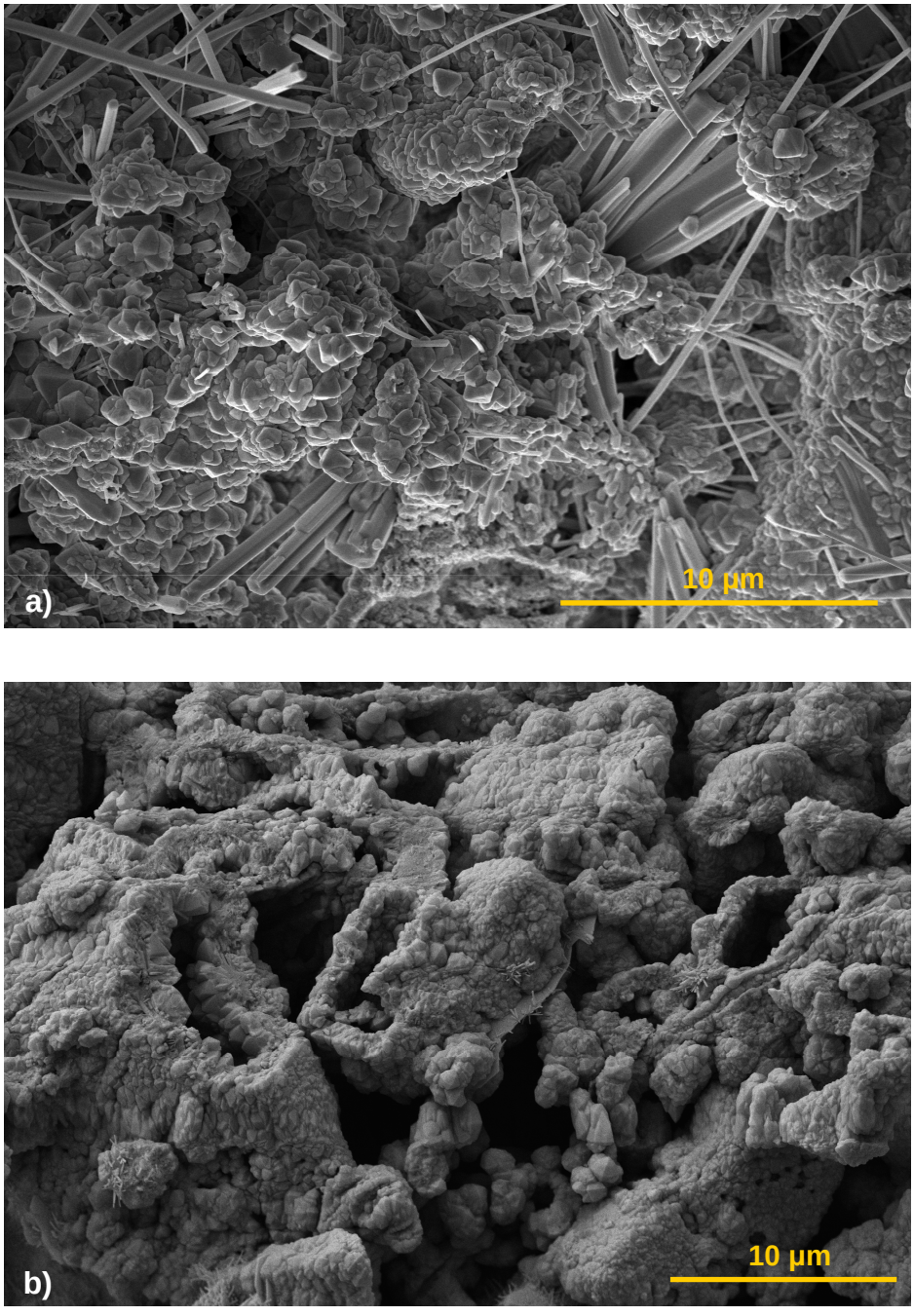

Figure VI-5: a) SEM image showing needle shaped jaffeite crystals growing in the pores between hydrogarnet crystals in sample containing 10 wt % of alumina and cured at 200 ℃. Compressive strength 2 0 MPa. b) SEM image of sample cured at 200 ℃ and containing 40 wt % of al umina where only hydrogarnet crystals are present. Compressive strength 8 MPa.

The mineralogy of the samples cured at 300 ℃ is similar to those cured at 350 ℃, and their engineering properties were also similar in terms of compressive strength. Figure VI-6 illustrates a ternary contour plot of samples cured at 350 ℃. When adding more than 25 wt % of silica, the compressive strength is increased as xonotlite forms instead of reinhardbraunsite and calcium silicate.

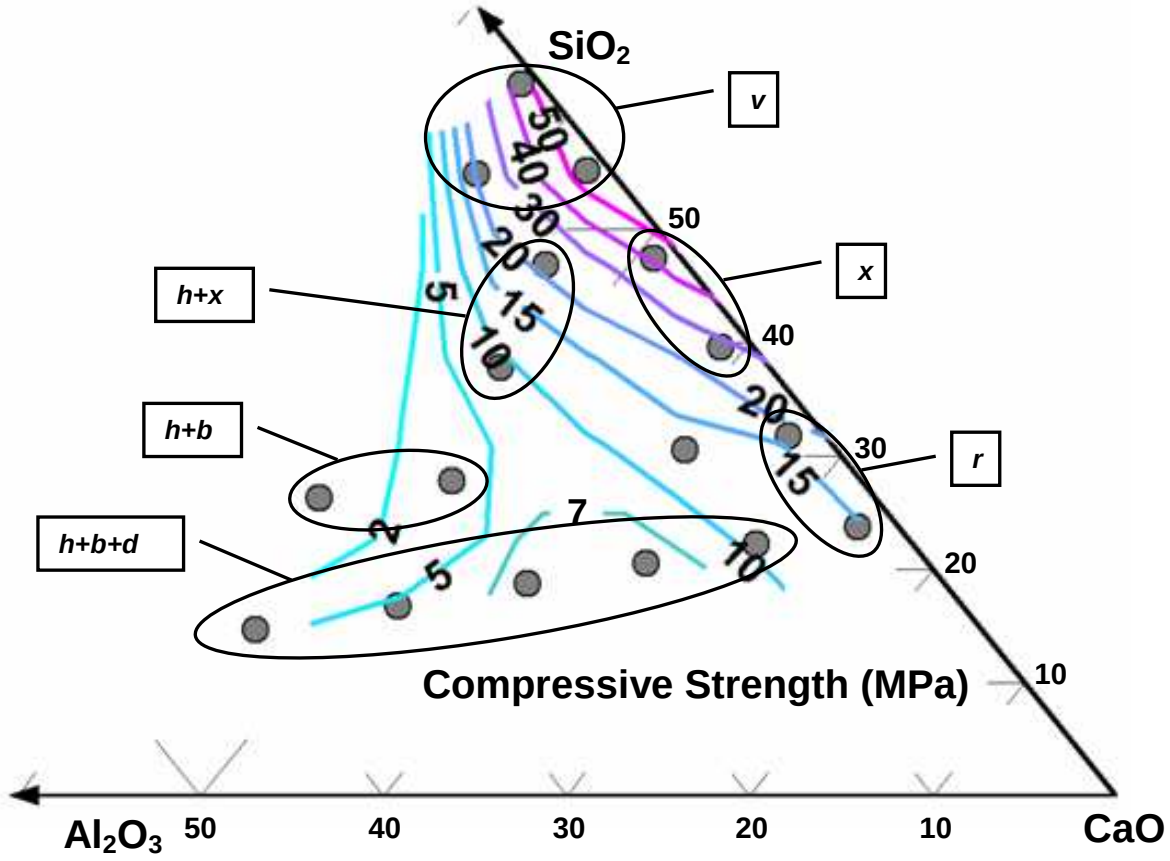

Figure VI-6: Ternary contour plot of compressive strength for samples cured at 350 ℃. Sample points (grey circles) are plotted in molar proportions of CaO, SiO_2 and Al_2O_3. Samples in circles indicate the dominant phases in different regions. Codes for phases are shown in Table VI-2.

As more silica is added, hexagonal crystal plates of truscottite form Figure VI-7 increasing strength further to a maximum of 52 MPa. Our results show that samples containing truscottite are stronger than those containing xonotlite, in disagreement with the results of Eilers *et al.* [32]. On comparing the maximum compressive strength values for samples cured at 200 ℃ and 350 ℃, an increase in strength of approximately 25 % is observed as the temperature is increased. This

suggests that truscottite, which is formed at higher temperatures (350 ℃), is stronger than gyrolite which forms at lower temperatures (Table VI-2).

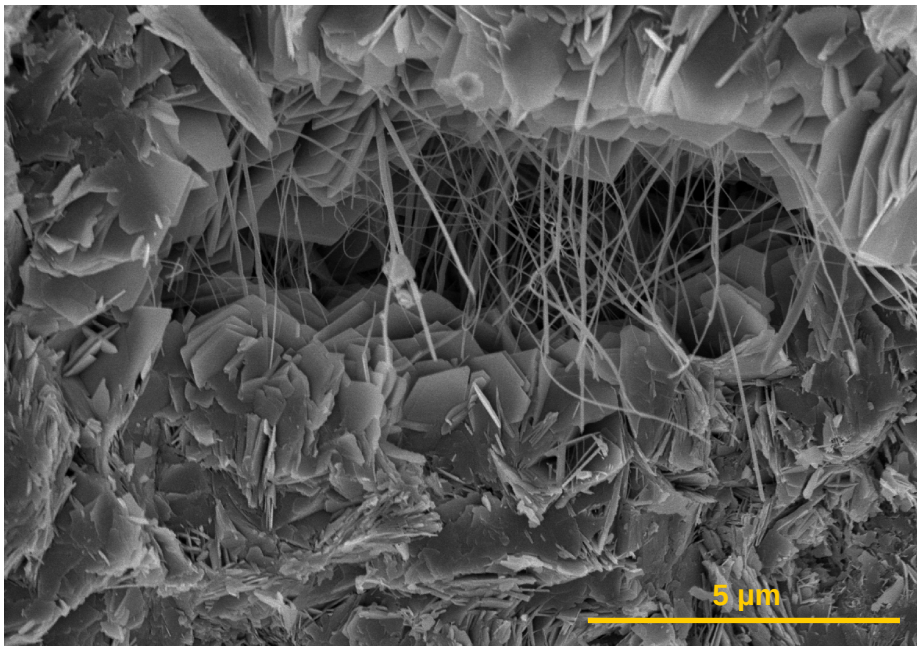

Figure VI-7: SEM image showing hexagonal crystals of truscottite, the small needles that are present are of xonotlite. Sample cured at 350 ℃ containing 40 wt % silica flour.

On the other hand, as the amount of alumina in the mix is increased, the compressive strength progressively decreases to a lowest value of 2 MPa. Apart from hydrogarnets, the formation of two new minerals at these temperatures, calcium alumina silicate hydrate and bicchulite, are responsible for the strength deterioration. Only with both high amounts of silica and low amounts of alumina is the strength increased, since such compositions favor the formation of truscottite. The remaining compositions examined at 300 ℃ and 3 50 ℃ have low strength due to the absence of 11Å tobermorite.

According to the American Petroleum Institute (API) specifications, the minimum compressive strength required by these materials for use as sealants for very deep oil or geothermal wells is 7 MPa [19]. The hydroceramic samples that meet this criterion are those that contain in large amounts minerals with a Ca/Si ratio of 1 or lower, such as xonotlite, gyrolite, 11Å tobermorite and truscottite.

VI- 3.3 Permeability

The ternary contour plot shown in Figure VI-8 illustrates the permeability of the samples cured at 200 ℃. The pattern of behavio ur is similar to the compressive strength measurements at the same temperature. When silica flour only is added, the permeability is decreased, whereas alumina additions have the reverse effect. The reason for this is the variation in mineralogy as explained in the previous section. When both additives are incorporated, samples containing high amounts of tobermorite exhibit low permeability. Our results are in good agreement with Nelson *et al.* [33] and Eilers *et al.*, [32] who studied the engineering properties of similar systems at these temperatures.

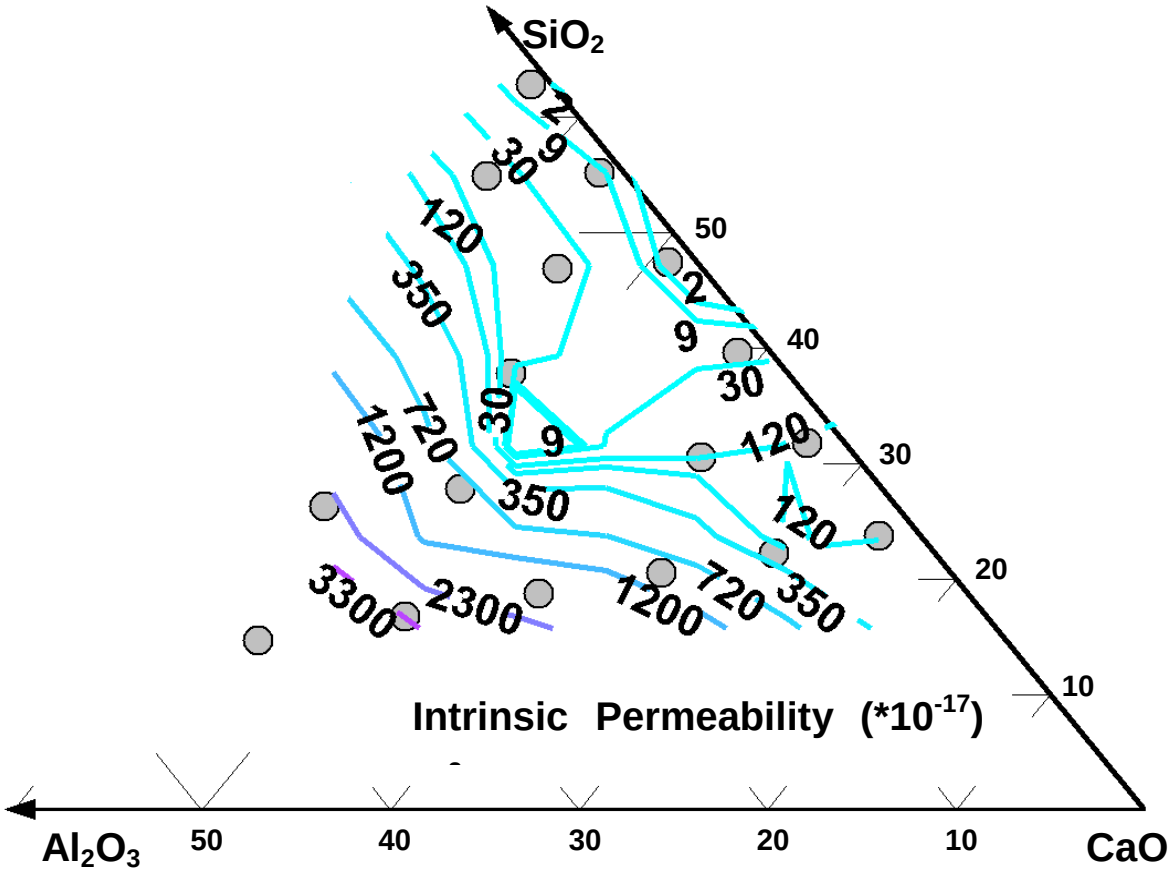

Figure VI-8: Ternary contour plot of intrinsic permeability for samples cured at 200 ℃. Sample points (grey circles) are plotted in molar proportions of CaO, SiO_2 and Al_2O_3.

At higher temperatures (300 ℃ –350 ℃), the permea bility behaviour in samples containing alumina is different. When adding more than 20 wt % of alumina, the permeability values decrease, as shown in Figure VI-9, despite the fact that hydrogarnet is present (Table VI-2).

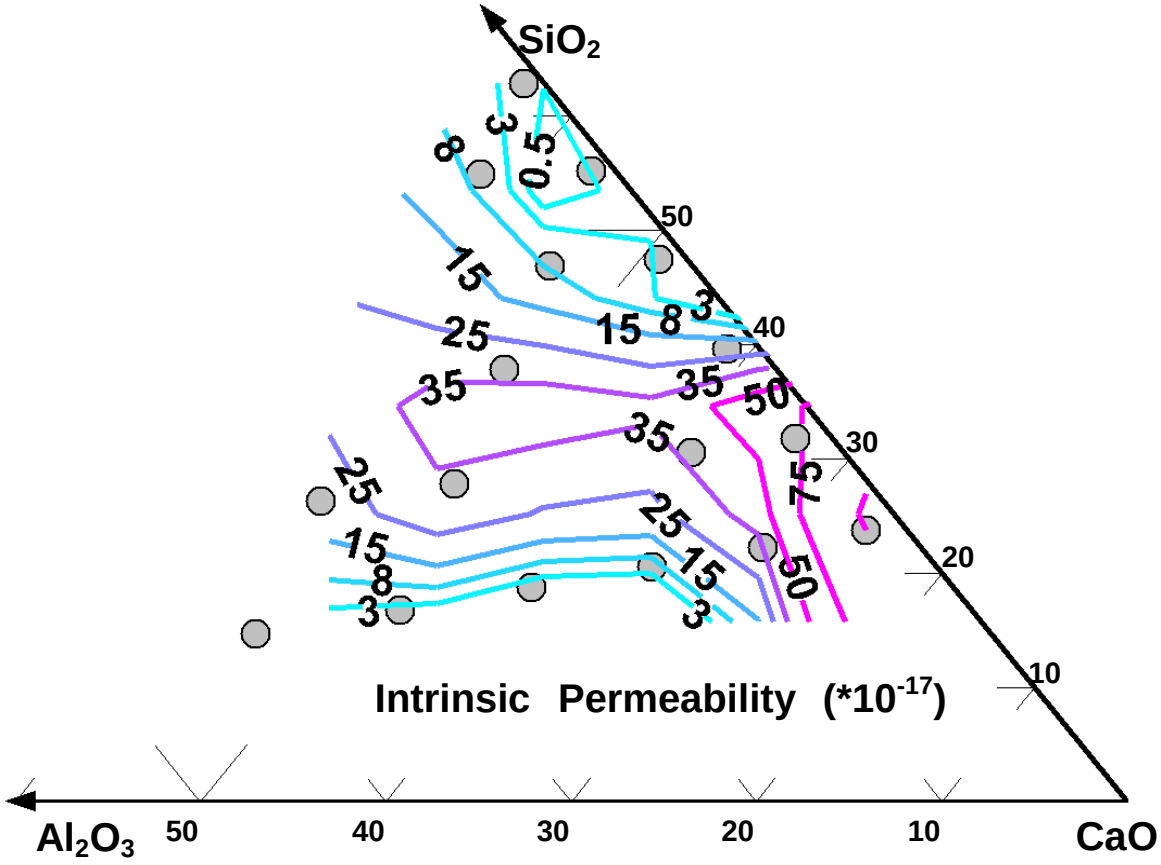

Figure VI-9: Ternary contour plot of intrinsic permeability for samples cured at 350 ℃. Sample points (grey circles) are plotted in molar proportions of CaO, SiO_2 and Al_2O_3.

The formation of the two new minerals, calcium aluminum silicate hydrate and bicchulite (Table VI-2), which are present in these samples along with hydrogarnets, are responsible for this. Calcium aluminum silicate hydrate forms platey crystals growing between the hydrogarnet aggregates as shown in Figure VI-10, preventing the liquid from moving through the sample, thereby reducing the permeability values. These values meet the API specifications for use as sealants for very deep oil or geothermal wells.

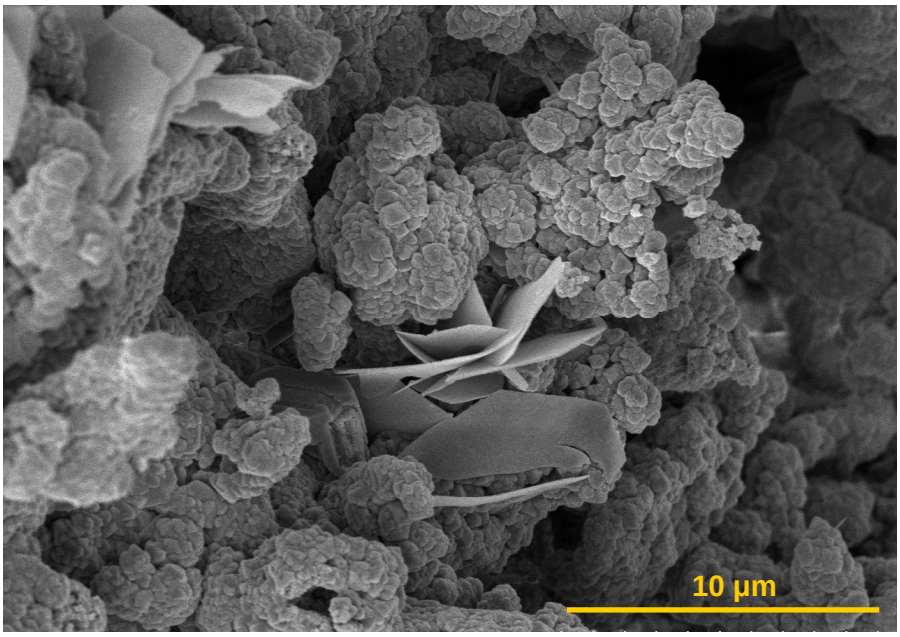

Figure VI-10: SEM image illustrating platey crystals of calcium aluminum silicate hydrate growing between hydrogarnet particles in sample containing 30 wt% of alumina cured at 300 ℃.

Adding silica flour, the permeability values decrease progressively (Figure VI-9). Instead of reinhardbraunsite and calcium silicate, xonotlite and truscottite form. Once truscottite is formed (>40 wt % of silica), the values of permeability are the lowest observed in our CASH system. Comparing truscottite with other minerals such as gyrolite, xonotlite or 11Å Tobermorite, a general improvement of the engineering properties of the hydroceramic materials is observed. Our experiments showed that truscottite is very stable in closed systems, although it is believed that it may be difficult to produce and to maintain in a geothermal environment [34].

When adding both silica and alumina to the samples, a decrease in permeability is observed when truscottite is formed in large amounts (Table VI-2). Although when calcium aluminum silicate hydrate or xonotlite is formed, and depending on the composition of the starting materials, permeability decreases compared to neat cement. In general, the permeability behavior of the system at 300 ℃ and 350 ℃ is improved compared to those at lowe r temperatures. The combination of phases with different crystal shapes produces complicated non-connected pore structures, hence forming a barrier to liquid penetration.

VI- 3.4 Permeability simulation

To simulate permeability, microstructure models closely related to the microstructure of real hydroceramic samples have been reconstructed using two-dimensional SEM images of the real samples. An example of a 3-D model microstructure generated from a 2-D image is given in Figure VI-11. The SEM image of a sample cured at 350 ℃ with 40 wt % addition of silica flour in Figure VI-11a shows hexagonal truscottite crystals and xonotlite needles. This image has been used as the binary image, after segmentation (Figure VI-11b), to extract the correlation functions to reconstruct the 3-D microstructure. The final 3-D microstructure generated (Figure VI-11c) consists of a three-dimensional grid (lattice) in which each site is defined to be either solid (white) or pore (black). In our study, the lattices were always 100 x 100 x 100 units for a total of one million sites (voxels) with voxel dimensions ranging from 0.25 μm to 1.95 μm, depending on the specific microstructure being simulated. Porosities for the reconstructed microstructures were set to match those of the physical specimens, which ranged between 25 % and 40 % for the materials examined in this study. The method used to reconstruct a 3-D porous medium from a 2-D image is fully described by Bentz and Martys elsewhere [35]. One assumption of the 3-D reconstruction technique is that the pore structure of the real (and reconstructed) microstructure is isotropic [35]. While the individual crystals comprising the solid phases in these microstructures may be highly anisotropic (as seen in Figure VI-11a), the pore space between them can still be isotropic as indicated by the black regions in the binary image in Figure VI-11b. The reconstruction algorithm generates 3-D porous microstructures with a percolation threshold (equivalent to zero permeability) near 10 % porosity [35], well below the porosity values examined in this study.

Using this 3-D model, the permeability is then calculated using a linear Stokes solver [28,29]. The permeability computer program applies pressure in one of the three principal directions of the 3-D microstructure and computes the resulting velocity vector field within the porosity. The Darcy equation [29] is then used to calculate the equivalent permeability for the microstructure. The permeability codes, Permsolver, have been validated previously by computing the permeabilities of both circular and square tubes [28]. For a square tube 25 voxels on one side, the error between computed and theoretical permeabilities was only 0.01 %, whereas for a circular tube with a diameter of 25 voxels it was less than 2 %. The codes, together with a user's manual, are available for download at

ftp://ftp.nist.gov/pub/BFRL/bentz/permsolver. This method has been used previously [36], for pervious concrete for example, but according to my knowledge this study is the first time that it has been used to compute permeability for hydrothermal and oilwell cement systems. Similar approaches can be applied to compute other properties, such as electrical conductivity or ionic diffusion, of the 3-D reconstructed microstructures [35,36].

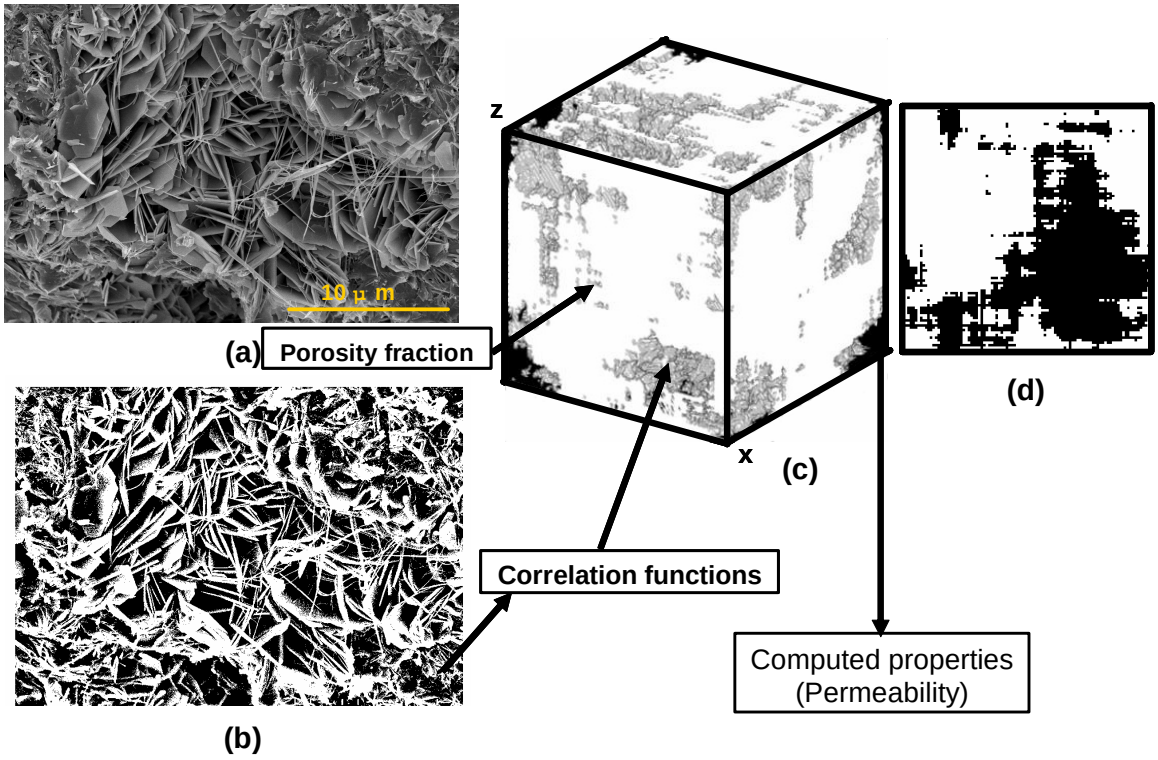

Figure VI-11: Illustration of the process of creating a three-dimensional microstructure for subsequent computation of permeability. **a)** SEM image showing hexagonal crystals of truscottite. The needle shaped crystals are of xonotlite. Sample cured at 350 ℃ containing 40 wt% of silica flour. **b)** Binary image used to extract the correlation functions for the 3-D reconstruction. **c)** Reconstructed three-dimensional microstructure (100 x 100 x 100 pixels) of which permeability is computed. **d)** Slice of the reconstructed three dimensional microstructure.

The permeabilities of samples cured at 200 ℃ and 3 50 ℃ with silica or alumina additions have been computed. The results in Figs. 11 and 12 show that the experimental and simulation values are in excellent agreement. Therefore, the first conclusion is that the 3-D models used to compute permeability represent well the

characteristics of the real microstructures which control liquid transport. All the results present in Figures VI-12 and 13 are simulation values of permeabilities calculated on the *x* direction of the model. In a few samples, the permeability has been computed in the other two directions (*y* and *z*) and the results are very similar, suggesting that both the 3-D model and the real microstructure are isotropic.

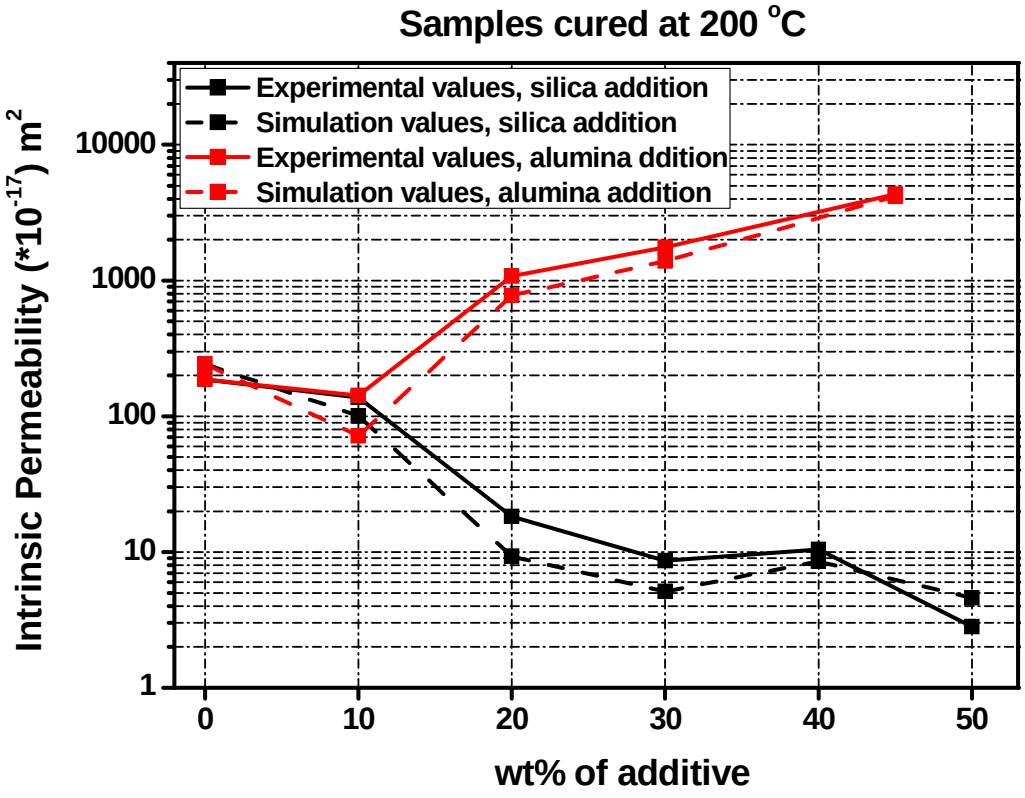

Figure VI-12: Comparison of experimental and simulation values of intrinsic permeability with silica or alumina additions in samples cured at 200 ℃.

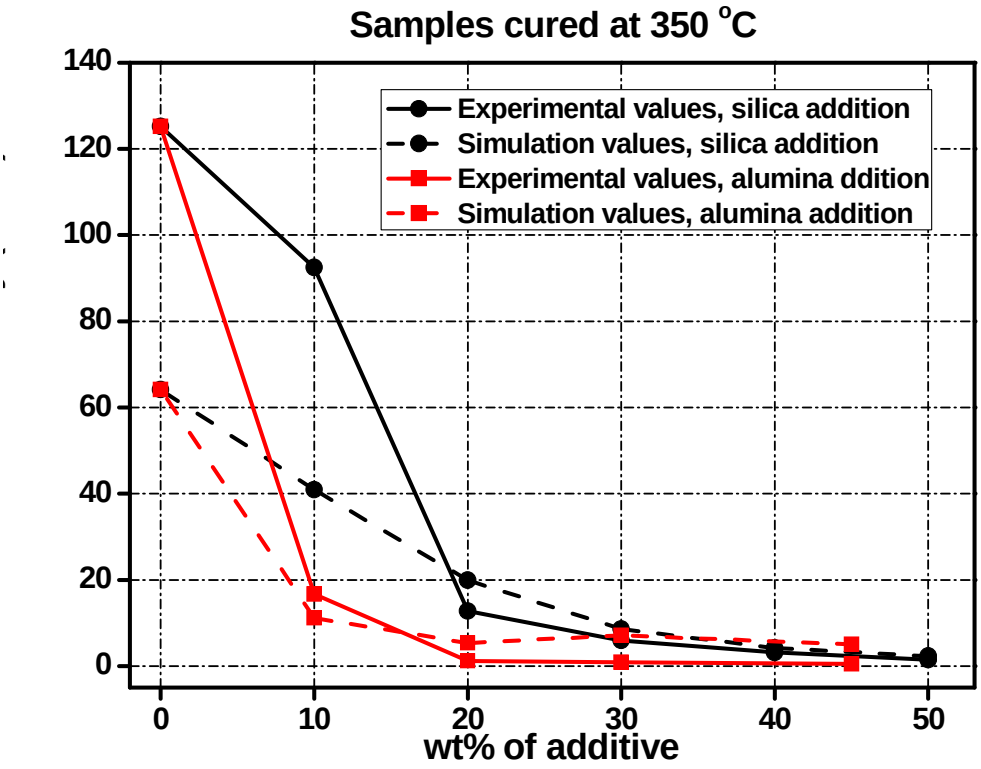

Figure VI-13: Comparison of experimental and simulation values of intrinsic permeability with silica or alumina additions in samples cured at 350 ℃.

VI- 4. Conclusions

In this chapter, the engineering properties of hydroceramic materials cured at 200 ℃ to 350 ℃ have been discussed. In additio n the relationship of these properties with microstructure and the evolution of various minerals have also been examined. Finally, computed permeabilities have been compared with experimental results. The main conclusions are summarized as follows:

By adding more than 20 wt % of silica flour, the engineering properties of the hydroceramics are improved due to the formation of xonotlite, gyrolite or truscottite. The property values of these materials are within the API specifications for very deep oil or geothermal well sealants.

Adding more than 20 wt % of alumina at 200 ℃ and 2 50 ℃, results in the formation of hydrogarnets which decrease the engineering properties of the hydroceramics as they create highly porous microstructures.

At 300 ℃ and 350 ℃ when adding alumina, calcium a luminum silicate hydrate and bicchulite grow between the hydrogarnet aggregates, improving permeability, with values lying within the acceptable limits of the API specification. On the other hand, the compressive strength values of these materials are very low and outside of the API specification.

Adding both silica and alumina to the system, results in samples that contain high amounts of xonotlite, gyrolite, 11Å tobermorite or truscottite which have improved engineering properties.

The simulation values of permeability are in good agreement with the experiments, demonstrating the potential of a computational image-based approach as an alternative to time-consuming experimental measurements of permeability.

VI- 5. References

1. E. B. Nelson, "Thermal Cements", pp. 9/1-9/19 in *Well Cementing***.** Edited by E. B. Nelson. Schlumberger Educational Services, Sugar Land, Texas, 1990.

2. A. J. Philippacopoulos and M. L. Berndt, "Structural analysis of geothermal well cements," *Geothermics,* **31** [6] 657-676 (2002).

3. R. A. Kennerly, "Products of hydrothermal hydration of cements from geothermal bores," *New Zealand Journal of Science,* **4** 453-468 (1961).

4. H. F. W. Taylor,"*Cement Chemistry*" 2nd. London, Thomas Telford Publishing, 1997.

5. R. Oberste-Padtberg, "Degradation of cements by magnesium brines"; in *Proceedings of the 7th International Conference on Cement Microscopy*. Edited by J. Bayles, G. R. Gouda, andA. Nisperos. Duncansville, TX, 1985.

6. T. Sugama, L. E. Brothers, and T. R. Van de Putte, "Air-foamed calcium aluminate phosphate cement for geothermal wells," *Cement and Concrete Composites,* **27** [7-8] 758-768 (2005).

7. N. Meller, C. Hall, and J. Phipps, "A new phase diagram for the CaO-Al_2O_3-SiO_2-H_2O hydroceramic system at 200 °C," *Materials Research Bulletin,* **40** 715-723 (2005).

8. N. Meller and C. Hall, "Hydroceramic sealants for geothermal wells"; pp.281-284 in *Proceedings of the International Congress on Applied Mineralogy*. Edited by M. Pecchio, F. R. D. Andrade, L. Z. D. D'Agostino, H. Kahn, L. M. Sant'Agostigno, andM. M. M. L. Tassinari. Brazil, 2004.

9. N. Meller, C. Hall, K. Kyritsis, and G. Giriat, "Synthesis of cement based CaO-Al_2O_3-SiO_2-H_2O (CASH) hydroceramics at 200 and 250 ℃: Ex-situ a nd in-situ diffraction " *Cement and Concrete Research,* **37** 823-833 (2007).

10. N. Meller, K. Kyritsis, and C. Hall, "The mineralogy of the CaO-Al_2O_3-SiO_2-H_2O (CASH) system from 200 to 350 ℃," *Cement and Concrete Research*, (accepted).

11. L. D. Sanders and W. J. Smothers, "Effect of tobermorite on the mechanical strength of autoclaves Portland cement-silica mixtures," *Journal of the American Concrete Institute,* **28** 127-134 (1957).

12. E. Grabowski and J. E. Gillott, "Modifications of engineering behaviour of thermal cement blends containing silica fume and silica flour by replacing flour with silica sand," *Cement and Concrete Research,* **19** [4] 499-508 (1989).

13. G. Carter and D. K. Smith, "Properties of cementing compositions at elevated temperatures and pressure," *Transactions of the Metallurgical Society of the American Institute of Metallurgical Engineers,* **213** [2] 20-26 (1958).

14. E. L. White, C. A. Langton, M. W. Grutzeck, and D. M. Roy, "High temperature cements for geothermal applications," *American Ceramic Society Bulletin,* **58** [3] 334 (1979).

15. N. Isu, K. Sasaki, H. Ishida, and T. Mitsuda, "Mechanical property evolution during autoclaving process of aerated concrete using slag. 1. Tobermorite formation and reaction behaviour of slag," *Journal of the American Ceramic Society,* **77** [8] 2088-2092 (1994).

16. M. L. Berndt and C. E. Mancini, "Tensile tests on plain and fibre reinforced geothermal cements," *Journal of Materials Science,* **39** [5] 1727-1733 (2004).

17. J. B. Odelson, E. A. Kerr, and W. Vichit-Vadakan, "Young's modulus of cement paste at elevated temperatures," *Cement and Concrete Research,* **37** [2] 258-263 (2007).

18. G. L. Kalousek and S. L. Chow, "Research on cements for geothermal and deep oil wells," *Society of Petroleum Engineers Journal,* **16** [6] 307-309 (1976).

19. API Specification 10. *Specification for materials and testing for well cements*. American Petroleum Institute. Washington, D.C., 1982.

20. ASTM Annual Book of Standards C39. 0*4 02. Compressive strength of cylindrical concrete specimens*. American Society for Testing and Materials, Philadelphia, 1999.

21. G. W. Scherer, "Measuring Permeability of Rigid Materials by a Beam-Bending Method: I, Theory," *Journal of the American Ceramic Society,* **83** [9] 1612-1613 (2000).

22. G. W. Scherer, J. J. I. Valenza, and G. Simmons, "New Methods to Measure Liquid Permeability in Porous Materials," *Cement and Concrete Composites,* **37** [3] 386-397 (2007).

23. API Specification 10. *Recommended practices for core analysis*. American Petroleum Institute, Dallas, 1998.

24. M. Sosoro, D. W. Hoff, and M. A. Wilson, "Penetration and Permeability of concrete: barriers to organic and contaminating liquids", pp. 187-212 in *Testing Methods***.** Edited by H. W. Reinhardt. Spon, London, 1997.

25. L. J. Buckley, M. A. Carter, M. A. Wilson, and J. D. Scantlebury, "Methods of obtaining pore solution from cement pastes and mortars for chloride analysis," *Cement and Concrete Research,* **37** [11] 1544-1550 (2007).

26. C. Hall and W. D. Hoff,"*Water transport in brick, stone and concrete*" London, Spon Press, 2002.

27. K. M. Green, W. D. Hoff, M. A. Carter, M. A. Wilson, and J. P. Hyatt "A high pressure permeameter for the measurement of liquid conductivity of porous construction materials," *Review of Scientific Instruments,* **70** [8] 3397-3401 (1999).

28. D. P. Bentz and N. S. Martys, "A Stokes Permeability Solver for Three-Dimensional Porous Media," *NISTIR 7416,* U.S. Department of Commerce, 2007

29. N. S. Martys, S. Torquato, and D. P. Bentz, "Universal scaling of fluid permeability for sphere packings," *Physical Review E,* **50** [1] 403-408 (1994).

30. N. Meller, K. Kyritsis, and C. Hall, "The mineralogy of the CaO-Al_2O_3-SiO_2-H_2O (CASH) system from 200 to 350 ℃," *Cement and Concrete Research,* (in prep).

31. E. Grabowski and J. E. Gillott, "Effect of replacement of silica flour with silica fume on engineering properties of oilwell cements at normal and elevated temperatures and pressures," *Cement and Concrete Research,* **19** [3] 333-344 (1989).

32. L. H. Eilers, E. B. Nelson, and L. K. Moran, "High-temperature cement compositions: pectolite, scawtite, truscottite or xonotlite: which do you want?," *Journal of Petroleum Technology,* **35** [8] 1373-1377 (1983).

33. E. Nelson and L. H. Eilers, "Cementing steamflood and fireflood wells-slurry design," *Journal of Canadian Petroleum Technology,* **25** [5] 58-63 (1985).

34. K. Luke, H. F. W. Taylor, and G. L. Kalousek, "Geothermal well cements formation of truscottite, xonotlite and scawtite " *American Ceramic Society Bulletin,* **58** [3] 334 (1979).

35. D. P. Bentz and N. S. Martys, "Hydraulic radius and transport in reconstructed model three-dimensional porous media," *Transport in Porous Media,* **17** [3] 221-238 (1994).

36. D. P. Bentz, "Virtual pervious concrete: microstructure, percolation, and permeability," *ACI Materials Journal,* **105** [3] 297-301 (2008).

CHAPTER VII

DURABILITY OF HYDROCERAMICS

VII- 1. Introduction

It has been noted in the introductory chapter that cement based well sealants needs to perform under severe chemical conditions because of the presence of different geothermal fluids. This small chapter will discuss some preliminary results on the durability studies carried out on different hydroceramic formulations at temperatures between 200 to 300 ℃.

VII- 2. Experimental procedures

VII- 2.1 Sample preparation

Different hydroceramic formulations (Table VII-1) have been tested for durability under simulated well conditions. The samples were prepared following the same procedure described in Chapter II and pre-cured at 200 ℃ for five days. Once the samples were prepared they were cut into three pieces with approximate dimensions of 6 mm height, 8 mm width and 23 mm length. Each piece was immersed into a different brine and cured for 30 days at the pre-cured temperature. The same experimental method was used for samples cured at 250 and 300 ℃.

Table VII-1: Proportions of starting materials in samples made for durability tests. Samples cured at 200, 250 and 300 ℃.

Proportions (wt %)		
Dyckerhoff cement	**Silica flour HPF6**	**α-Alumina**
100	-	-
90	10	-
70	30	-
60	40	-
70	-	30
60	20	20
60	30	10

VII- 2.1.1 Selection and preparation of brines

Different brine compositions occur in different parts of the earth [1]. In this study three different brines were used. The chemistry of these brines was close to the chemistry of three different geothermal fluids present in well environments [1,2]. The first brine was a sodium sulphate solution (1.69 M, Na_2SO_4) with pH=7.48. The second brine was a hydrochloric acid solution (0.01 M, HCl) with pH=2.21. The last brine used was a sodium carbonate solution (2 M, $NaCO_3$) with pH=11.46.

VII- 2.2 Experimental techniques

In order to map and determine the alteration in mineralogy of these samples tomographic energy-dispersive diffraction imaging (TEDDI) has been used. All the experiments have been carried out in Synchrotron Radiation Source (SRS) at Daresbury laboratories.

VII- 2.2.1 Synchrotron and tomographic energy-dispersive diffraction imaging (TEDDI)

It is a fundamental principle of physics that when charged particles are accelerated they emit electromagnetic radiation [3]. A synchrotron is a circular particle accelerator that boosts the velocity of electrons, protons or ionized atoms very close to the speed of light (e.g. ~0.9999 of the speed of light at 2GeV). Synchrotron produces a wide range of electromagnetic radiation. However, it is often constructed so that the stronger emission consists of X-rays. In synchrotron facilities this energy can be used for a number of experimental purposes.

Particle acceleration is caused by variable frequency of electric field coupled with a variable magnetic field. Adjustments of these parameters secure a constant path of the particles during acceleration. This allows the vacuum container for the particles to be a ring. The shape also allows and requires the use of magnet devices (such as bending magnet, multipole wiggler or undulator) to bend the particle beam.

X-rays produced from synchrotron have several advantages the over those from conventional sealed X-ray tubes [3]. The X-ray beam is much more intense, therefore data can be collected from samples of much smaller volumes in a much shorter time. Despite the continuing success of conventional diffractometers, the higher intensity patterns obtain with synchrotron radiation can be used to resolve more difficult space group or symmetry problems, or can more easily identify minor phases present in the samples [4,5]. Another advantage of synchrotron radiation is

the continuum wavelength produced from infrared to hard X-ray. Hence the appropriate wavelength for a particular experiment can be chosen so that a wider range of d-spacing can be detected. Problems related to fluorescence and absorption are eliminated. Due to these advantages the need for development of specialized techniques such as tomographic energy dispersive X-ray diffraction imaging has been necessary.

Tomographic energy-dispersive diffraction imaging (TEDDI) has been invented by Hall *et al.* [6-8] and applied to various cementitious systems [3]. TEDDI has been developed from energy-dispersive diffraction, a technique which has already found wide applications in the field of time-resolved in-situ diffraction studies of materials such as catalysts and zeolites [9,10], ceramics [11], and cements [12,13].

Energy dispersive diffraction (EDD) was first demonstrated by Geissen [14] in 1968. The EDD is based on Bragg equation:

$$n\lambda = 2d\sin\theta \qquad \text{(VII-1)}$$

where the wavelength, λ is variable and the angle of diffraction relative to the crystalline surface, θ, is fixed (but it is adjustable). The factor 2 is the result of the diffracted radiation passing successfully twice across the space between adjacent planes in the crystal. The letter n is an integer and d is the atomic spacing. Information regarding the atomic spacing is obtained by measuring the energies of diffracted photons. Energy, E, relates to wavelength λ by h, Planck's constant and c, by:

$$E = \frac{hc}{\lambda} = \frac{12.3986}{\lambda}\text{keV} \qquad \text{(VII-2)}$$

Combining Eq. VII-1 and VII-2 the energy-dispersive relation is obtained:

$$Ed\sin\theta = \frac{hc}{2} = 6.1992\text{keV} \qquad \text{(VII-3)}$$

An energy discriminating detector located at a fixed angle determines and counts the energies of the diffracted photons. The diffraction spectrum from each

detector consists of 4000 energy channels, with the channel width being approximately 0.03 keV.

There is a linear relationship between data collection channel numbers and photon energy. This relationship is given by a quadratic equation described by the energy calibration: $E = ax + b$, where x is the channel number and a and b are the calibration coefficients obtained from characteristic fluorescence lines from various elements.

VII- 2.2.2 Station 16.4

Synchrotron tomographic energy-dispersive diffraction imaging (TEDDI) experiments were carried out on beam line 16.4 at the Synchrotron Radiation Source at Daresbury Laboratories, UK. The Synchrotron Radiation Source (SRS) at Daresbury is a low emittance storage ring which operates with an electron beam energy of 2 GeV and stored beam currents in excess of 200 mA [15]. Station 16.4 receives hard X-rays from a superconducting wiggler magnet positioned in straight 16 of the ring. The wiggler magnet is a three-pole device with an on-axis peak filed of 6 T and return fields about 1.2 T [15]. The X-rays travel from the synchrotron to the hutch along an evacuated beam pipe. The beam pipe ends inside the hutch with a water-cooled, 0.1 mm thick aluminium window, which is connected to the station front end by flexible bellows.

A detailed description of the experimental enclosure is given by Clark [15]. The incident X-ray beam is shaped by a circular pinhole to 0.50 mm diameter, and then the diffracted X-rays reach the detector at fixed angles through flat plate collimators (Figure VII-1a). The energy-dispersive method is a fixed geometry technique, with the incident and diffracted X-ray beam defined by the collimator system. The diffracted signal comes from a precise region called a *lozenge*. This region can be adjusted from approximately 1 mm^3 to 10,000 μm^3 by manipulation of the X-ray beam slits, collimation system and diffraction angle, this is a distinguishing feature of TEDII from other techniques. The novelty with TEDDI is that the diffraction-lozenge can be arranged so that it is scanned through the specimen collecting EDD patterns at each point. The scanning procedure is performed by moving mechanically the specimen through the stationary synchrotron white X-ray beam, the scanning being either one, two or three dimensional in nature (Figure VII-1a). Three energy-dispersive detectors were used which allows simultaneous data acquisition at three 2θ angles and it covers a greater range of reciprocal space (*d* -

spacing). The detector unit consists of three germanium crystals and it is placed behind a thick beryllium window.

In this study the samples were stacked on the sample holder and placed on the stationary (Figure VII-1b). The sample holder could be adjusted, using the screws at the edges, depending on the amount of the samples measured each time. The samples were separated using square aluminium plates with dimensions 25x25 mm and scanned along the *x*-axis with 1 mm intervals.

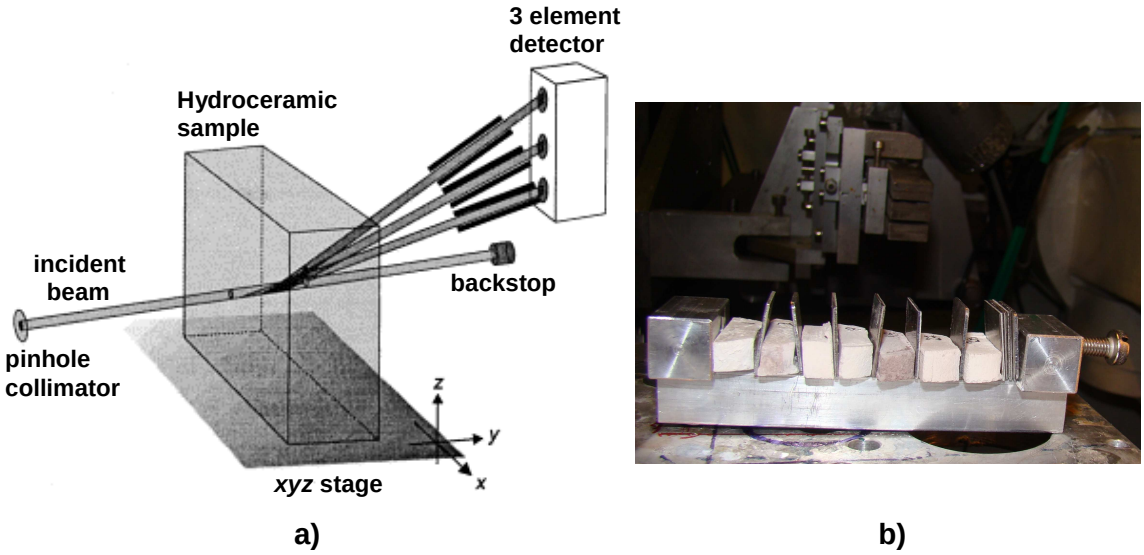

Figure VII-1: a) Image illustrating the TEDDI configuration in relation to the three energy-dispersive detectors and the hydroceramic sample under study. The incident beam defines three diffraction lozenges which are then aligned into coincidence. After Hall *et al.* [8]. **b)** Samples stacked on sample holder. The aluminium sheets are placed to separate them. At the back it is observed the 3 element detector.

VII- 3. Results and discussion

The amount of data collected from Daresbury was enormous and only a small part of the data has been analyzed for this chapter. Sample containing neat cement only and cured at 200 ℃ for 30 days into so dium sulphate brine and a sample containing 30 wt % of silica flour cured at the same brine and temperature will be discussed.

The mineralogy of the sample, containing neat cement only, prior to the brine attack consisted of jaffeite, α-dicalcium silicate hydrate, portlandite and a small amount of calcite (Chapter II). In Figure VII-2 are shown the diffraction patterns of this sample after brine attack which is scanned along the *x*-axis with 1 mm interval. The blue pattern corresponds to the first scan collected at the edge of the sample. The following pattern (green) corresponds to the second scan collected from the same sample but at a different position (1 mm to the left) etc. It is clear that the mineralogy has changed throughout the whole sample. A new mineral is formed, called cesanite ($Na_7Ca_3(SO_4)_6(OH)\bullet 0.8(H_2O)$), instead of portlandite. Sulphate mineral cesanite is reported to form under hydrothermal conditions, when mixtures of Na_2SO_4, Ca_2SO_4 and $Ca(OH)_2$ are heated at temperatures between 200 to 390 ℃ [16]. These conditions are favourable when curing cement only in the specific brine, hence the presence of cesanite.

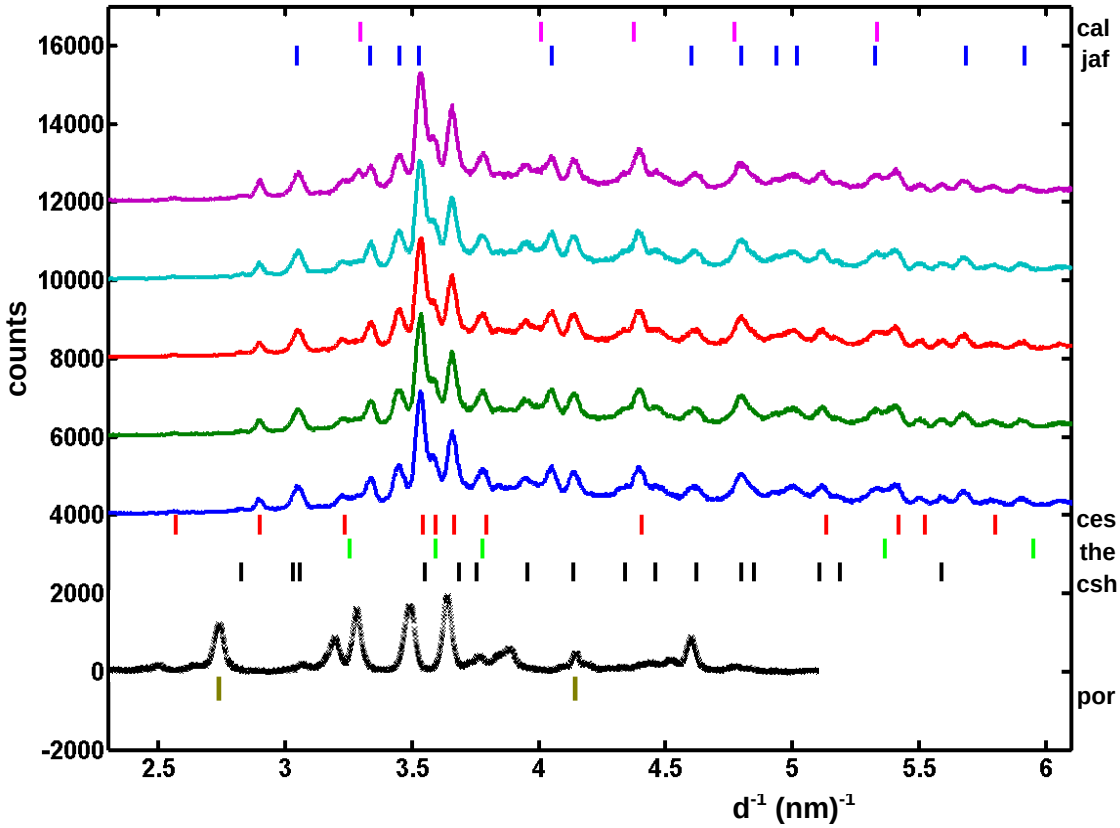

Figure VII-2: Diffraction patterns of sample pre-cured at 200 ℃ for five days, containing cement only, and cured for 30 days at the pre-cured temperature. Each pattern corresponds to a single scan with 1 mm interval across the sample. The bottom pattern (black) corresponds to the pre-cured sample prior to brine attack. The results correspond to the middle detector only. *Cal*, *jaf*, *ces*, *the*, *csh* and *por* corresponds to minerals calcite, jaffeite, cesanite, thenardite, α-dicalcium silicate hydrate and portlandite respectively.

This mineral according to my knowledge is reported here for a first time in cement based materials. In addition the mineral thenardite (Na_2SO_4) is present, the source of which is the brine.

In Figure VII-3 are shown the results from the sample containing 30 wt % of silica flour and cured for 30 days at 200 ℃ in sod ium sulphate. Xonotlite was the mineral formed in this sample before the brine attack (Chapter II). The results show that after the durability test the mineralogy has not altered significantly. Only thenardite (Na_2SO_4) is observed at the edges of the sample (1^{st} and 9^{th} pattern) but it has not penetrated more than 1 mm. The compressive strength of the specific sample is high and the permeability is low resulting in a highly complicated porous structure (Chapter VI). This has a significant impact on the behaviour of this sample in brine as the fluid can not penetrate deeper into the sample, because of this complicated structure, maintaining the mineralogy unchanged.

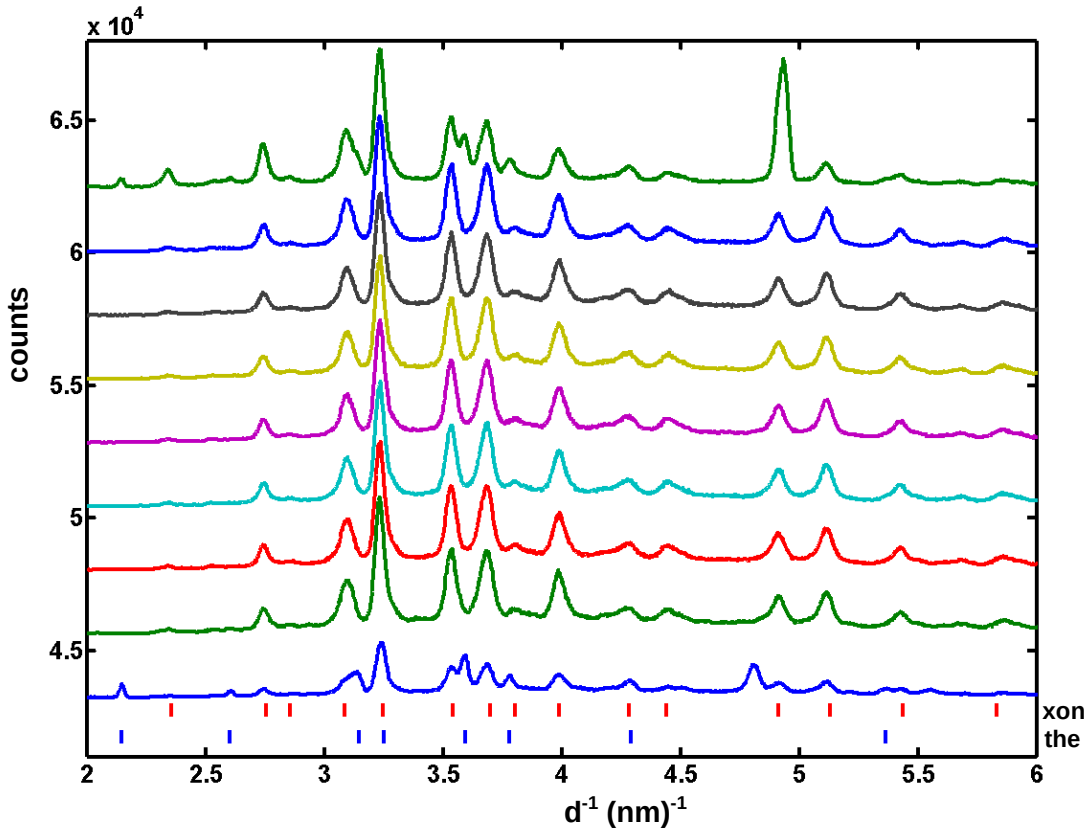

Figure VII-3: Diffraction patterns of sample pre-cured at 200 ℃ for five days, containing 30 wt % of silica flour, and cured for 30 days at the pre-cured temperature. Each pattern corresponds to a single scan with 1 mm interval across the sample. The results correspond to the middle detector only. *Xon* and *the* corresponds to minerals xonotlite and thenardite respectively.

VII- 4. Conclusions

This small chapter describes in detail the experimental procedure carried out regarding the durability studies performed on hydroceramic materials. Tomographic energy-dispersive diffraction imaging (TEDDI) is the technique used to characterize the materials after the durability test and proves to be a powerful tool to map the alterations in mineralogy in cement based materials.

When neat cement only is immersed in sodium sulphate brine, a new mineral forms throughout the sample which is called cesanite instead of portlandite. The formation of the mineral cesanite, in cement based materials, is reported here for a first time. On the other hand sample containing xonotlite proves to be more durable when immersed into the same brine as there is no evidence of alteration in mineralogy. In both cases thenardite is observed. However it is observed only at the edges in sample containing xonotlite.

The durability of the sample containing xonotlite results from the highly complicated microstructure created from the specific mineral, which it does not allow the brine to penetrate into the sample. In contrast the sample containing neat cement only, the minerals formed, create a microstructure with low strength and high permeability allowing the brine to penetrate into the sample and alter the mineralogy.

VII- 5. References

1. N. Meller, "The chemical variation of geothermal fluids with specific relevance to anorthite dissolution." University of Edinburgh, Edinburgh, UK, 2002.

2. V. Barlet-Gouédard, "Ageing durability methodologies with brines." In**.** Shlumberger, France, Paris, 2000.

3. P. Barnes, S. L. Colston, A. C. Jupe, S. D. M. Jacques, M. Attfield, R. Pisula, S. Morgan, C. Hall, P. Livesey, and S. Lunt, "The use of synchrotron sources in the study of cement materials", pp. 477-498 in *Structure and Performance of Cements***.** Edited by J. Bensted and P. Barnes. Spon Press, London & New York, 2002.

4. R. J. Cernik and P. Barnes, "Industrial-aspects of synchrotron X-ray powder diffraction," *Radiation Physics and Chemistry,* **45** [3] 445-457 (1995).

5. R. I. Walton and D. O'Hare, "Watching solids crystallise using in situ powder diffraction," *Physical Chemistry Chemical Physics,* **2** [23] 2283-2291 (2000).

6. C. Hall, P. Barnes, J. K. Cockroft, S. L. Colston, D. Häusermann, S. D. M. Jacques, A. C. Jupe, and M. Kunz, "Synchrotron energy-dispersive X-ray diffraction tomography," *Nuclear Instruments and Methods in Physics Research B,* **140** 253-257 (1998).

7. C. Hall, P. Barnes, J. K. Cockroft, S. D. M. Jacques, A. C. Jupe, X. Turrillas, M. Hanfland, and D. Häusermann, "Rapid whole-rock mineral analysis and composition mapping by synchrotron X-ray diffraction," *Analytical Communications,* **33** 245-248 (1996).

8. C. Hall, S. L. Colston, A. C. Jupe, S. D. M. Jacques, R. Livingston, A. O. A. Ramadan, A. W. Amde, and P. Barnes, "Non-destructive tomographic energy-dispersive diffraction imaging of the interior of bulk concrete," *Cement and Concrete Research,* **30** [3] 491-495 (2000).

9. J. S. O. Evans, R. J. Francis, D. O'Hare, S. J. Price, S. M. Clark, J. Flaherty, J. Gordon, A. Nield, and C. C. Tang, "An apparatus for the study of the kinetics and mechanism of hydrothermal reactions by in-situ energy-dispersive X-ray diffraction," *Review of Scientific Instruments,* **66** [3] 2442-2445 (1995).

10. H. Y. He, P. Barnes, J. Munn, X. Turrillas, and J. Klinowski, "Autoclave synthesis and thermal transformations of the aluminophosphate molecular-sieve Vpi-5 - an insitu X-ray diffraction study," *Chemical Physics Letters,* **196** [3-4] 267-273 (1992).

11. X. Turrillas, P. Barnes, D. Gascoigne, J. Z. Turner, S. L. Jones, C. J. Norman, C. F. Pygall, and A. J. Dent, "Synchrotron-related studies on the dynamic and structural aspects of zirconia synthesis for ceramic and catalytic applications," *Radiation Physics and Chemistry,* **45** [3] 491-508 (1995).

12. P. Barnes, X. Turrillas, A. C. Jupe, S. L. Colston, D. O'Connor, R. J. Cernik, P. Livesey, C. Hall, D. Bates, and R. Dennis, "Applied crystollography solutions to problems in industrial solid-state chemistry: Case examples with ceramics, cements and zeolites," *Journal of the Chemical Society, Faraday Transactions,* **92** [12] 2187-2196 (1996).

13. S. L. Colston, P. Barnes, A. C. Jupe, S. Jacques, C. Hall, P. Livesey, J. Dransfield, and N. Meller, "An in situ synchrotron energy-dispersive diffraction study of the hydration of oilwell cement systems under high temperature/autoclave conditions up to 130 ℃," *Cement and Concrete Research,* **35** [12] 2223-2232 (2005).

14. B. C. Giessen and G. E. Gordon, "X-ray Diffraction - New high speed technique based on X-ray spectrography," *Science,* **159** [3818] 973-& (1968).

15. S. M. Clark, "A new energy-dispersive powder diffraction facility at the SRS," *Nuclear Instruments & Methods in Physics Research Section a-Accelerators Spectrometers Detectors and Associated Equipment,* **381** [1] 161-168 (1996).

16. A. Piotrowski, V. Kahlenberg, R. X. Fischer, Y. Lee, and J. B. Parise, "The crystal structures of cesanite and its synthetic analogue - A comparison," *American Mineralogist,* **87** [5-6] 715-720 (2002).

GENERAL CONCLUSIONS & FUTURE WORK

The aim of this thesis was to develop new cement-based materials for use as sealants in geothermal and deep oil or gas wells. These materials, called hydroceramics, are prepared at temperatures between 200 to 350 ℃ using cement and additives such as silica flour and alumina at different proportions. These hydroceramic formulations have been examined for their mineralogy, engineering properties and durability. The main conclusions are summarized as follows:

A comparison between the pure $CaO\text{-}SiO_2$ system of Taylor with the hydroceramic system showed that many phases appear to be stable at similar temperatures (portlandite, jaffeite, hillebrandite, reinhardbraunsite and xonotlite) however there are numerous differences from the pure system when using real cements.

- The stability of $\alpha\text{-}Ca_2SiO_3(OH)_2$ is extended to < 250 ℃. In addition $Ca_8Si_5O_{18}$ which is not observed by Taylor forms in large proportions when 10 to 20 wt % of silica flour is added.
- The stability of 11Å tobermorite is greatly extended from 170 ℃ to < 300 ℃.
- When alumina is added to the hydroceramics hydrogarnet is the dominant aluminum bearing phase. At temperatures greater that 250 ℃ hydrogarnet is replaced by $Ca_4Al_6O_{13}\bullet 3H_2O$ and when temperature exceeds 300 ℃ it is replaced by both $Ca_4Al_6O_{13}\bullet 3H_2O$ and bicchulite.
- In addition the presence of alumina, particularly fine grained alumina, pushes the stability field of 11 Å tobermorite and gyrolite to higher temperatures.

The chemistry of the major minerals formed in hydroceramics has been studied using electron probe microanalysis (EPMA) and found that:

- The CaO/SiO_2 ratio of belite, alpha dicalcium silicate hydrate, jaffeite, reinhardbraunsite, xonotlite, tobermorite, gyrolite and the $CaO/(CaO+Al_2O_3)$ ratio of hydrogarnet is found to be in good agreement with measurements that have been carried out on either natural minerals or the synthetic equivalent.
- The chemical formulae of all the above minerals show that other elements such as aluminium, iron, magnesium, sulphur and potassium are incorporated in their structures, the source of which is cement.

- The progress of belite hydration has been clearly illustrated in samples containing neat cement only and cured at temperatures between 200 to 250 ℃. The inner part of these grains consisted of belite partially hydrated and the outer part was alpha dicalcium silicate hydrated. The hydration reaction possibly follows the rules encountered in mineral replacement processes.
- Xonotlite is formed topotactically out of tobermorite hence the Ca and Si deficiency.
- The substitution of iron for silicon is lower than aluminum for silicon in tobermorite and the charge imbalance created is neutralized from the univalent cations incorporated in the structure such as sodium and potassium, with the following order $Na^{+}<K^{+}$.
- The anomalous type of 11Å tobermorite is present in the hydroceramics samples.
- The chemistry of the hydrogarnets depends on the amount of silica added to the system and more strongly on the curing temperature. In addition the unit cell size is related to the chemical composition of the hydrogarnets. In the CASH hydroceramic system hydrogarnet composition with *y* values higher than 2.2 has not been observed, thus supporting the view of Jappy and Glasser that there is a miscibility gap in the solid solution series.

The crystal habit of these minerals has been studied using scanning electron microscopy (SEM). The crystals have been simulated using WinXmorph.

- Minerals with CaO/SiO_2 ratio less than 1, such as jaffeite, reinhardbrounsite and xonotlite, occur as needle shape crystals whereas gyrolite and truscottite with CaO/SiO_2 more than 1 occur as hexagonal plate like crystals.
- Anomalous and normal 11Å tobermorite occur as needle and plate like crystal respectively. In the CASH hydroceramic system only the anomalous type is present hence needle shape crystals of tobermorite occur.
- Two different crystal shapes of hydrogarnet have been observed octahedral and icositetrahedral.
- The shape of the simulated crystals of jaffeite, reinhardbraunsite, xonotlite, gyrolite, truscottite and hydrogarnet found to be identical with those shown in the SEM micrographs.

The engineering properties of the hydroceramics such as compressive strength and permeability have been studied using a tensile tester and a permeameter respectively. In addition computed permeabilities have been compared with experimental results.

- By adding more than 20 wt % of silica flour, the engineering properties of the hydroceramics are improved due to the formation of xonotlite, gyrolite or truscottite. The property values of these materials are within the API specifications for very deep oil or geothermal well sealants.
- Adding more than 20 wt % of alumina at 200 ℃ and 250 ℃, results in the formation of hydrogarnets which deteriorate the engineering properties of the hydroceramics as they create highly porous microstructures.
- At 300 ℃ and 350 ℃ when adding alumina, calcium aluminum silicate hydrate and bicchulite grow between the hydrogarnet aggregates, improving permeability, with values lying within the acceptable limits of the API specification. On the other hand, the compressive strength values of these materials are very low and outside of the API specification.
- The simulation values of permeability are in good agreement with the experiments, demonstrating the potential of a computational image-based approach as an alternative to time-consuming experimental measurements of permeability.

Durability studies on some hydroceramic formulations have been carried out in Synchrotron Radiation Source (SRS) at Daresbury laboratories.

- Tomographic energy-dispersive diffraction imaging is a powerful tool to map mineralogical alterations in cement based materials.
- The engineering properties prove to be very important for the behaviour of the hydroceramics under simulated well conditions.
- Sample containing xonotlite (high compressive strength, low permeability) creates complicated microstructures therefore the mineralogy remains unchanged as the brine can not penetrate into the sample.
- Sample containing neat cement only forms minerals which create porous microstructures resulting in altered mineralogy.
- The mineral cesanite which is formed in sample containing neat cement only when immersed into sodium sulphate brine is reported here for a first time.

Further work would include data analysis of the durabilities studies. Different hydroceramic formulations, immersed into different brines, have been examined in Daresbury. The interpretation of these results would be useful as it would reveal important information regarding the behaviour of hydroceramics under different simulated well conditions. In addition work on the engineering properties of the samples tested for durability, especially those with altered mineralogy, would be very important.

Finally all the hydroceramic formulations reported in this thesis have been obtained with silica flour and corundum as additives. Further work would include the use of different additives such as glass powder to replace silica flour or kaolinite.

APPENDICES

APPENDIX – I : Mass of Saturated Vapour

In order to be confident that there was enough water in the Parr cell for the hydration of the hydroceramic samples a calculation of the mass of the saturated vapour has been carried out. The mass of the water vapour is known at all temperatures. Therefore from the ideal gas law ($PV=nRT$) the mass of the saturated vapour in the Parr cell, depending the amount of cups present, has been calculated (Table A-1). In addition in Table A-2 is shown the amount of water required in the Parr cell to maintain the SVP.

Where P is the absolute pressure of the gas, V is the volume of the gas, n is the number of moles in the gas, R is the universal gas constant and T is the absolute temperature.

Table A-1: Mass of saturated vapour pressure in Parr cell. Different mass of SVP is obtained as more cups are in the Parr cell as they reduce the volume of the autoclave.

Mass of Saturated Vapour Pressure in Parr Cell (g)								
No. of cups / T (℃)	**1**	**2**	**3**	**4**	**5**	**6**	**7**	**8**
200	0.8772	0.7747	0.6722	0.5698	0.4673	0.3648	0.2623	0.1599
250	2.2289	1.9685	1.7081	1.4477	1.1874	0.9270	0.6666	0.4062
300	5.1548	4.5526	3.9504	3.3483	2.7461	2.1439	1.5417	0.9395
350	12.6693	11.1893	9.7093	8.2293	6.7492	5.2692	3.7892	2.3092

Table A-2: Mass of water required in the Parr cell depending the amount of cups present in the autoclave.

Mass of water required in Parr Cell (g)								
Cell No. / T (°C)	**1**	**2**	**3**	**4**	**5**	**6**	**7**	**8**
200	-	-	-	-	-	-	-	-
250	2	2	1	-	-	-	-	-
300	5	3	1	1	-	-	-	-
350	12	10	8	6	4	2	-	-

APPENDIX – II : Bogue method

The modified Bogue method is a computational program which calculates the mineral composition of the cement clinker from the elemental (oxide) analysis.[1,2] Only results relevant with this thesis are presented below.

Table B-1: Phase composition of clinker (wt %) as predicted from the modified Bohue method.[2]

Phases	Wt %
Alite	62
Belite	21
Aluminoferrite	13
Gypsum	3

Table B-2: Composition of clinker phase.

	Alite	Belite
Ca	72.264	63.500
Si	25.025	31.500
Al	1.241	1.500
Fe	1.059	1.700
Na	0.099	0.100
Mg	0.260	0.000
P	0.199	0.200
S	0.240	0.240
K	0.089	0.900
Ti	0.000	0.200
Mn	0.000	0.000

[1] H. F. W. Taylor, “Modification of the Bogue calculation,” *Advances in Cement Research*, **2** 73-77 (1989).

[2] C. Hall, “Predicting the phase composition of Portland cements from bulk chemical analysis,” Schlumberger Cambridge Research, Departmental note SRC/SN/1993/014/WPC/C, May 1993.

APPENDIX – III : Calculating Formula from Weight % Oxide

1. Calculate the molar proportion of each oxide by dividing by the molar weight of that oxide, i.e. divide Column 2 by Column 3 in Table C-1. The amount of water is calculated as the difference from 100% of the total.

2. Determine the atomic proportion of oxygen from each molecule by multiplying the molar proportion by the number of oxygens in that oxide, e.g. multiply CaO molar proportion by 1 and SiO_2 molar proportion by 2. At the foot of Column 5 determine the total, T.

3. Re-cast the oxygen atomic proportion by dividing by T and multiplying by the total number of oxygens present in the formula. E.g. for jaffeite $Ca_6(Si_2O_7)(OH)_6$ there are 13 oxygens, 6 from the calcium oxide, 4 from the silicon oxide and 3 for water.

4. To derive the number of cations in the formula multiply re-cast the oxygen atomic proportion by the proportion of cations in the oxide. E.g. for SiO_2 there are half as many silicons as oxygens, therefore multiply by ½. For Al_2O_3 there are 2 aluminiums for every three oxygens therefore multiply by ⅔.

Oxide	*Wt %*	*Mol Wt (g)*	*Mol Prop*	*Oxygen Atomic Proportion*	*Re-cast Oxygen Atomic Proportion*	*Cations*	*No. Cations per oxygen*	*No. Ions in formula based on 10 oxygens*
CaO	65.89	56.08	1.17492	1.17492	6	Ca	1	6
SiO_2	23.53	60.08	0.39164	0.78328	4	Si	½	2
Total	89.42	-	-	-	-	-	-	-
H_2O	10.58	18.01	0.58745	0.58745	3	H	2	3
				T=2.54565	Σ=13			

Table C-1: Calculation of no. ions in formula from Wt % oxide.

APPENDIX – IV : Glossary

Chemical formulae of minerals:

Alpha dicalcium silicate hydrate	$\alpha\text{-}Ca_2SiO_4\bullet(H_2O)$
Bicchulite	$Ca_8(Al_2SiO_6)_4(OH)_8$
Calcium aluminum oxide hydrate	$Ca_4Al_6O_{13}\bullet 3H_2O$
Cesanite	$Na_7Ca_3(SO_4)_6(OH)\bullet 0.8(H_2O)$
Corundum	Al_2O_3
Foshagite	$Ca_4(Si_3O_9)(OH)_2$
Gyrolite	$Ca_{16}Si_{24}O_{60}(OH)_8\bullet(14+n)H_2O \quad (0\leq n\leq 3)$
Hillebrandite	$Ca_2(SiO_3)(OH)_2$
Hydrogarnet	$Ca_3Al_2(SiO_4)_{3-y}(OH)_{4y} \quad (0\leq y\leq 3)$
Jaffeite	$Ca_6(Si_2O_7)(OH)_6$
Kilchoanite	$Ca_6(SiO_4)(Si_3O_{10})$
Portlandite	$Ca(OH)_2$
Quartz	SiO_2
Reinhardbraunsite	$Ca_5(SiO_4)_2(OH)_2$
11Å Tobermorite	$Ca_5Si_6O_{17}\bullet 5(H_2O)$
Truscottite	$Ca_{14}Si_{24}O_{62}\bullet(4+z)H_2O \quad (0<z<6)$
Xonotlite	$Ca_6Si_6O_{17}(OH)_2$

Abbreviations:

XRD	X-ray powder Diffraction
SEM	Scanning Electron Microscope
EPMA	Electron Probe Microanalysis
TEDDI	Tomographic Energy-Dispersive Diffraction Imaging

APPENDIX – V : Publications

Refereed papers

N. Meller, C. Hall, K. Kyritsis and G. Giriat, "Synthesis of cement based CaO-Al_2O_3-SiO_2-H_2O (CASH) hydroceramics at 200 and 250 ℃: Ex-situ and in-situ diffraction" *Cement and Concrete Research*, **37** [6] 823-833 (2007).

K. Kyritsis, N. Meller and C. Hall, "The relationship between the microstructure and the engineering properties of hydroceramic sealants for geothermal wells", *Proceedings of the 12th International Congress on the Chemistry of Cement (ICCC)*. Montreal Canada, 2007.

N. Meller, C. Hall, K. Kyritsis, G. Giriat, H. J. Jakobsen and J. Skibsted, "Incorporation of aluminium guest ions in nominally alumina-free calcium silicate hydrates: effects on crystal structure and thermal stability", *Proceedings of the 12th International Congress on the Chemistry of Cement (ICCC)*. Montreal Canada, 2007.

N. Meller, K. Kyritsis and C. Hall, "The mineralogy of the CaO-Al_2O_3-SiO_2-H_2O (CASH) hydroceramic system from 200 to 350 ℃" *Cement and Concrete Research*, (accepted).

K. Kyritsis, N. Meller and C. Hall, "Chemistry and morphology of hydrogarnets formed in cement-based CASH hydroceramics cured at 200 ℃ to 350 ℃" *Journal of the American Ceramic Society*, (accepted).

K. Kyritsis, C. Hall, D. P. Bentz, N. Meller and M. A. Wilson, "Relationship between the engineering properties, mineralogy and microstructure in cement based hydroceramic materials cured at 200 ℃ to 350 ℃" *Journal of the American Ceramic Society*, (accepted).

N. Meller, K. Kyritsis and C. Hall, “The hydrothermal decomposition of calcium monosulfate-14 to katoite hydrogarnet and α-anhydrite: an in-situ synchrotron X-ray diffraction study” *Cement and Concrete Research*, (submitted).

D. P. Bentz, E. J. Garboczi, N. S. Martys, K. A. Snyder, W. S. Guthrie, K. Kyritsis and N. Neithalath, “Virtual testing of concrete transport properties” *American Concrete Institute (ACI) Fall 2009 Convention on Material Science Modelling*. New Orleans USA, (submitted).

N. Meller, J. Skibsted, C. Hall, K. Kyritsis and H. J. Jakobsen, “The effect of aluminium guest-ions in xonotlite, 11Å tobermorite and gyrolite: Crystal structure and thermal stability” (in prep.)